IMAGE PROCESSING APPROACHES FOR NOISE REDUCTION IN EDDY CURRENT IMAGES

By

B. SASI
(Enrollment No: ENGG02200804020)

Indira Gandhi Centre for Atomic Research, Kalpakkam

A thesis submitted to the
Board of Studies in Engineering Sciences

In partial fulfillment of requirements
for the Degree of

DOCTOR OF PHILOSOPHY
of

HOMI BHABHA NATIONAL INSTITUTE

AUGUST, 2015

Homi Bhabha National Institute

Recommendations of the Viva Voce Board

As members of the Viva Voce Board, we certify that we have read the dissertation prepared by **B. Sasi** entitled "**Image processing approaches for noise reduction in eddy current images**" and recommend that it may be accepted as fulfilling the dissertation requirement for the Degree of Doctor of Philosophy.

U. Kamachi Mudali — 02/9/16

Chairman-**Dr. U. Kamachi Mudali** Date:

2/9/2016

Guide / Convener-**Dr. B. Purna Chandra Rao** Date:

AK Bhaduri — 02/9/2016

Member 1- **Dr. A.K. Bhaduri** Date:

2/9/16

Member 2- **Dr. B.K. Panigrahi** Date:

02/09/2016

External Examiner - **Dr. C. V. Krishnamurthy** Date:

Final approval and acceptance of this dissertation is contingent upon the candidate's submission of the final copies of the dissertation to HBNI.

I hereby certify that I have read this dissertation prepared under my guidance and recommend that it may be accepted as fulfilling the dissertation requirement.

Date: 2/9/2016

Place: Kalpakkam

Dr. B. Purna Chandra Rao

Guide

STATEMENT BY AUTHOR

This dissertation has been submitted in partial fulfillment of requirements for an advanced degree at Homi Bhabha National Institute (HBNI) and is deposited in the library to be made available to borrowers under rules of the HBNI.

Brief quotations from this dissertation are allowable without special permission, provided that accurate acknowledgement of source is made. Requests for permission for extended quotation from or reproduction of this manuscript in whole or in part may be granted by the Competent Authority of HBNI when in his or her judgment the proposed use of the material is in the interests of scholarship. In all other instances, however, permission must be obtained from the author.

B. Sasi

(B. Sasi)

Date : 2/9/16

Place : Kalpakkam

DECLARATION

I, hereby declare that the investigation presented in the thesis entitled **"Image processing approaches for noise reduction in eddy current images"** submitted to Homi Bhabha National Institute (HBNI), Mumbai, India, for the award of Doctor of Philosophy in Engineering Sciences, is the record of work carried out by me under the guidance of Prof. B. Purnachandra Rao, Head, Nondestructive Evaluation Division, Metallurgy and Materials Group, Indira Gandhi Centre for Atomic Research, Kalpakkam. The work is original and has not been submitted earlier as a whole or in part for a degree/diploma at this or any other Institution/University.

(B. Sasi)

Date : 2/9/16

Place : Kalpakkam

LIST OF PUBLICATIONS ARISING FROM THE THESIS

JOURNALS

1. **B. Sasi**, M.S. Ahamed Ali, C. Babu Rao and T. Jayakumar, "Effective de-noising and characterization of flaws in eddy current-NDE images, Int. Journal of Signal and Imaging System Engineering, Vol.7, No.3, pp. 236-251, 2014.

2. **B. Sasi**, Matteo Cacciola, C. Babu Rao, T. Jayakumar and Baldev Raj, "Hybrid signal processing approach for enhanced detection of flaws in eddy current NDE", Research in NDE, Vol.24, No.1, pp. 51-61, 2013.

3. **B. Sasi**, Matteo Cacciola, Lalita Udpa, B.P.C. Rao, T. Jayakumar and Baldev Raj, "Development of image fusion methodology for EC images using discrete wavelet transform", NDT & E International, Vol.51, pp. 51-57, 2012.

4. **B. Sasi**, B.P.C. Rao, T. Jayakumar and Baldev Raj, "Wavelet transform based de-noising method for processing eddy current signals", Research in NDE, Vol.21, No.3, pp.157-170, 2010.

B. Sasi
2/9/16
(B. Sasi)

Solely dedicated to

my Parents

ACKNOWLEDGEMENTS

My deepest gratitude goes first and foremost to my research supervisor Prof. B. Purna Chandra Rao, Head, Nondestructive Evaluation Division (NDED), Indira Gandhi Centre for Atomic Research (IGCAR) for his consistent guidance, instructive suggestions and valuable comments. I am deeply obliged to his meticulous planning, effective approach and perfections in all the research works. I express my heartfelt gratitude to Dr. T. Jayakumar, former Director, Metallurgy and Materials Group (MMG), IGCAR for his constant inspiration, encouragement and all round support that led to the successful completion of this work. I am indebted to Dr. C. Babu Rao, Raman Research Fellow, IGCAR whose passionate academic advice and support during this work have been invaluable to me.

My sincere thanks to eminent members of the doctoral committee Dr. U. Kamachi Mudali, Dr. A. K. Badhuri and Dr. B. K. Panigrahi, for their regular evaluation of the research work and suggestions to improve the quality of this work. I would like to extend my heartfelt thanks to the former directors of IGCAR, Dr. Baldev Raj, Shri S. C. Chetal and Dr. P. R. Vasudeva Rao, for permitting me to pursue research in IGCAR.

I take this opportunity to thank Dr. C. K. Mukhopadhyay, Head, EMSI section, NDED, IGCAR for providing me the freedom to pursue this research work. My sincere thanks are due to Dr. S. Thriunavukkarasu, Shri S. Mahadevan and Dr. K. V. Rajkumar for providing their valuable advice, time and careful reading of all my works and extending their help in the preparation of the thesis in an effective manner.

My thanks are also due to my fellow colleagues, Dr. W. Sharatchandra Singh and Shri S. Ponseenivasan, for providing me technical support in various occasions of the thesis work. I wish to acknowledge Shri P. Krishnaiah (Retired), Shri V. Arjun, Shri K. Sambasiva Rao, SRF, HBNI and Shri Anil Kumar Soni, SRF, HBNI, for their help. I also thank the staff members of the NDED for their helpful assistance.

The informal encouragement and help of many friends has been indispensable and I acknowledge the contribution of my husband Shri B. Madhu who has been always my sensible counsellor and great supporter. Special thanks should go to my mother-in-law Smt P. B. Leelakumari for her spiritual and parental support. I am due gratitude to my daughter Ms. M. Gopika who is the joy and everything of my life for her understanding, support and patience during my research work. Special thanks to my father Late Shri K. Balakrishnan and mother Smt M. T. Devayani for their moral support and their endless love I felt through the distance.

B. Sasi

(B. Sasi)

Date: 2/9/16

Place: Kalpakkam

TABLE OF CONTENTS

ABSTRACT

Nondestructive evaluation (NDE) plays an important role in ensuring structural integrity of engineering components through detection and sizing of flaws. It is very important to detect flaws in components at the early stages to prevent catastrophic failures. Eddy current (EC) NDE technique is simultaneously influenced by several variables such as surface roughness, variations in probe lift-off, variations in electrical conductivity and magnetic permeability and variations in geometry, apart from flaws. These variations produce large amplitude noise and thus, often mask information from shallow surface flaws as well as deep seated flaws. Although EC imaging is helpful, detection of shallow surface flaws in the presence of such composite noise is challenging.

Removal of noise in EC images is time consuming, as it involves the use of several methods of processing depending on the sources of noise. The reported literature on processing of EC images, influenced by noise, is limited to handling one disturbing variable at a time. Information related to processing of composite noise in EC images is scarce in open literature. This demands development of image processing approaches for automated removal of noise in EC images while retaining maximum possible information related to flaws.

This thesis presents the development of image processing approaches for noise reduction in EC images of surface flaws in AISI type 316 Stainless steels. It incorporates spatially adaptive noise filtering using multiresolution analysis by Discrete Wavelet Transform (DWT). It explores Independent Component Analysis (ICA) technique that involves separation of sources of noise based on their statistical independence.

Extensive studies have been carried out on the EC images acquired from plates, weld plates and thin walled tubes made of AISI type 316 stainless steels to develop the DWT

and ICA based approaches. Performances of these approaches have been evaluated using Noise Reduction Percentage (NRP) and Signal to Noise Ratio (SNR).

This thesis proposes a hybrid image processing approach by combining the advantage of the noise reduction ability of DWT based approach and the flaw retention ability of ICA based approach. A significant enhancement in flaw amplitude has been achieved by the proposed hybrid approach as compared to the individual processing approaches. The hybrid approach is found to be noise tolerant to variations in lift-off up to ≤1.5 mm.

The efficacy of the proposed hybrid approach has been successfully demonstrated on EC images acquired at various frequencies (20 kHz, 75 kHz and 150 kHz) using probes of 3.0 mm, 5.0 mm and 20.0 mm diameter. The denoising capability of the proposed hybrid approach has been successfully validated on the influence of composite noise from variation in lift-off and wall thickness (geometrical variations) in thin wall SS tubes. The applicability of the proposed hybrid approach has been evaluated for enhancement of sub-surface flaws and natural crack.

The hybrid approach proposed in this thesis has significantly enhanced the flaw detection sensitivity. It has also provided better insight into the existence of statistical dependency and utilization of dependency for enhanced effective separation of flaw information. The approach proposed in this thesis can be applied to EC images of flaws of varying orientation, width and depth and can be extended to other NDE images.

LIST OF FIGURES

LIST OF TABLES

NOMENCLATURE

LIST OF SYMBOLS

dB	decibel
kHz	kilo Hertz
m/s	meter per second
mm	millimeter
V	Volts
δ	Standard depth of penetration
μ	Magnetic permeability
μ_r	Relative magnetic permeability
σ	Electrical conductivity
ϕ	Phase angle
λ	Eigen value
ν	Eigen vector
Ψ	Wavelet filter
J_z	Current density along the depth
J_0	Current density at the surface
B	Magnetic field density
E	Electric field
R	Resistance
X_L	Reactance
Z	Impedance
f	Excitation frequency
g	Wavelet function
h	Scaling function
P_i	Probability distribution
$\mathbf{W}$	(Bold capital letters) Matrices
$\mathbf{x}$	(Bold small letters) Vectors
y	(Italic small letters) Scalars
D	Decision operator
$f(\cdot)$	Function representation

LIST OF ABBREVIATIONS

ADC	Analog-to Digital Converter
AET	Acoustic Emission Testing
AISI	American Iron and Steel Institute
AWGN	Additive White Gaussian Noise
Bior	Biorthogonal
BSS	Blind Source Separation
Coif	Coiflet
CWT	Continuous Wavelet Transform
DAQ	Data Acquisition
Db5	Daubechies
DWT	Discrete Wavelet Transform
EC	Eddy Current
ECT	Eddy Current Testing
EDM	Electric Discharge Machining
FBTR	Fast Breeder Test Reactor
FRP	Flaw Reduction Percentage
GCD	Generalised Gaussian Distribution
HAZ	Heat affected Zone
ICA	Independent Component Analysis
IRT	Infrared Thermography Testing
KL	Karhunen Loeve
LPT	Liquid Penetrant Testing
MPT	Magnetic Particle Testing
MSE	Mean Square Error
NDE	Nondestructive Evaluation
NDT	Nondestructive Testing
NRP	Noise Reduction Percentage
PCA	Principle Component Analysis
pdf	Probability Density Function
PSF	Point Spread Function
ROI	Region of Interest
RT	Radiography Testing
SNR	Signal-to-Noise Ratio
SS	Stainless Steel

SURE	Stein’s Unbiased Risk Estimator
Sym	Symlet
UT	Ultrasonic Testing
VT	Visual Testing
WT	Wavelet Transform

Chapter 1 : Introduction

Preamble

This chapter provides a brief introduction to non-destructive evaluation (NDE) and eddy current NDE technique. It describes the basics of eddy current imaging and enlists the sources of noise in eddy current NDE and their influence on flaw detection. It covers the basics of image processing approaches employed for noise removal.

1.1 Nondestructive evaluation

Nondestructive Evaluation (NDE) is a branch of science that deals with the assessment of structural integrity of engineering components through detection and quantification of flaws, microstructural variations and residual stresses without causing any damage to the components [1]. NDE is an integral part of nuclear, aerospace, petrochemical and other industries to ensure safety and reliability of the plant components. The critical components such as heat exchangers of boilers, steam generators and condensers, aircraft engines, wire ropes, gas pipelines etc. are subjected to NDE, essentially because their failures will affect the plant availability, productivity and profitability. Flaws can form in a component during manufacturing process e.g. casting, welding, rolling, forging and machining and can also form during the service life of a component due to initiation and growth of creep cavities, fatigue cracks and stress corrosion cracks [2]. A flaw in a component creates a substantial chance of failure over long years of service. To ensure safety and reliability of components, early detection and sizing of flaws is essential.

A variety of NDE techniques such as visual testing (VT), liquid penetrant testing (LPT), ultrasonic testing (UT), radiography testing (RT), infrared thermography testing (IRT), acoustic emission testing (AET), eddy current testing (ECT), magnetic particle testing (MPT) are popular for detection of flaws. Among these, VT technique is generally used for quick assessment of quality of welds while RT and UT techniques are employed for volumetric examination. Eddy current (EC) and magnetic (MPT and magnetic flux leakage) techniques are preferred for the detection of surface and sub-surface flaws in non-ferromagnetic and ferromagnetic components respectively [3, 4].

In general, a NDE system consists of three units, i.e. excitation, reception and processing units. In excitation unit, a particular form of energy, e.g. electromagnetic energy in ECT, is used as input to an exciter to send energy into an object under test. The energy is transformed depending on the material properties and flaws in the object. The transformed energy is picked up by a receiver or sensor in the reception unit. In the processing unit, the receiver response is processed and displayed in the form of a signal or an image to extract information about the flaw present in the test [5].

NDE techniques are based on various physical principles. They use different forms of energy as the basis for measurements. Every technique is influenced by a physical property and this aspect is used for detection of flaws as shown in Table 1.1. The choice of NDE techniques for a particular application is dictated by the material, component geometry, characteristics of the expected flaws, accessibility and cost effectiveness.

Among the host of NDE techniques, EC technique is widely used for testing thin (thickness $\leq$ 5.0 mm) electrically conducting materials, such as stainless steel, titanium, brass, aluminium and inconel etc. EC technique is extensively used in aerospace, nuclear, petrochemical and automobile industries [6, 7]. This technique can detect wall thinning, cracks, pitting, stress corrosion cracking, hydrogen embrittlement, denting and deposits. The most popular applications of this technique include detection of flaws in plates, tubes, rods, bars, multi-layer structures, discs, welds, blades, and other regular as well as irregular geometries; material sorting, proximity sensing, coating thickness measurements, heat treatment adequacy assessment and liquid sodium level monitoring [8, 9]. The widespread use of this technique is due to its ease of operation, versatility, excellent sensitivity to surface as well as subsurface flaws in metallic materials and repeatability.

Table 1.1 List of various NDE techniques.

Technique	Energy	Influence by physical property	Materials applicable	Detection of flaws
ECT	5-5000 kHz	Electrical conductivity Magnetic permeability	Conducting	Surface and subsurface
IRT	300GHz-400THz	Thermal conductivity	Thermally Conducting	Surface and subsurface
MFL	Steady state 10-100 Hz	Magnetic permeability	Magnetic	Surface and subsurface
MPT	Steady state magnetic field	Magnetic permeability	Magnetic	Surface
RT	X-ray	Density	Conducting, Non-conducting	Surface and subsurface
UT	Sound (0.5-25 MHz)	Acoustic impedance	Conducting, Non-conducting	Surface and subsurface
VT	Light, UV light	Contrast between flaw and background	Conducting, Non-conducting	Surface

EC testing is carried out on stainless steels (SS), which are major structural materials in nuclear and chemical industries in view of their good corrosion resistance and better mechanical properties (yield, ductility, and toughness). In these steels, early detection of flaws is important, since, flaws occur in a component and may grow due to exposure to elevated temperatures, hostile media or stresses [10].

Large SS components are made by joining of plates by a welding process. A welded component may fail at the weld or heat affected zone (HAZ) regions, because of improper design of weld joints, incorrect selection of filler material, inappropriate welding process, undesired microstructure, residual stresses and corrosion, etc. Further, a flaw may grow during the service life of a welded component. Most commonly found weld flaws include lack of fusion, lack of penetration, cracks, cavities, porosities, slag inclusions and an excessive penetration. Among these, cracks are more harmful. They classified into longitudinal and transverse, depending on their direction with respect to the weld direction i.e. along or perpendicular [10].

Another major component is a tubular product mainly used as heat exchangers and steam generators in power and petrochemical industries. EC technique is the most preferred technique for testing nonmagnetic (μ_r=1.0) heat exchanger tubes.

The measurements made in EC technique, for that matter in all NDE techniques, are relative and not absolute. As a result, calibration or reference standards consisting of artificial flaws are used for comparison and interpretation of the measured data [8]. Calibration standards are made from specimens having identical dimensions, material properties and ageing conditions as that of the component being tested. Through holes, flat bottom holes and notch type of artificial flaws of different dimensions are often used to represent the expected flaws in components, for instrument calibration and for flaw sizing purpose. Electric discharge machining (EDM) is used for fabrication of these artificial flaws.

1.2 Principle of eddy current technique

EC technique works on the principle of electromagnetic induction [6]. Figure 1.1 shows the schematic of basic principles of the EC technique. In this technique, change in coil impedance of a coil (also called probe or sensor) excited with sinusoidal current is measured when it is placed over an electrically conducting material surface. The primary magnetic field set up by the coil induces eddy currents (according to the Faraday's law) in the material, which in turn, sets up secondary magnetic fields.

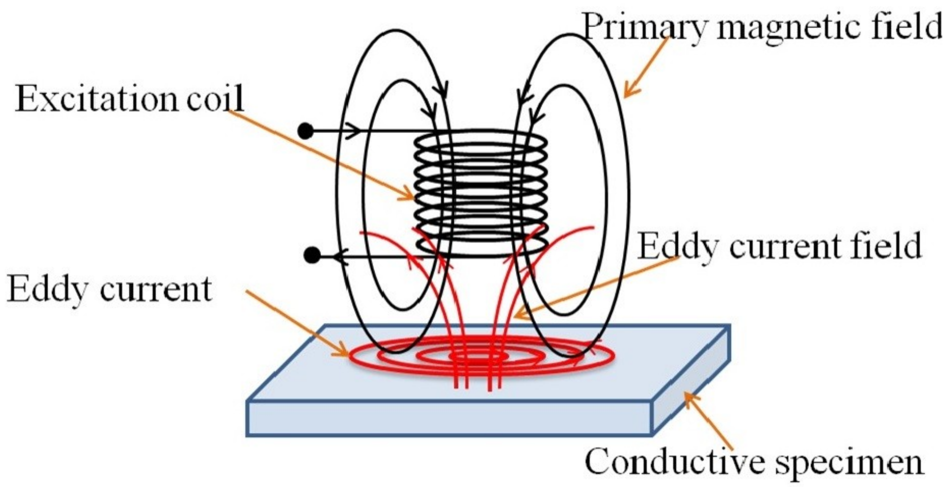

Figure 1.1 Principle of eddy current testing technique.

According to the Lenz's law, the secondary magnetic fields oppose the primary magnetic fields of the coil [3]. This results in a reduction of flux linkage to the coil which manifests as a change in coil impedance ($\boldsymbol{Z}$). The impedance is a complex quantity with resistance component, $\boldsymbol{R}$ (real) and inductive reactance component $\boldsymbol{X_L}$ (imaginary) as

$$\boldsymbol{Z} = \boldsymbol{R} + j\boldsymbol{X_L} \tag{1.1}$$

where magnitude and phase angle of the coil impedance in expressed as

$$\boldsymbol{Z} = \sqrt{\boldsymbol{R}^2 + \boldsymbol{X}_L^2} \qquad 1.2$$

$$\theta = tan^{-1}\frac{\boldsymbol{X_L}}{\boldsymbol{R}} \qquad 1.3$$

The presence of flaws such as cracks, voids, inclusions, corrosion, wall loss, etc. alters the distribution of eddy currents and hence changes the coil impedance [8]. The impedance changes for flaw-free and flaw regions are different and this enables successful detection of a flaw.

The amplitude and phase characteristics of eddy current sinusoids in an electrically conducting test material can be obtained by solving the governing differential equation. The governing differential equation for a coil excited with an alternating current and producing eddy currents $\boldsymbol{J}$ in a homogeneous isotropic electrically conducting material is derived from the Maxwell's curl equations [3]

$$\boldsymbol{\nabla} \times \boldsymbol{E} = -\frac{d\boldsymbol{B}}{dt} \qquad 1.4$$

$$\boldsymbol{\nabla} \times \boldsymbol{B} = \mu \boldsymbol{J} \qquad 1.5$$

where $\boldsymbol{E}$ is the electric field, $\boldsymbol{B}$ is the magnetic field density, **J** is the current density and μ is the magnetic permeability of the material. Upon simplifying, the partial differential equation describing the ECT is given as

$$\nabla^2 \boldsymbol{J} = j\omega\mu\sigma J \qquad 1.6$$

Solving equation (1.6) provides the distribution of **J** in the thickness direction [3]:

$$\boldsymbol{J_z} = \boldsymbol{J_0} e^{\{-\beta\}} sin\,(\omega t - \beta) \qquad 1.7$$

where $\mathbf{J_z}$ is the induced current density along the thickness of the material (z-axis) and $\mathbf{J_0}$ is the current density at the surface of the material. The induced current density (equation 1.7) contains amplitude and phase lag information which represents the flow of eddy currents in the material. β is the phase lag at depth, z and is defined as

$$\beta = z\sqrt{\pi f \mu \sigma} \qquad 1.8$$

The flow of eddy currents is not uniform in the thickness direction. The induced eddy current density in equation (1.7), decays exponentially and the phase lag β varies linearly with depth in thickness direction (equation 1.8). The eddy currents are maximum at the surface of the material and they decrease with depth, following the *skin effect* phenomenon. For a coil excited by an alternating current at a frequency f, the depth at which the current density decreases by the factor *1/e* (37%) surface current density, is called standard depth of penetration (δ) and is defined as

$$\delta = \frac{1}{\sqrt{\pi f \mu \sigma}} \qquad 1.9$$

where f is the excitation frequency, μ is the magnetic permeability and σ is the electrical conductivity. As can be seen from the equation (1.9), δ depends on f, σ and μ. Any increase in the value of these parameters decreases δ.

1.2.1 Eddy current probe

Eddy current probe has two main functions. First, the EC probe establishes varying electromagnetic fields that induce eddy currents in the object under test. Second, the EC probe senses the change in impedance due to the presence of a flaw in the test object. The configuration of an EC probe depends on the geometry of the test object. Different types of probe configurations are used for different applications include the following [8]:

- Surface or pancake probes used for testing plates and bolt-holes.

- Encircling probes used for inspection of tubes, bars with outside access.
- Bobbin probes used for inspection of tubes with inside access.

EC probes operate in i) absolute mode (single coil), ii) differential mode (two coils wound in opposite directions) and iii) send-receive mode (separate excitation coil and separate receiver coil or solid state sensor e.g. Hall, GMR). Absolute probes are employed for testing plate geometries and they are good for detection of flaws as well as gradual variations e.g. wall thickness. However, absolute probes are sensitive to lift-off variation (distance between probe and component surface), probe tilt and temperature changes. Differential probes are employed for testing of cylindrical objects and they are good for detection of small flaws. These probes are immune to changes in temperature as well as operator induced probe wobble. Send-receive probes are employed for testing of thick objects and they are good for detection of sub-surface flaws.

1.2.2 Eddy current instrument

The typical EC instrument consists of a sinusoidal drive unit for producing excitation frequencies in the range of 50.0 Hz-5.0 MHz to excite the EC probe. A high precision Wheatstone bridge circuit is used for measuring the changes in coil impedance as voltage drop. Amplifiers, filters, oscilloscope (to display the impedance changes in a 2-D graph or as a vector) and data acquisition card are used for signal handling and display. Signal analysis techniques are applied to interpret the received signal. The final result is displayed in impedance plane or time-domain.

1.2.3 Eddy current signal

The locus of changes in impedance of an EC probe, during the movement of the probe over a over test object is called an EC signal. The EC signal consists of two components viz. resistance and inductive reactance as shown in Figure 1.2 (a). The EC signal is also visualized as a Lissajous figure on complex (impedance) plane as shown in Figure 1.2 (b) with resistance as abscissa and inductive reactance as ordinate for two surface flaws (D1 and D2) of length 6.0 mm, width 2.0 mm and depths 0.2 mm and 0.5 mm in a 5.0 mm thick stainless steel plate.

From Figure 1.2 (a) the amplitude of EC signal provides information about the severity of the flaw. On the other hand, in the impedance plane (Figure 1.2 b) the signal phase angle provides information about the depth of the flaw. The signal extent or flaw length cannot be visualized by merely scanning the probe over a flaw. A clear benefit exists if a series of parallel line scans (raster scan) are made.

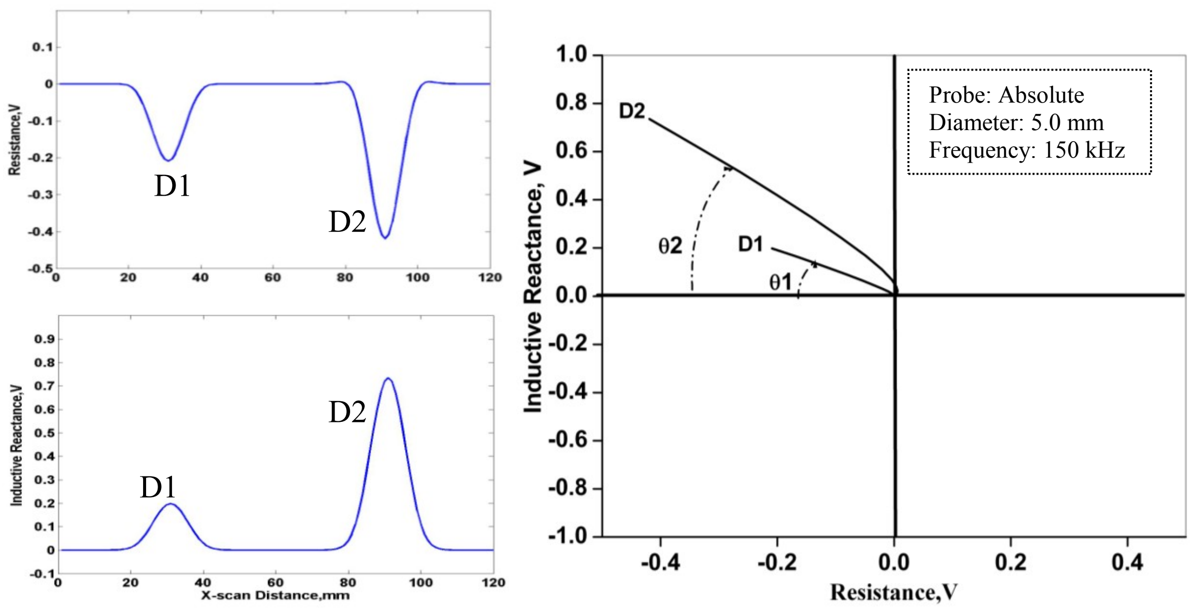

(a) Time-domain signals (b) Impedance plane signal

Figure 1.2 Typical EC signals of two surface flaws, D1, D2 (depth 0.1 mm, 0.5 mm) in (a) time domain and (b) impedance plane.

1.2.4 Eddy current imaging

Unlike other NDE imaging modalities (radiography, thermography), EC imaging is usually performed by raster scanning of a probe over the test object as illustrated in Figure 1.3. The impedance values obtained at discrete positions are collated to form a pseudo colour or a grey level image. This is mathematically represented by convolution operation.

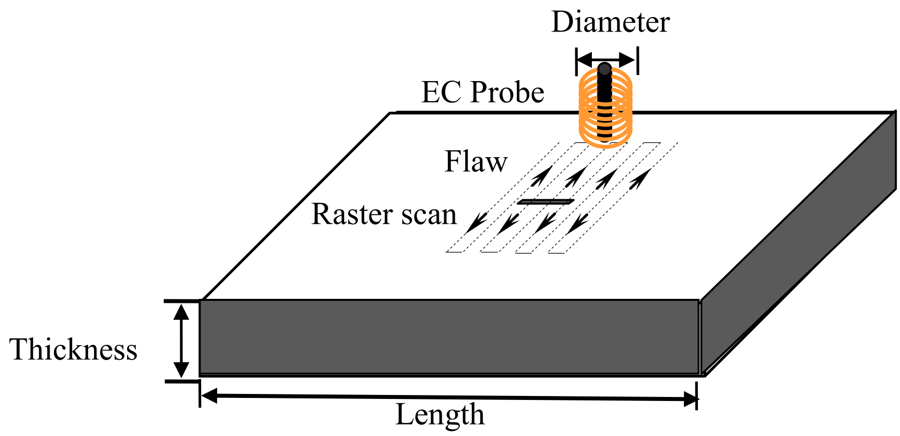

Figure 1.3 Schematic representation of raster scan of a plate using a single absolute EC probe.

In other words, convolution of point spread function (*psf*) of the probe with mapping of electrical conductivity and magnetic permeability of the test object results in an EC image [11]. EC imaging system can be modelled as a two dimensional linear system where output y(m,n) can be obtained by convolution of impulse response $\mathcal{H}[.]$ with the input flaw image x(m,n).

$$y(m,n) = \mathcal{H}[.] * x(m,n) \qquad 1.10$$

EC imaging can be done in three ways. They are by i) raster scan using a single absolute probe, ii) linear scan using single array probe and iii) matrix array probe either stationary or moving [12]. Although array probes are advantageous for faster detection of flaws, certain drawbacks limit their wide spread use. These include the difficulty in manufacturing identical array probe coils, large number of probes required for covering the scan area and lower sampling rate due to multiplexing. Hence, EC imaging by raster scanning using a single probe is still preferred for reliable detection and accurate sizing of flaws [13].

Typical resistance, inductive reactance, magnitude and phase images of a surface breaking flaw (length 6.0 mm, width 0.5 mm and depth 0.5 mm) in 5.0 mm thick SS plate at 5 kHz using a single probe are shown in Figure 1.4. EC images are more convenient to interpret and are useful to obtain the length and width of the flaw.

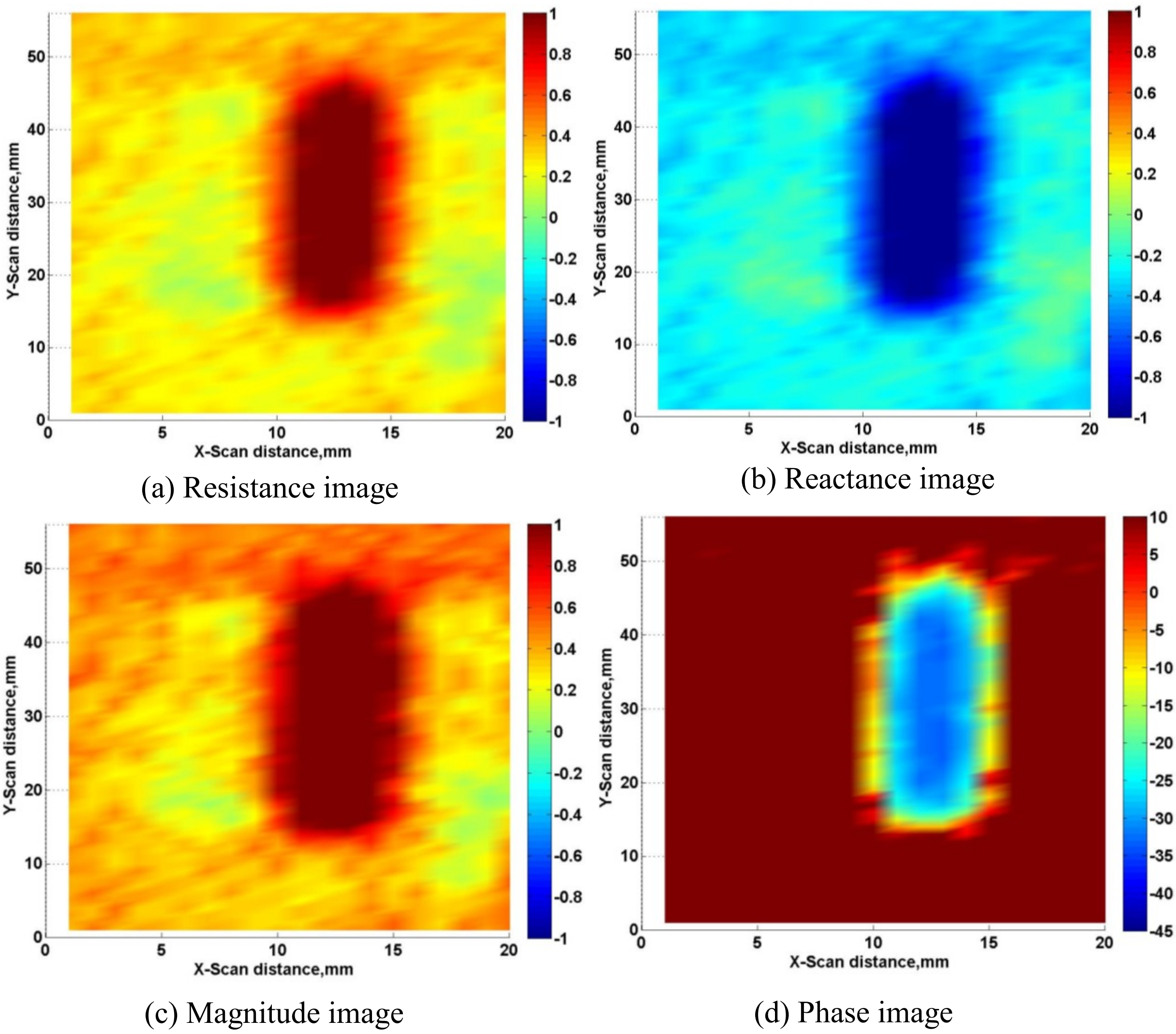

(a) Resistance image

(b) Reactance image

(c) Magnitude image

(d) Phase image

Figure 1.4 Different EC images obtained for a surface flaw.

However, EC images have the influence of disturbing variables, apart from blurring due to convolution of *psf* of a probe with flaws. The variables are the following:

a) change in electromagnetic coupling due to surface roughness, variations in probe lift-off and wobble
b) change in material properties due to alloy non-uniformity either in composition or due to heat treatment condition and inhomogeneous microstructure with a distribution of magnetic delta ferrite (material properties) in weld region.
c) change in geometry of the component (wall thickness variations in thin tubular component due to die chattering and pilgering effect).

These variables produce impedance changes. These signals often mask small amplitude signals from flaws and influence the detection sensitivity. These are unwanted information and are termed as noise.

The simultaneous occurrence of more than one noise (e.g. variations in material properties and variations in lift-off) is phrased as 'composite noise' in the thesis. The random occurrence of one or more variables generates variations in spatial distribution of noise. The removal of this composite noise in EC images is challenging and is investigated in this thesis.

The disturbing noise due to variations in lift-off and material properties is a great concern in EC testing of SS plates and welds. The influence of noise from single source and composite noise on flaw detection is discussed in the next section.

1.3 Influence of noise in EC imaging

1.3.1 Single source of noise: Variations in lift-off

Electromagnetic coupling between EC probe and test object under test is very important during EC inspections. The distance between the probe and object under test is called lift-off for pancake probe and is called fill-factor for bobbin as well as encircling probes. The variation in coupling due to change in lift-off produces large amplitude signals termed as noise and this disturbs the EC testing. During ECT, uniform lift-off is preferred. Usually lift-off signal is made parallel to X-axis on the impedance plane display for discriminatory purposes.

A varying lift-off can be caused by an irregular surface of the material or by non uniform probe movement. Typical EC image with variations in lift-off (0.0 mm to 1.0 mm) from single source is shown in Figure 1.5.

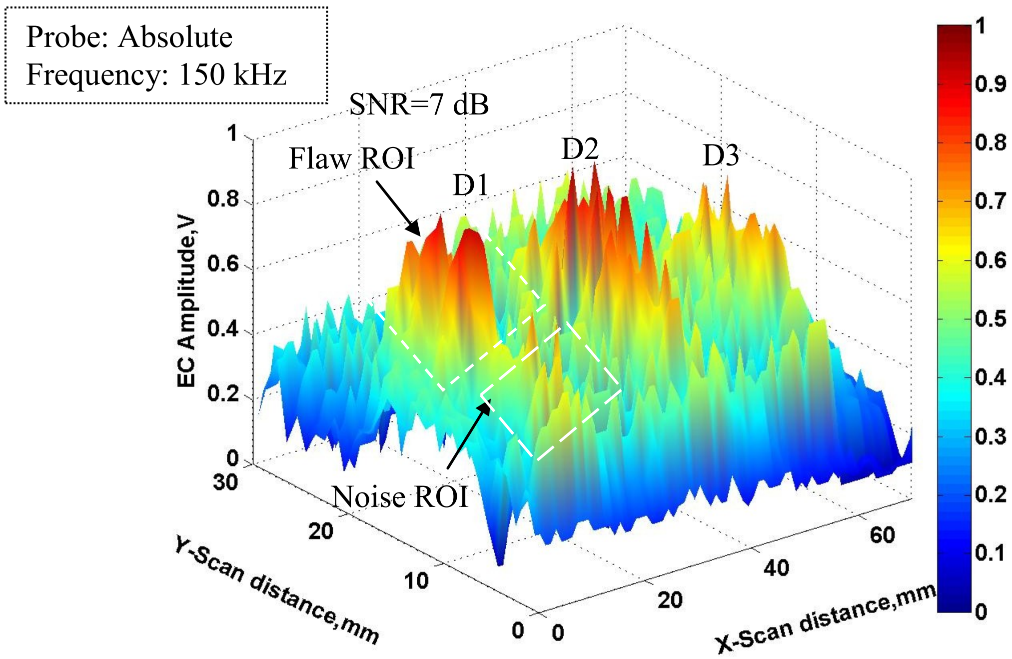

Figure 1.5 EC image of flaws (D1, D2, D3) of depths 0.5 mm, 0.8 mm and 1.0 mm in a SS plate with variations in lift-off (0.0 mm to 1.0mm).

This is an EC image obtained for a 5.0 mm thick SS plate having three flaws (D1, D2 and D3) of length 8.0 mm and width 0.6 mm. Clearly seen, the lift-off variations degrade the flaw information present in the image and unambiguous detection of flaw is difficult. Figure 1.6 compares the EC signals for two flaws (D1 and D2 shown in Figure 1.2) acquired at constant lift-off of 0.3 mm and with variations in lift-off (0.0 mm to 1.0 mm).

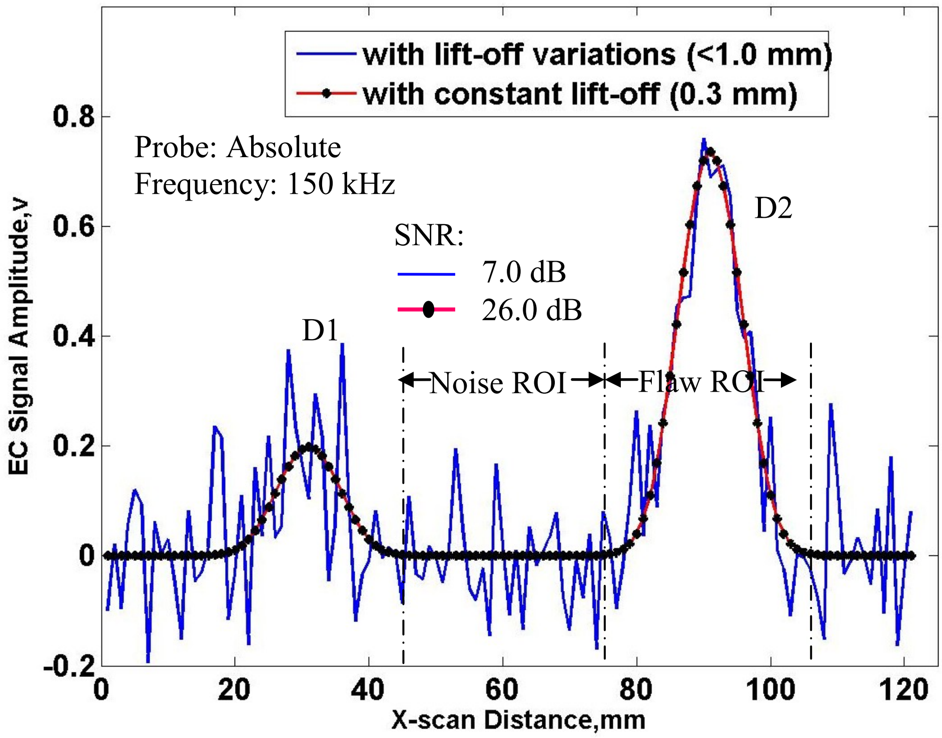

Figure 1.6 EC signals of two surface flaws (D1 and D2) acquired at constant lift-off and with variations in lift-off (0.0 mm to 1.0 mm).

The signal quality is being compared quantitatively on the basis on Signal-to-Noise Ratio (SNR) which is defined as logarithmic ratio of the mean value of the flaw signal (μ_{signal}) to the standard deviation of the noise (σ_{noise}) in the signal [14]. In the case of image, gradient vector in two orthogonal directions is estimated. The region having magnitude above an acceptable threshold is identified as the region of interest (ROI) of flaw. In the case of multiple flaws present in the image, the rectangular region around the smallest flaw (defect-ROI, refer Fig.4) is considered for estimation of SNR, region between two flaws is considered as the noise ROI.

The variations in lift-off reduced the SNR to 7 dB from 26 dB for the signals obtained at 0.3 mm constant lift-off. It depicts the ambiguity in detection of shallow flaws, due to the influence of lift-off variations.

1.3.2 Composite noise: Variations in material properties and lift-off

In austenitic stainless steel welds, inhomogeneous microstructure with a distribution of magnetic delta ferrite and variations in grain size are formed due to temperature gradient in the weld region during welding. These variations affect the electrical conductivity and magnetic permeability (termed as ‘material properties variations’ in the thesis) of the weld zone and produce large amplitude disturbing noise. As a result, it is difficult to detect flaws in the weld region.

Figure 1.7 (a) shows typical EC image from a weld region having two surface flaws of depths 0.25 mm and 0.5 mm at a constant lift-off of 0.3 mm at 75 kHz (δ=1.5 mm). Large amplitude noise due to the material properties variations resulting a SNR of -0.5 dB. Figure 1.7 (b) shows the EC image from the same weld region obtained by varying lift-off of 0.0 mm to 1.0 mm. Now, in addition to material properties variations, variations in lift-off produce composite noise masking the shallow flaws (Flaw 1, depth 0.25 mm, Flaw 2, depth 0.5 mm) in the weld region. It is clearly observed from Figure 1.7 (b) that composite noise degrades the SNR to -1.4 dB (Flaw 1, depth 0.25 mm) and reduces the sensitivity to detect shallow flaws.

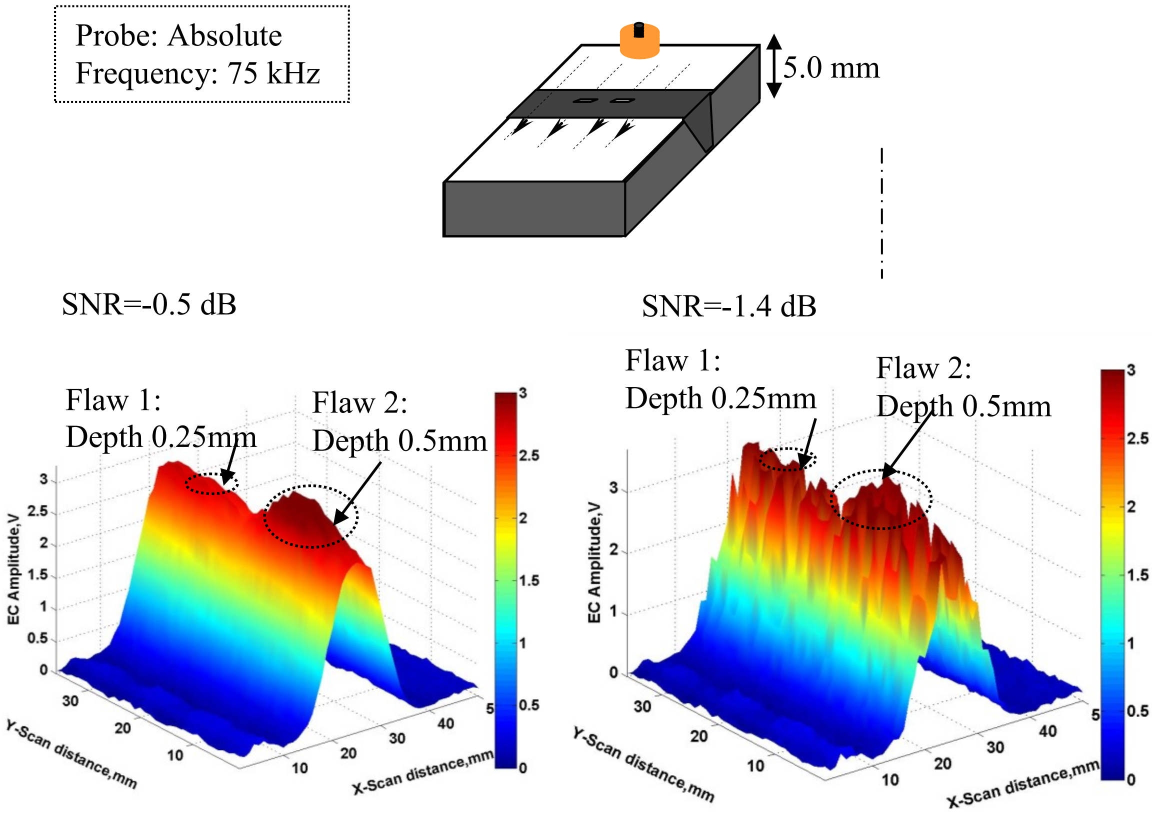

(a) Noise: material properties variations

(b) Noise: composite noise

Figure 1.7 EC images of two flaws of depths 0.25 mm and 0.5 mm (length 6.0 mm, width 0.25 mm) with (a) variations in material properties and (b) composite noise.

1.3.3 Composite noise: Variations in geometry and lift-off

Variations in geometry of the test object also influence the EC images. A typical example of this is the wall thickness variations in SS tubes due to die chattering and improper pilgering that produce periodic thickness variations. The EC image from two flaws of depths 0.075 mm and 0.15 mm (length 4.0 mm, width 0.1 mm) in a SS thin wall tube in the presence of wall thickness variations is shown in Figure 1.8 (a). The noise due to periodic wall thickness variations degrades the SNR (Flaw 1) to 0.2 dB [15]. Additional lift-off variations degrade the SNR (Flaw 1) to -0.5 dB. This clearly illustrates the challenge in flaw detection in the presence of composite noise.

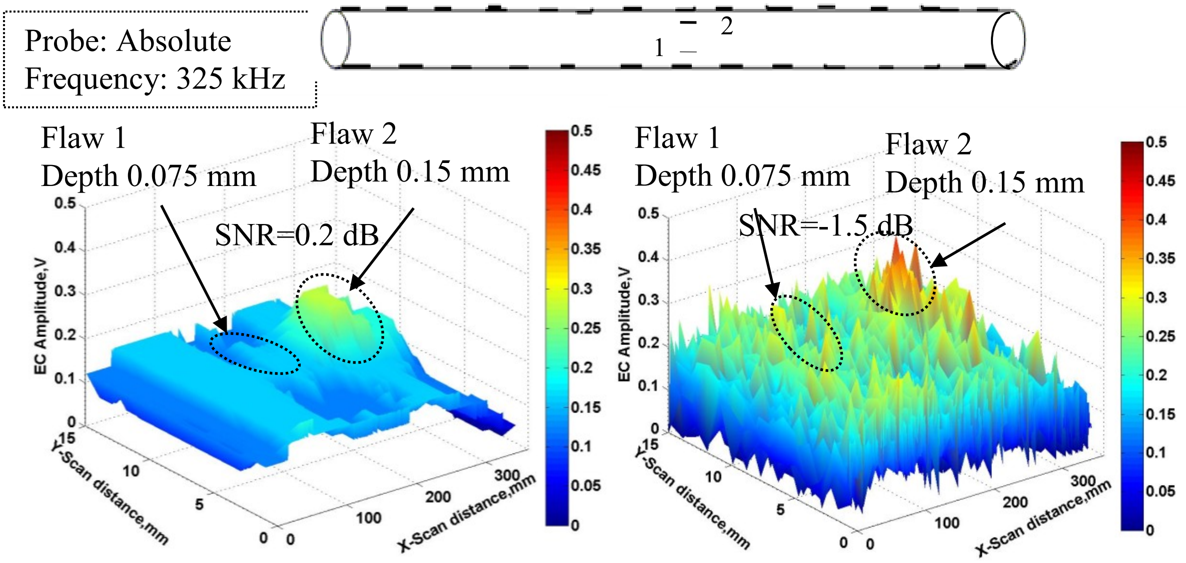

(a)Noise: wall thickness variations

(b)Noise: composite noise

Figure 1.8 EC images of two flaws in a thin wall SS tube with (a) wall thickness variations and (b) composite noise.

In order to extract information of flaws, processing of EC images is important for removing noise. This will enable identification of regions of the flaws and better characterisation of flaws.

1.4 Noise reduction methods

The EC data has time, frequency, and statistical information and their extent varies depending on the interaction of excitation energy with the test material. Hence, understanding the properties of information in terms of time, frequency and statistical characteristics is helpful for noise reduction. Filtering methods are used for noise reduction. These filtering methods are broadly classified into the following four major categories and their principles are discussed in detail in this section [16, 17]:

1) Time domain filtering

2) Frequency domain filtering

3) Time-frequency domain filtering

4) Statistical domain filtering

1.4.1 Time domain filtering

Time domain filtering is applied for removing additive noise and periodic noise. Mean, Maximum, Minimum and median filters are generally used for this purpose. This filtering involves operating a window mask of relatively smaller an image of size 3x3, 5x5 or 7x7 over an EC image and replacing the pixel with the computed value (mean, maximum, minimum, median, according to a filter). This is repeated for every step movement of the window. The mean filter reduces image blurring and yields a very good result for EC images corrupted by impulse noise while the median filter reduces large amplitude sparse spikes (salt and pepper noise). However, mean, maximum and minimum filters are not effective in complete removal of noise unless the noise characteristics are known [18].

1.4.2 Frequency domain filtering

Frequency domain filtering is applied for removing additive noise and periodic noise when the frequency characteristics of noise and desired information are distinct [19]. Low-pass, high-pass and band-pass filters are used in the Fourier transformed (FT) domain depending on the prior knowledge of the frequency content of the desired information. This frequency domain information is transformed back to time domain using inverse FT. Deconvolution can be applied in frequency domain (equation 1.10). However, this fails if the *psf* image is unknown and noise is very high. Another frequency domain filtering called, Wiener filter, forms the foundation of data dependent linear least square error filters [16, 20]. For an image with additive noise, the Wiener filter is obtained as

$$W(f) = \frac{P_{xx}(f)}{P_{xx}(f)+P_{NN}(f)} \qquad 1.11$$

where $P_{xx}(f)$ and $P_{NN}(f)$ are the signal and noise power spectra. Wiener filter recovers the desired information from noise, if their spectra do not overlap. Wiener filter has a drawback that it requires prior knowledge of desired information or the power spectral density of noise and flaw. The use of conventional frequency domain filtering technique is beneficial if the desired information and noise have separation in bandwidths.

1.4.3 Time-frequency domain filtering

Time-frequency filtering is applied when time localization of spectral components is needed. This type of filtering is widely applied to non-stationary time domain signals in which specified frequency components exist. EC signal of a flaw is a classical example of a non-stationary signal in spatial domain. Short time Fourier transform and wavelet transform are examples of time-frequency domain filtering. The wavelet transform (WT) processing provides the ability to examine and retain the frequency of a signal/image at different scales and resolutions as compared to the Fourier transform [21]. For numerical implementation of the wavelet transform two different types of techniques viz., continuous wavelet transform (CWT) and discrete wavelet transform (DWT) are used [22].

In the continuous wavelet transform, the signal is multiplied with a function called mother wavelet, and the transform is computed separately for different segments of the time-domain signal.

$$\psi_x(\tau, s) = \frac{1}{\sqrt{s}} \int x(t)\psi^*\left(\frac{t-\tau}{s}\right) dt \qquad 1.12$$

where $\psi(t)$ is the mother wavelet which is a continuous function in both time and frequency domains, τ is the translation factor that depends on time, and s is the scale factor which is a function of frequency [23]. Daughter wavelets are derived from the mother wavelet by varying the scaling factor. Thus, the frequency bandwidths of daughter wavelet filters are different from each other. The CWT coefficients $\psi_x(\tau\ s,)$ are obtained by cross-correlation of $x(t)$ with different daughter wavelet filters. The time-frequency localization property of the wavelet filters enables one to use them as band-pass filters at the bandwidth of the wavelet. Selection of mother wavelet is important. Usually a wavelet is selected such that its shape resembles the shape of the desired features in a signal [15].

Discrete wavelet transform was developed to save computation time by eliminating redundancy in CWT analysis. In DWT, as a first step, decomposition of signal into detail (high frequency components) and approximation (low frequency components) coefficients is done by employing a windowing technique with variable sized window enabling, dyadic sampling [24]. The next step involves, selective elimination of wavelet coefficients by thresholding. By performing inverse DWT using synthesis filter (discussed in the following section), denoised wavelet coefficients are reconstructed back into the time domain signal.

In 2D DWT, decomposition is achieved by use of separable and non-separable wavelet filters. A separable filter implies that filtering can be performed in one dimension (rows) followed by filtering in another dimension (columns) [25]. In sub-band decomposition, sub bands are logarithmically spaced in frequency and represent octave level decompositions. It provides unique directional information that is useful for an image representation and feature extraction at different scales [23].

An image is decomposed into four sub-bands and is schematically illustrated in Figure 1.9 (a). These sub-bands are formed by the application of horizontal and vertical decomposition filters. Sub-bands with label LH1, HL1 and HH1 correspond to finest scale coefficients while sub-band LL1 represents coarse level coefficients [26]. The LL1 sub band is further decomposed to find out the next coarse level of the wavelet coefficients as shown in Figure 1.9 (b).

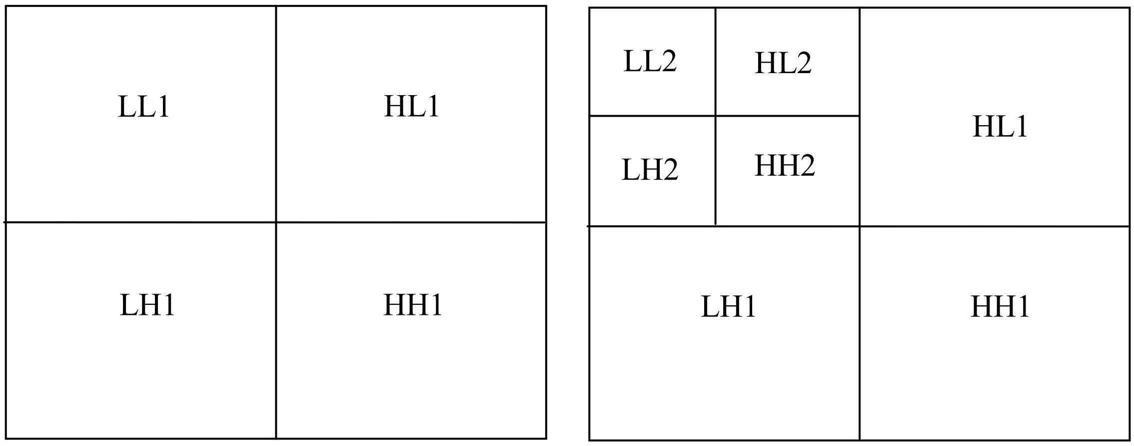

(a)-One level decomposition (b)-Two level decomposition

Figure 1.9 Typical denomination of sub-band 2D DWT.

The denoising performance of the wavelet processing of EC images depends on various parameters including the type of wavelet, thresholding method and threshold selection rules. Over the past decades, 47 different types unique wavelet filters have been identified and used. Selection of the best wavelet filter (within 47 wavelet filters) is very important, as it may affect the results of wavelet transform. The topic of wavelet selection has been addressed by various researchers and they are either qualitative or quantitative.

1.4.3.1 Qualitative measure for selection of wavelet

The wavelet filters are characterised by properties such as orthogonality, symmetry and compact support. An orthogonal wavelet is efficient in decomposing a signal into non-overlapping subfrequency bands. The orthogonality of a wavelet means that the scaling function *h(n)*, and wavelet function *g(n)* of wavelet are similar. The filter satisfies the following equality [27]:

$$g(n) = -1^n h(1-n) \qquad 1.13$$

The orthogonality between wavelet coefficients and scaling coefficients is defined as

$$\sum_n h(n)g(n) = 0 \qquad 1.14$$

The scaling coefficients, which satisfy equation 1.14 are called quadrature mirror filters.

On the other hand, the biorthogonal property is a generalisation of orthogonality where the scaling and the wavelet functions be neither of the same length and not even numbered. The scaling function is orthogonal to shifted version of wavelet function (*g(n)*) dual filter and satisfies the following equality and biorthogonal denomination comes from this feature.

$$\tilde{g}(n) = (-1)^n h(1-n) \qquad 1.15$$

Therefore, the quadrature mirror property is replaced with dual property. The filter coefficients are being symmetric leads to linear phase filtering. This is an important and required property for filtering operations. A compact support wavelet has nonzero basis function within a finite interval. This property allows the wavelet filters to efficiently represent signal/image that has localized features.

One approach to wavelet selection is based on geometric shape matching of wavelet filters [28, 29]. It was found that components in a signal may be extracted effectively when a base wavelet has the identical shape of the desired signal. As far as shape matching is concerned, it is generally difficult to accurately match the shape of a signal to that of a wavelet qualitatively. These deficiencies motivate the study on quantitative measures for wavelet selection.

1.4.3.2 Quantitative measure for selection of wavelet

The measures such as cross correlation, mutual information and distribution error have been used for wavelet selection [30, 31]. The energy content of a signal is a measure that uniquely characterises a signal. If a signal contains a particular frequency as the major component, then the wavelet coefficients corresponding to that particular scale will have relatively high magnitudes. Therefore, a wavelet filter that extracts maximum energy of the signal is considered as a optimal wavelet filter. Ambiguity arises with the presence of noise of same amount of energy in a number of scales. In that case, the spectral or energy distribution can be considered. The energy distribution between inter scale wavelet coefficients can be quantitatively described by entropy [32] as

$$E_{entropy}(s) = -\sum_{i=1}^{N} p_i \cdot log_2\, p_i \tag{1.16}$$

where $\sum_{i=1}^{N} p_i = 1$ and $p_i \log_2 p_i = 0$ if $p_i = 0$, where p_i is the energy probability distribution of wavelet coefficients. The entropy of the wavelet coefficients is bounded by

$$0 \leq E_{entropy}(s) \leq log_2\, N \tag{1.17}$$

in which $E_{entropy}(s)$ will be equal to a) zero when wavelet coefficients are zero except for one particular scale of coefficient, and b) $\log_2 N$, when wavelet coefficients are distributed for a number of scales (i.e., I/N). This reveals that an optimum wavelet should yield larger magnitude of a few wavelet coefficients at a particular scale than at other scales, leading to the minimum entropy.

1.4.3.3 Wavelet thresholding

The well known wavelet-based denoising depends on thresholding of wavelet coefficients [33]. Threshold optimisation is the center of many studies in signal or image enhancement.

Donoho proposed a procedure for denoising i.e., i) decomposition of the image into wavelet coefficients, ii) comparing the detail coefficients with a threshold value, iii) shrinking these coefficients close to zero to eliminate the effect of noise in the image and iv) reconstruction of image from the modified coefficients [34].

Hard and soft thresholding techniques are used for image denoising. Hard thresholding eliminates all coefficients smaller than a threshold and leaves the other without any change. On the contrary, soft thresholding shrinks the coefficients above a threshold. Mathematically hard and soft thresholds are expressed as:

$$\textit{Soft thresholding: } \hat{x} = sign(x)(|x| - \lambda_t) \qquad 1.18$$

$$where\ \Theta_s\ (x, \lambda_t) = \begin{Bmatrix} \hat{x}\ for\ |x|\ \geq \lambda_t \\ x\ for\ |x| \leq\ \lambda_t \end{Bmatrix} \qquad 1.19$$

$$\textit{Hard thresholding: } \Theta_H(x, \lambda_t) = \begin{Bmatrix} x\ for\ |x|\ \geq \lambda_t \\ 0\ for\ |x| \leq\ \lambda_t \end{Bmatrix} \qquad 1.20$$

Finding an optimum value for thresholding is an important task. The smaller threshold will pass all coefficients correspond to noise and resultant images may still be noisy. On the other hand, larger threshold makes more number of coefficients to zero, which provides image smoothness, blurring and loss of desired information related to flaws.

Commonly used threshold methods are universal threshold, minimax, Sqtwolog, Rigrsure and Heursure methods. The universal threshold estimates $\lambda = \sigma\sqrt{2\log N}$ where N is the number of pixels and σ^2 is the noise variations. The number of samples is large, then the universal threshold gives better results with soft threshold. The minimax estimates an optimal threshold in terms of L^2 risk (minimum value from the mean square error). Sqtwolog estimates the threshold equal to the square root of logarithm of the signal length (N). SureShrink is an adaptive threshold estimator based on Stein’s Unbiased Risk

Estimator (SURE) and was proposed by Donoho and Johnstone [35]. It is a combination of universal threshold and SURE threshold. In this method, threshold estimate is assigned through the principle of minimising SURE to each dyadic resolution level. The threshold λ_t by SureShrink is defined as

$$\lambda_t = argmin_\lambda SURE = argmin_\lambda \left[N - 2.\#\{k: |x_{j,k}| \leq \lambda\} + \textstyle\sum_k^N min(|x_{j,k}|, \lambda)^2\right] \quad 1.21$$

The goal of SureShrink is to minimise the mean squared error

$$MSE = \frac{1}{n^2} \textstyle\sum_{x,y=1}^{n} (z(x,y) - s(x,y))^2 \quad 1.22$$

where z(x,y) is the estimate of the signal while s(x,y) is the original signal without noise and n is the size of the signal. In spite of the high performance, Donoho and Johnstone in pointed out that SureShrink in extremely sparse and wavelet representations might obtain an inadequate threshold [35].

Chang et.al. proposed Bayes Shrink and it estimates a threshold value that minimises the Bayesian risk assuming Generalised Gaussian Distribution (GCD) prior [36]. In Bayesian risk minimisation, $\hat{x}$ is estimated by the transformation of the given noisy image y using a decision operator D as $\hat{x}$=Dy. The optimal operator D is defined as

$$D = argmin_D R(D) = argmin_D E[\|\hat{x} - x\|^2] \quad 1.23$$

Suppose $x_{j,k}$ is a set of wavelet coefficients, $y_{j,k}$ is the noisy image and x is the thresholded image, then minimising the difference between x and $\hat{x}$ is called risk minimisation. The prior probability should be known to minimise the risk R for Bayesian approach. The BeyesShrink threshold minimises the Bayes risk and is described as

$$R(\lambda_t) = E(\|\hat{x} - x\|^2) = E_x E_{y|x}(\|\hat{x} - x\|^2) \quad 1.24$$

On the other hand, Rigrsure estimates threshold based on the principle of minimising the Stein's Unbiased Risk Estimator. Heursure is a hybrid scheme of the Rigrsure and Sqtwolog and this is useful to avoid over smoothing [37].

1.4.3.4 Reconstruction

The reconstruction of the wavelet denoised coefficients is carried out by computing inverse 2D DWT by use of synthesis filters $g^{-1}(n)$ and $h^{-1}(n)$ determined by the equation (1.16), for each sub-level decomposition [38]. It may be noted that reconstruction is the mirror image of decomposition and associated with up sampling by a factor of two so that the reconstructed image can be shown in the original resolution. The schematic of 2D decomposition through scaling and wavelet function and reconstruction through synthesis filtering is shown in Figure 1.10.

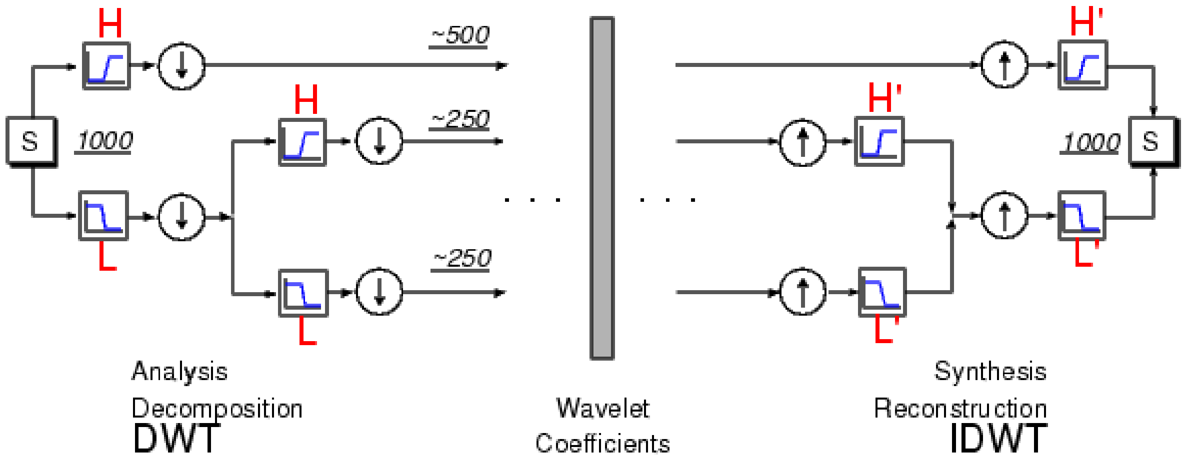

Figure 1.10 2D decomposition and 2D synthesis filtering for image reconstruction [22].

1.4.4 Statistical domain filtering

Apart from analysing the frequency contents of EC data, statistical nature of the data can be considered for noise reduction. The statistical characteristics of EC signals of noise and flaw are studied in terms of their probability distribution. Figure 1.11 (a) shows the signal from a flaw and the corresponding probability density function (*pdf*). The EC signal of composite noise (variations in material properties in weld region) and its corresponding *pdfs* are shown in Figure 1.11 (b).

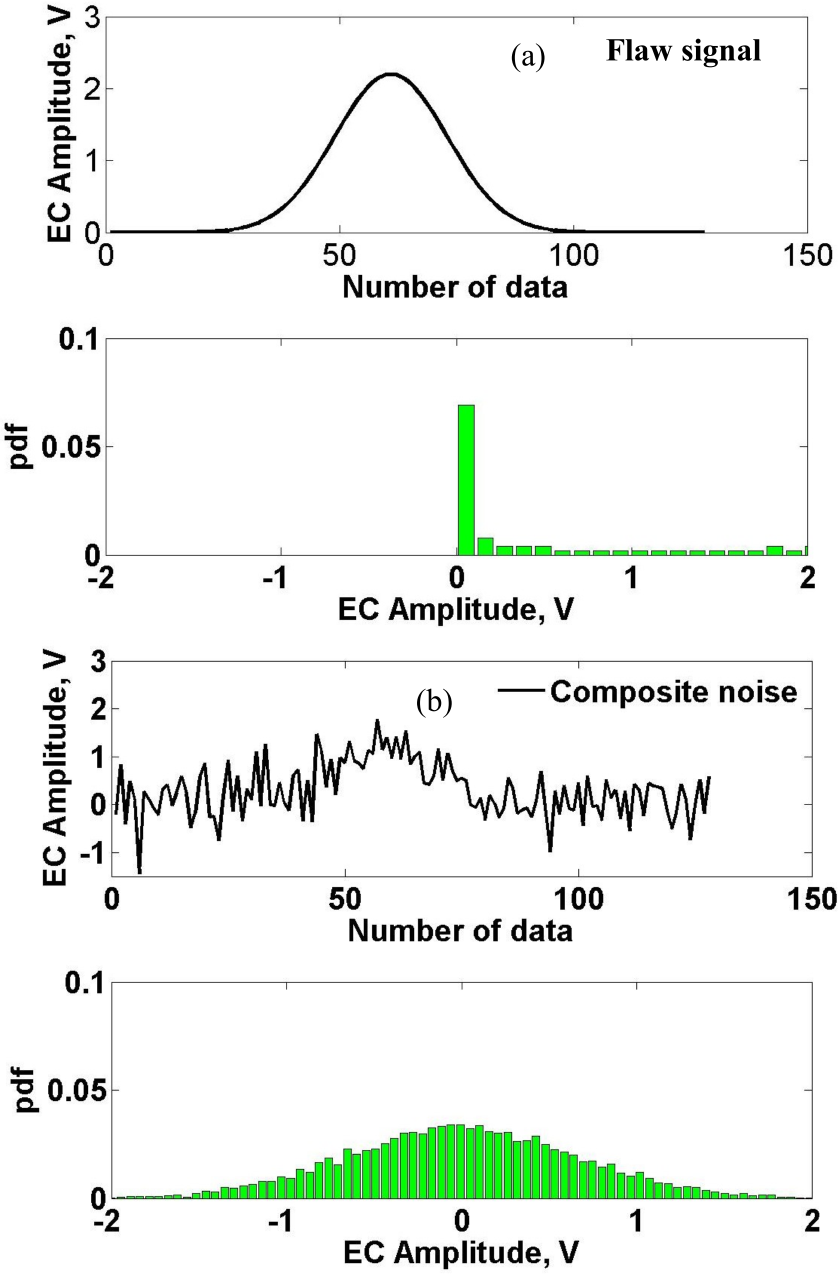

Figure 1.11 EC signal and *pdf* of (a) flaw alone (b) composite noise.

As per central limit theorem, Gaussian distribution of composite noise gives the evidence that the composite noise is independent variable and has statistical independency. As clearly seen from the figures, statistically independent nature of noise shows Gaussianity and distinct from flaw information. This indicates the measure of Gaussianity in the EC image can be used for identification of noise. The statistical technique that utilises information of variance and entropy of the signal or image called, blind source separation technique, is found attractive. Two promising blind source separation techniques are Principle Component Analysis (PCA) and Independent Component Analysis (ICA). The PCA and ICA techniques utilise variance and Kurtosis as a statistical measure to provide linear transformation of data to a new coordinate system. Principal component analysis Principal component analysis is a method of linear transformation of data to a new coordinate system with order of variations (principal components). Schematic projection of data and their Eigen value as a new coordinate system are shown in Figure 1.12 (a) and (b) respectively. The transformation process of data through decomposing and reconstruction is termed as Karhunen Loeve (KL) transform [39]

1.4.4.1 Principle component analysis

The KL transform calculates the Eigen values (λ) and Eigen vectors (ν) of covariance matrix **C**. Further the principal component K is estimated by multiplying the normalised input data (B) with the transpose of the Eigen vector matrix and is expressed as

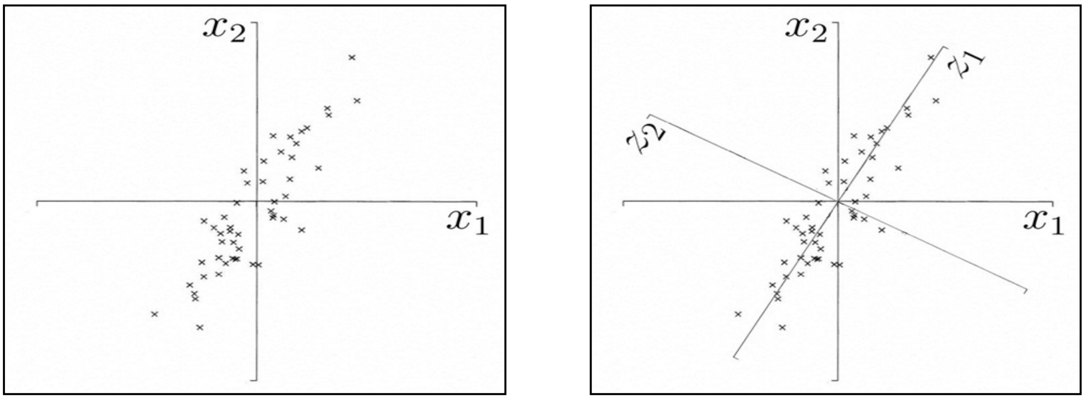

(a) 2D data on Cartesian coordinates (b) Projection of the data on coordinates

Figure 1.12 Principal component analysis of 2D data.

$$K = \nu^T * B \qquad 1.25$$

KL transform has been used as noise reduction method in EC testing [40, 41]. The PCA technique has been utilised to improve the quantification of the pulsed eddy current signals for flaw detection and to classify cracks located in the second lower layer of aircraft lap-joints [42, 43]. The literature survey on these topics found the use of PCA, to optimise the feature set of EC signals.

1.4.4.2 Independent component analysis

Independent component analysis separates a multivariate signal into additive subcomponents by assuming that they are all statistically independent of each other. ICA aims to maximise the statistical independence of noise (unconstrained sources) and at the same time reducing the divergence among the spatially constrained source [44]. ICA is often described as an extension to PCA that un-correlates the signals of higher order moments and produces a non-orthogonal basis. PCA and ICA techniques provide linear transforms and they differ the way statistical information is utilised to carry out the transform. However, the information in signals is mutually correlated, PCA technique fails to process the signals that are independent of each other.

ICA technique transforms the input signals into the ICs subspace, where the direction of the components is statistically independent. Suppose N statistically independent signals, $\phi\ (t)$, i = 1,... N is measured using N sensors and resulted N observation signals $x_i(t)$, i = 1, ...N and are linear mixtures of N statistically independent components S_i. A fundamental aspect of the mixing process is that the sensors must be spatially separated (e.g. microphones that are spatially distributed around a room) so that each sensor records a different mixture of the sources. With this spatial separation assumption, mixing process with matrix multiplication is written as

$$X_i = a_1S_1 + a_2S_2 + ... + a_nS_n \qquad 1.26$$

The entire system of *n* measured signal as X=AS where **A** is an nXm matrix containing the characterised mixing coefficients for the linear mixture [45]. The independent components are obtained from the estimation of **W,** known as de-mixing matrix ($\mathbf{A^{-1}}$), as.

$$S=WX \qquad 1.27$$

It is based on the postulation that the sum of two independent signals usually has a distribution that is closer to Gaussian distribution of the two original signals. According to the central limit theorem the distribution of a sum of independent signals with arbitrary distributions tends a Gaussian distribution. Thus a Gaussian signal can be considered as a linear combination of many independent signals. Schematic projection of multivariate distribution of Gaussian variables and non-Gaussian variables is shown in Figure 1.13 (a) and (b) respectively. The data in Figure 1.13 (b) are clearly divided into two clusters.

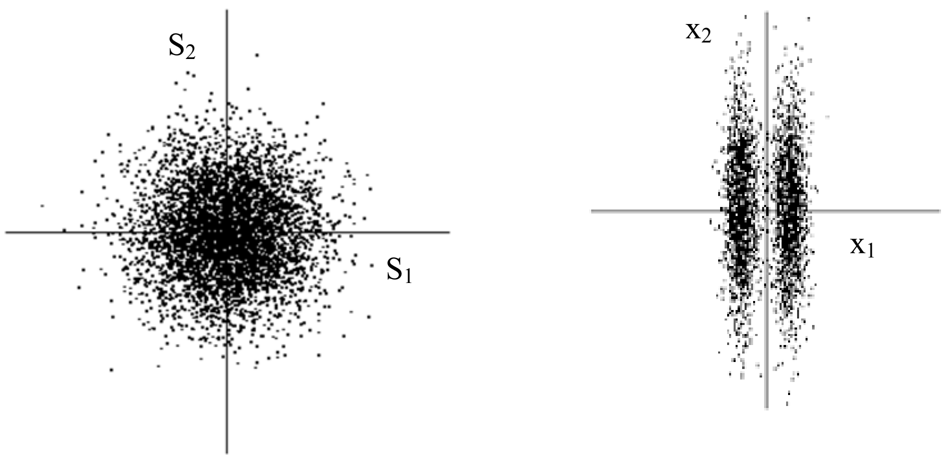

(a) (b)

Figure 1.13 Independent component analysis of 2D data.

The direction of maximum variance (principal component) along the vertical provides no separation between the cluster, while non-Gaussianity along the horizontal provides optimal separation of the clusters.

Non-Gaussianity is an important and essential principle in the estimation of mixing matrix **A**. To use non-Gaussianity for estimation of **A**, there needs to be a quantitative measure of non-Gaussianity of a signal. Two commonly used measures are Kurtosis and entropy.

The Kurtosis of a signal (s), is defined by [46]

$$kurt(s) = E\{s^4\} - 3(E\{s^4\})^2 \qquad 1.28$$

when data is pre-processed to have unit variations and zero mean, Kurtosis is equal to the fourth moment of the data where $E\{s^2\}$=1. For a Gaussian signal, $E\{s^4\} = 3(E\{s^4\})^2$ and hence, its Kurtosis is zero. The Kurtosis is zero for Gaussian random variable and non-zero for non-Gaussian random variables. Random variables that have a negative Kurtosis is called sub-Gaussian (flaw) and with positive Kurtosis is called super-Gaussian. Kurtosis has been widely used as measure of Non-Gaussianity in ICA because of its computational, theoretical and simplicity.

From the information theory, entropy is considered as the measure of randomness of a signal. Entropy H of discrete-valued signal s is defined as

$$H(S) = -\sum P(s = ai) \log P(s = ai) \qquad 1.29$$

This definition of entropy can be generalised for a continuous valued signal (s), called differential entropy, and is defined as

$$H(S) = -\int p(s) \log p(s)\, ds \qquad 1.30$$

The information theory states that Gaussian signal has the largest entropy. For the signals that have spiky *pdf*, i.e., when the variables are clearly clustered, entropy will be small [47]. The problem in using differential entropy is, however, that it is computationally difficult to determine and it requires an estimate of the *pdf.* To avoid the problems encountered with the differential entropy, new approximations were developed based on the maximum entropy principle as

$$J(y) = \sum_{i=1}^{p} k_i \left[E\{G_i(y)\} - E\{G_i(\nu)\}\right]^2 \qquad 1.31$$

where k_i are positive constants, ν and y are Gaussian variable of zero mean and unit variance, G are the non quadratic functions and are

$$G_1(u) = \frac{1}{a_1} \log \cosh a_1 u \qquad 1.32$$

$$G_2(u) = -exp\,(-u^2/2) \qquad 1.33$$

where $1 \leq a1 \leq 2$ is a constant. The non-Gaussianity measured by the approximation of *J(y)* can also be iteratively used such that the direction at which **WX** maximises the non-Gaussianity and minimises the randomness in the estimation of **W** [48].

The *pdf* of noise in EC images (refer Figure 1.11), shows Gaussian distribution. As per the central limit theorem, the linear combination of noise having statistical independence shows Gaussian distribution, gives the evidence that the noise in EC images are of statistically independent. The statistical independence of data is measured in terms of Gaussianity and ICA that utilises the measure of Gaussianity for separation of statistical independent information is a promising technique for noise removal in EC images.

Before performing ICA preprocessing steps of centering and whitening are generally carried out. The centering step is commonly performed by subtracting the mean (m) of the data (x). This results in centered data X_c as

$$X_C = X - m \qquad 1.34$$

This step simplifies the ICA algorithm, and de-mixing matrix is estimated using the centered data. The whitening on data involves linearly transforming the data such that which are uncorrelated have unit variance. To perform whitening transformation, Eigen value decomposition of data X is used.

$$E\{XX^T\} = I = VDV^T \qquad 1.35$$

where V is the matrix of Eigen vectors of $E\{XX^T\}$ and D is the diagonal matrix of Eigen values i.e., D=diag $\{\lambda_1, \lambda_2, \ldots \lambda_n\}$. Whitening transforms the mixing matrix into a new orthogonal coordinate system

$$E\{XX^T\} = AE\{SS^T\}A^T = AA^T = I \qquad 1.36$$

Whitening thus reduces the number of parameters to be estimated. Instead of having to estimate the new elements of the matrix X_c, the orthogonal matrix has n(n-1)/2 degrees of freedom. This step of whitening significantly reduces the computational complexity of the ICA.

1.5 Summary

Eddy current testing is important for nondestructive detection of flaws in stainless steels used in nuclear and other industries. EC signals are used for detection of flaws while EC imaging is beneficial for three dimensional representations of flaws. EC techniques are simultaneously influenced by variations in surface roughness, probe lift-off, electrical conductivity, magnetic permeability and geometrical variations and are reflected as noise in EC images. Noise reduces the detection sensitivity to shallow flaws that are detrimental to the structural integrity of engineering components. The removal of noise by using several filtering techniques in time, frequency, time-frequency and statistical domains are discussed. Among them, DWT based on multiresolution analysis and ICA based on statistical characteristic of noise are found promising, for removal of noise in EC images.

Chapter 2 : Literature review and motivation

Preamble

This chapter covers the reported literature on noise removal in eddy current NDE. It also identifies the gap areas based on the literature survey, which has helped in setting the motivation and identifying the objectives of the research work. This chapter also outlines the organization of the thesis.

2.1 Literature Survey

As discussed in Section 1.3, variations in lift-off, material properties and geometry produce large amplitude noise in EC images and degrade the detection sensitivity of the technique. Hence, denoising is an essential step for reliable detection of flaws. Several approaches were proposed by many researchers for noise removal [41-49].

Koyama et.al., developed an EC probe consisting of a wide tangential exciting coil (length 40.0 mm, width 30.0 mm, height 30.0 mm) and differential receiver coils (length 4.0 mm, width 1.0 mm, height 7.0 mm) for elimination of noise by weld zone in AISI 304 stainless steel plates [49]. The tangential coil was designed for inducing uniform eddy currents in the plate and a differential receiver coil was used for detecting the normal component of the induced magnetic field. In this study, detection performance of a conventional pancake probe (10.0 mm outer diameter) and the uniform eddy current probe was compared. The schematic of the uniform EC probe is shown in Figure 2.1 (a). ECT of weld zone was conducted with SS plates of 1.9 mm thick having a flaw of length 5.0 mm, width 0.2 mm and depth 1.7 mm in the weld zone (width 5.0 mm) using the pancake probe and uniform EC probe at a test frequency of 70 kHz. Figure 2.1 shows the EC image obtained for a flaw perpendicular to the weld centreline using the pancake probe and using the uniform

EC probe. They reported that the uniform EC probe was less influenced by weld variations due to the self-nulling feature of the probe as compared to the pancake probe [49]. They reported that for flaw detection on the surface of the weld zone, repeated scans with change in the direction of the probe is necessary, thus the testing is time-consuming.

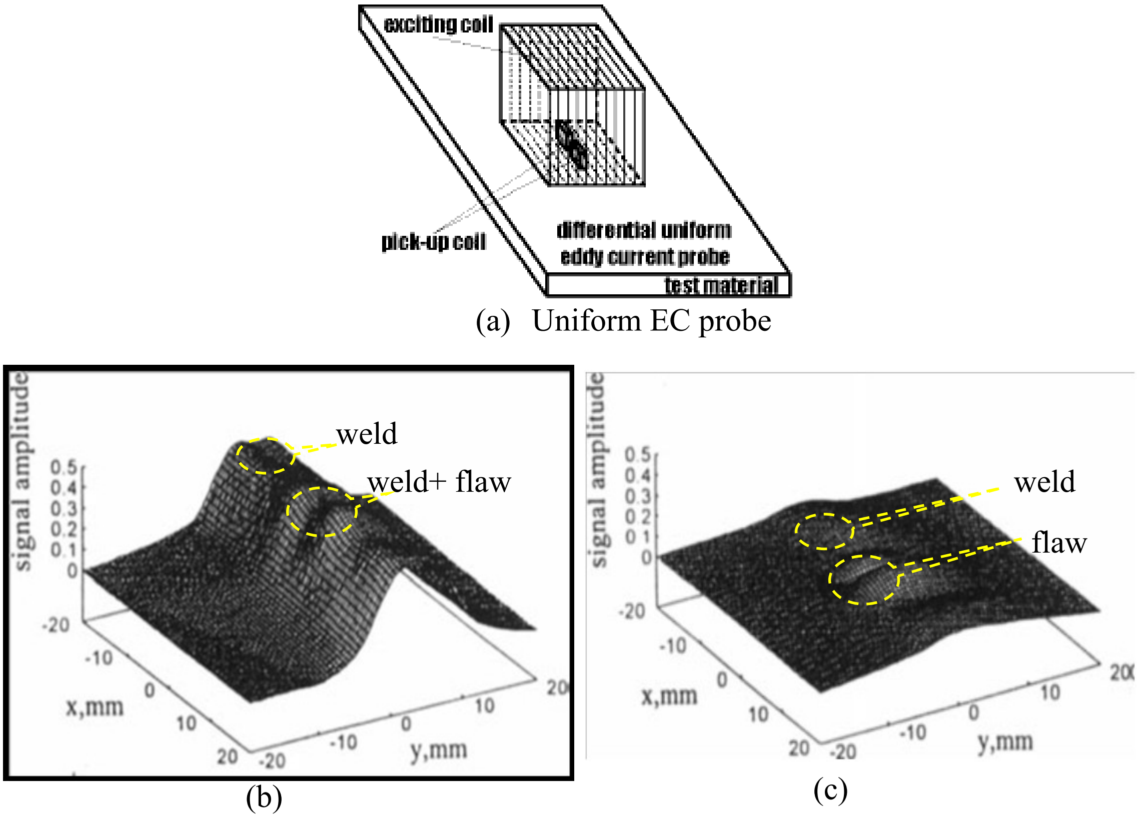

Figure 2.1 (a) Structure of the uniform EC probe, EC images of a flaw of depth 1.7 mm in a weld zone using (b) pancake probe and (c) uniform EC probe [49].

Xiang et.al., developed a multifrequency rotating EC probe system that consists of two pancake probes and one plus point probe having two coils oriented orthogonal to each other, to reduce the influences from support plate and probe wobble during ECT of steam generator tubes [50]. Figure 2.2 (a) shows the schematic of the rotating probe and typical EC image from a steam generator tube having axial and circumferential flaws.

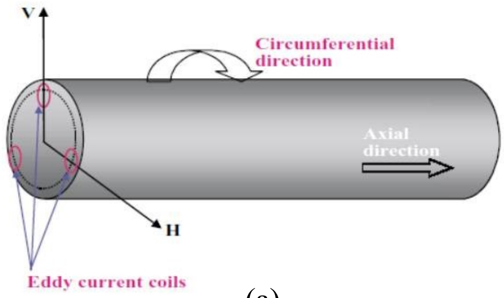

(a)

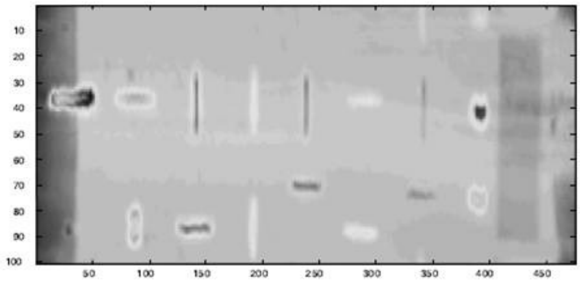

(b)

Figure 2.2 (a) Rotating probe geometry and (b) EC image from steam generator tube.

In addition to probe design, several researchers reported filtering techniques such as median filter and low pass filter as a pre-processing tool to reduce noise in EC signals [42, 51]. Udpa *et al*. used a few variant Fourier descriptors to estimate depth of flaws in heat exchanger tubes and under support plates [52]. Rao *et al*. proposed an intelligent imaging scheme using artificial neural network for fast and automated detection, imaging and characterization of surface flaws in 3.0 mm thick SS plates and reported a tenfold reduction in inspection time without compromising the probability of flaw detection [53].

The Fourier filtering technique has been applied to EC signals having unique and different frequency components for flaws and noise. For elimination of noise by Fourier filtering, prior knowledge of desired signal or the power spectral density of both noise and flaw is required [54]. However, due to the attractive properties like sparsity, edge detection and multiresolution, wavelet transform (WT) has gain popularity for spatially adaptive filtering applications e.g. for elimination of undesired signals [36].

Lopez et.al., applied discrete wavelet transform (DWT) for denoising the probe wobble noise caused by slack between EC probe and tube walls of steam generator tubes. They studied the efficiency of using four selected wavelet filters (Haar, Birothogonal 3.5, Biorthogonal reverse 3.5, Daubechies 5) on EC signals acquired from a SS tube (19.05 mm internal diameter, 1.24 mm wall thickness) having two artificial through holes of 0.9

mm and 1.1 mm diameter [55]. The efficiency of four wavelet filters was compared by the retention of unchanged flaw amplitude. They observed that Db5 wavelet could efficiently remove the noise without reducing the flaw amplitude as compared to others. They attributed this performance to wavelet function shape that closely matches the EC signal of the holes.

Thriunavukkarasu et.al., compared the noise reduction as well as enhancement of remote field eddy current (RFEC) signals of flaws in bend region of steam generator tubes using Fourier filtering, cross-correlation and wavelet transform based techniques [56]. The noise considered to be from expansion bend regions, exciter–receiver coil misalignment, bending stresses, probe wobble and magnetic permeability variations that hindered detection of flaws. They reported that CWT based technique can unambiguously detect 10% wall loss present in the bend region with a SNR better than 7 dB.

It is interesting to learn from literature that correct choice of wavelet and selection of the wavelet coefficients are important for reduction of noise. There have been efforts to estimate the threshold for coefficients. Commonly used threshold selection methods are universal threshold, minimax, Sqtwolog and Rigrsure and Heursure methods. The threshold selection algorithms have been studied by Lazaro et.al., with three different rules (a) universal, (b) minimax and (c) SURE for different wavelet filters and stated that the universal threshold has given the best SNR [57]. The studies of Pardo et.al., with SURE threshold, has shown better performance than universal and minimax thresholds [54]. However, information related to the applicability of the wavelet threshold selection method for noise removal in EC images is scarce. A systematic study on the comparative performance of the Heursure, Rigrsure and Sqtwolog methods on EC image denoising is beneficial for reliable detection of flaw with minimal reduction in amplitude.

Apart from the frequency and wavelet transform based filtering techniques, application of statistical techniques are also reported for noise reduction. Principal component analysis (PCA), technique was reported for enhanced detection of flaws in aeronautical lap-joints [58, 42]. Diraison *et al.* employed imaging film based EC imager for detection of buried flaws in aeronautical lap-joints in the presence of large amplitude noise from the rivets. They applied PCA technique and observed that it successfully separated the noise from the rivet structure [59]. Rao *et al.* reported application of PCA technique for noise reduction and for enhancement of magnetic flux leakage images of flaws in carbon steel plates [60]. Kalyanasundaram *et al.* proposed an Eigen value based approach for enhancement of EC images. In this approach, Eigen pairs having maximum information related to flaws are determined and utilised to reconstruct noise-free images [61].

Shin et.al., applied ICA technique to ECT data from steam generator tubes with support plate. They studied the separation of signals due to flaw and support plates and observed the successful separation of both the signals. They added random white noise (50 dB of signal power) and evaluated the performance of the ICA technique to filter the noise. They observed higher SNR and reported that ICA technique can be used to reduce noise in EC signals [62].

Joubert et.al., investigated the application of PCA and ICA techniques to separate signals of rivets from flaw response during the inspection of riveted lap-joints. They observed that the separation efficiency of the PCA technique increases monotonically with length of flaw [63].

2.2 Motivation for research

Shallow flaws (depth less than 10% of wall thickness) in engineering components are detrimental. Hence, early detection of shallow flaws in engineering components is desired. Disturbing noise due to variations in lift-off and material properties during EC testing of stainless steel plates and welded structures is a concern. The need for improving detection sensitivity for smaller flaws in the presence of noise has stimulated interest to investigate and develop approaches for removal of noise in EC images, obtained especially during remote EC inspection of curved SS plates and weld regions.

As inferred from the literature discussed in Section 2.1, studies on noise removal are limited to processing signals or images influenced by noise due to one disturbing variable at a time. However, in practice, the images are simultaneously influenced by disturbing noise from different sources like variations in lift-off, material properties and geometry. Development of image processing methods for removal of such noise is challenging. Systematic investigations have not been reported in processing the EC images to eliminate this composite noise. Hence, there is a strong need to develop image processing approaches that can simultaneously remove noise in EC images.

Studies reported in open literature show that time-frequency based wavelet transform method is promising for denoising of EC images of flaws. However, systematic studies related to the selection of optimum wavelet, decomposition level, selection of wavelet coefficients and thresholding methods for EC images are very limited. For automated selection of optimal wavelet among the available 47 wavelet filters and suitable optimum decomposition level there is no clear cut approach reported in the literature. Hence, there is a need to evolve an approach for automated selection of an optimal wavelet and thresholding method to efficiently reduce noise in EC images. Information related to wavelet processing of such composite noise is limited. It is worth studying the performance of the DWT based processing approach for handling composite noise in EC images.

Literature survey reveals that the statistical domain based PCA and ICA techniques are being increasingly applied to EC signals and images of flaws. It is interesting to note that the composite noise due to different disturbing variables (random) follow Gaussian distribution according to the central limit theorem. In this context, it may be beneficial to develop ICA based processing approach, exploiting the Gaussianity of the noise and the non-Gaussian nature of the desired information of flaws in EC images.

Exploiting the statistical independence of noise as well as the spatial frequency localization of flaws by DWT in a sequence of processing is attractive to remove the composite noise and to retain the flaw amplitude in EC images. A clear benefit exists with a study to identify the most optimum sequence of a processing approach using DWT and ICA techniques and develop a hybrid image processing approach. A detailed study in this regard is beneficial and desired for automated detection of shallow flaws from EC images of austenitic stainless steel plates and welds.

2.3 Objective of research

The objective of the research work is to develop image processing approaches for removal of composite noise from EC images of flaws in stainless steel plates and welds. In order to achieve this, studies are focused on developing approaches that exploit the statistical independency of composite noise and the spatial frequency localization of flaws in EC images. The research is focussed towards removal of noise in EC images and no efforts are made to enhance the flaw information. The following are the objectives of this research:

- To develop DWT based approach for reduction of noise in EC images based on automated selection of wavelet filter, decomposition level, and thresholding and evaluation of performance of the approach
- To develop ICA based approach for reduction of noise in EC images based on iterative estimation of mixing matrix for separation of statistically independent component and evaluation of performance of the approach
- To develop a hybrid image processing approach that combines the capabilities of the DWT based approach and the ICA based approach for removal of composite noise in EC images and evaluation of performance of the hybrid approach

2.4 Organisation of the thesis

The thesis has been organised in four major chapters addressing the set of objectives, towards establishing effective noise reduction in eddy current images, as given below:

Chapter 3 presents the experimental set up developed for eddy current imaging on planar and tubular geometries. It also describes the details of noises and flaws considered for experimental investigations. The chapter proposes two new parameters viz Noise Reduction Percentage and Flaw Reduction Percentage to assess the noise reduction and flaw retention capabilities of the proposed approaches.

Chapter 4 discusses the development of DWT based image processing approach for automated removal of noise in eddy current images. The chapter proposes criteria for optimisation of wavelet filter, decomposition level, and selective elimination of noise through the implementation of semi-local paradigm for wavelet thresholding method. The chapter also discusses the denoising ability of the proposed approach.

Chapter 5 details the development of ICA based approach for reduction of noise in EC images based on iterative estimation of de-mixing matrix for separation of statistically independent component. The performance of the ICA based approach has been analysed and compared with that of the DWT based approach in this chapter.

Chapter 6 discusses the development of a hybrid image processing approach that combines the capabilities of the DWT based approach and the ICA based approach for efficient removal of composite noise in EC images. This chapter also discusses the experimental investigations carried out to study the influence of test parameters on noise removal.

Chapter 7 summarises the major conclusion drawn from the research work and provides the scope for future research.

Chapter 3 : Experimental details

Preamble

This chapter provides the details of three modules (EC instrument, scanning system and data acquisition system) essential for EC imaging on planar and tubular geometries of specimens.

EC images of flaws representing real testing conditions are considered for reduction of noise using the DWT based and ICA based image processing approaches. Experimental imaging that maps the electrical conductivity and magnetic permeability at a point of interrogation of probe in the test specimen is carried out. In order to represent the real world flaws, artificial (EDM) notches of different dimensions are machined by electro-discharge machining (EDM) process in stainless steel specimens of planar, welded and tubular geometry are considered.

3.1 Design of imaging setup

The imaging setup is designed for acquiring experimental images from plates and tubes having single and multiple flaws. The schematic of the experimental imaging setup used to carry out raster scan is shown in Figure 3.1. This setup consists of three important modules viz. i) EC instrument comprising of signal generator and probe, ii) automated scanner, and iii) data acquisition system.

3.1.1 EC instrument

The EC instrument consists of a sine wave generator, signal conditioning circuit, demodulator and display unit. The sine wave generator generates a single or two frequency sine waves for excitation of the EC probe. The output of the sine wave generator is conditioned and this energizes the EC probe. The change in impedance of the EC probe is measured in terms of voltage using a Wheatstone bridge circuit. The measured voltage is separated into resistance (horizontal) and a reactive (vertical) component by a phase discriminator circuit and the response is displayed in xy plane known as the impedance plane diagram. A commercial EC instrument-Model Insis EX-4 (supplied by M/s. Technofour) is used.

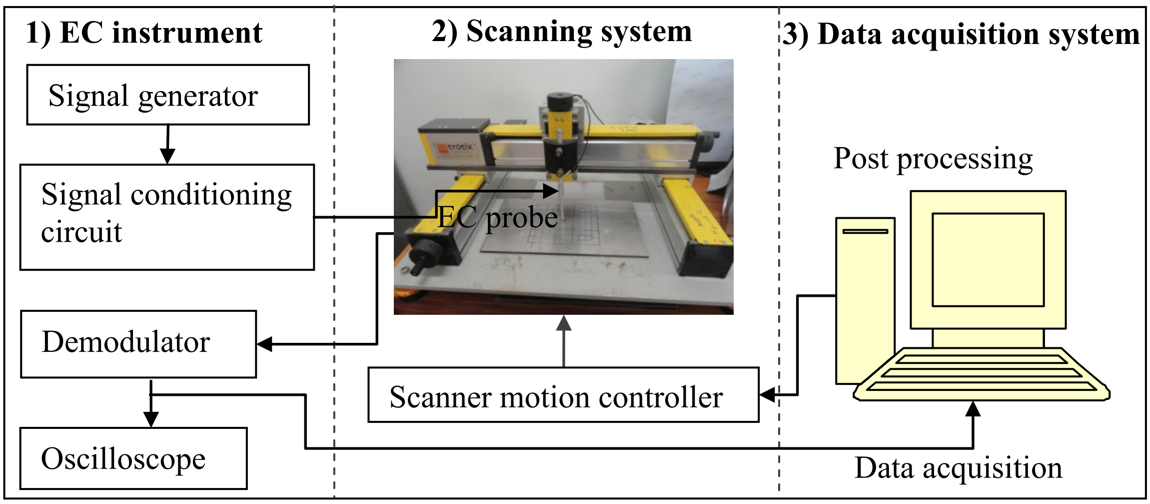

Figure 3.1 Block diagram of the EC imaging setup.

3.1.2 EC probe

Surface absolute type (pancake) probes are used for testing of plates as well as tubes. Probes of 3.0 mm, 5.0 mm and 20.0 mm diameter having wide range of operating frequency from 50 kHz to 500 kHz are used. The operating frequencies of 75 kHz (2δ) and 150 kHz (1δ) are used for imaging of the stainless steel plates. For imaging of stainless steel tubes, pancake probe of 3.0 mm diameter operating at 350 kHz is used.

3.1.3 Scanning system

The XY scanning system used for imaging of plates consists of stepper motor controlled X and Y scanning arms and a holder for mounting the EC probe. The scanner has a maximum coverage area of 500.0 mm x 500.0 mm. The minimum possible scan pitches for both X and Y stages are 0.01 mm and the reposition accuracy is 0.01 mm. The EC instrument is interfaced to the XY scanner for automated raster scanning of the EC probe over the SS plates and welds. The scanner is controlled using a NI PCI-7330 motion control card and LabVIEW software. The raster scanning at 1.0 mm/s is synchronised with the data acquisition system to acquire data at discrete points during the raster scanning. Figure 3.2 shows the photograph of the setup used for EC imaging of plates.

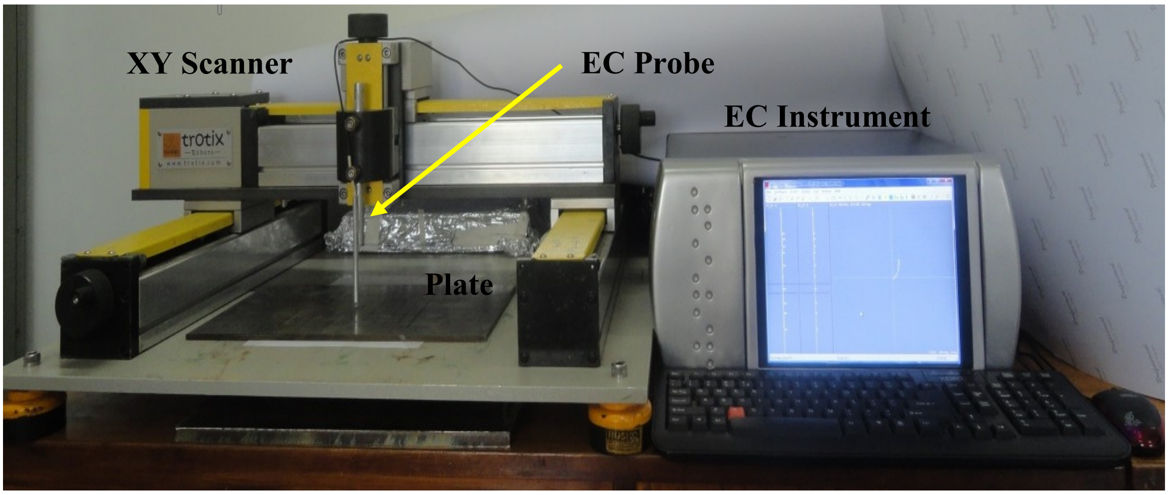

Figure 3.2 Photograph of the setup used for EC imaging of plates.

For EC imaging of flaws in tubes, Z θ scanner is used. The EC instrument is interfaced to the Z θ scanner and controlled using NI PCI-7330 motion control card and LabVIEW software. The tube in the Z θ scanner is rotated in steps of 1.0 deg. along the theta direction. The rotation of tube along the theta direction is carried out for every 1.0 mm movement of the probe along Z direction over 15.0 mm length. Figure 3.3 shows the photograph of the setup used for EC imaging of tubes.

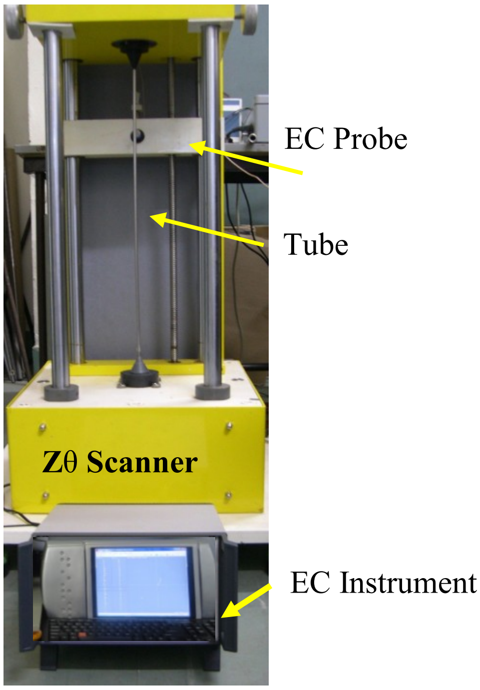

Figure 3.3 Photograph of the setup used for EC imaging of tubes.

3.1.4 Data acquisition system

The EC signals are acquired using a 12 bit analog-digital converter (ADC) card having sampling frequency of 1 kHz. During data acquisition, 1000 data points are acquired as the probe is kept stationary at every 1.0mm, and its average value is taken as the acquired data for that probe position. The measured resistive and reactive component signals are digitized and magnitude of the voltage (refer Section 1.2.3) is used for formatting images.

3.2 Details of specimens

3.2.1 Material

The specimens made of AISI type 316 SS (18.0% Cr, 8.0%Ni, 2.0%Mo, 2.0%Mn, 0.75% Si, 0.1%N, 0.08%C and Bal., Fe) are considered in this study.

3.2.2 Geometry

The large structures of critical components have planar and welded parts. Fuel clads and heat exchanger tubes are also found in nuclear industry. EC signals are influenced by variations in lift-off, material properties (electrical conductivity and magnetic permeability) in welded part in planar geometry and variation in geometry (wall thickness variations) in thin tubular component. Hence, geometries of 1) plate 2) weld region of plate (tungsten inert gas welding) and 3) thin tube are considered for imaging. The details of the specimens are given Table 3.1. The probe excitation frequency is determined based on the thickness of the part and using equation 1.9.

Table 3.1 Details of dimension of specimens used.

Geometry	Dimension, mm Length x Width x Thickness	Absolute surface Probe Diameter, mm	Frequency, kHz
Plate	150.0 x 150.0 x 5.0	3.0, 5.0, 20.0	150, 75, 20
Weld plate	350.0 x 150.0 x 5.0	3.0, 5.0	150
Tube	outer diameter:5.1 inner diameter 4.36 wall thickness: 0.37	3.0	350

3.3 Dimensional details of machined Flaws

Notches of different lengths (6.0 mm, 4.0 mm), widths (0.5 mm, 0.3 mm) and depths (0.5 mm, 1.0 mm, 2.0 mm) have been fabricated by electro discharge machining (EDM) process in 5.0 mm thick AISI type 316 SS plates and welds. The dimensions of the notches machined in plates, weld region of plates, and thin wall tubes are listed in Table 3.2, 3.3 and 3.4 respectively. The tolerance in the machining of notches is ± 0.05 mm.

Table 3.2 Dimensions of machined notches in SS 316 plates.

Plate No.	Flaw No.	Flaw Dimension (Length x Width x Depth), mm
B1	F1	4.0x 0.5 x 0.3
	F2	4.0x 0.5 x 0.5
	F3	6.0x 0.5 x 0.7
	F4	6.0x 0.5 x 1.0
B2	F5	20.0 x 0.5 x0.7
	F6	4.0x 0.5 x 0.7
B3	F7	4.0x 0.3 x 0.5
	F8	4.0x 0.3 x 1.0
	F9	6.0x 0.5 x 0.7
	F10	6.0x 0.5 x 1.0
B4	F11	4.0 x 0.3x 0.3
	F12	4.0 x 0.3x 0.5
	F13	6.0 x 0.3x 0.7
	F14	6.0 x 0.3x 1.5
	F15	8.0 x 0.3x 1.0
	F16	8.0 x 0.3x 2.0
	F17	8.0 x 0.5x 0.5
	F18	8.0 x 0.5x 1.0
	F19	8.0 x 0.5x 2.0
B5	F20	6.0 x 0.3x 1.0
	F21	6.0 x 0.3x 2.0
	F22	6.0 x 0.3x 3.0
	F23	6.0 x 0.3x 3.5
	F24	6.0 x 0.3x 4.0
	F25	6.0 x 0.3x 4.5

Table 3.3 Dimensions of machined notches in weld region of SS weld plates.

Weld Plate No.	Flaw No.	Flaw Dimension, mm Length (L) x Width (W) x Depth (D)	Type of Flaw
W1	F26	4.0 x 0.25 x 0.2	Longitudinal notch
	F27	4.0 x 0.25 x 0.3	
	F28	4.0 x 0.25 x 0.5	
	F29	6.0 x 0.25 x 0.5	
	F30	6.0 x 0.25 x 1.0	
W2	F31	6.0 x 0.25 x 0.5	Longitudinal notch
	F32	6.0 x 0.25 x 2.0	
	F33	8.0 x 0.25 x 0.3	Transverse notch
	F34	8.0 x 0.25 x 0.5	
	F35	8.0 x 0.25 x 0.6	

Table 3.4 Dimensions of machined notches in SS 316 tubes.

Tube No.	Flaw No.	Flaw Dimension, mm Length (L) x Width (W) x Depth (D)	Type of Flaw
T1	F36	4.0x 0.1x 0.075	Longitudinal notch
	F37	4.0x 0.1x 0.075	
T2	F38	4.0x 0.1x 0.075	
	F39	4.0x 0.1x 0.075	Transverse notch
	F40	4.0 x 0.1 x 0.15	

The notches having length 4.0 mm, width 0.5 mm and depth 0.5 mm (10% wall thickness) have been considered as shallow flaws among the machined flaws. The detection and enhancement of shallow flaws have been particularly considered for assessing the noise reduction capability of the processing approaches. The photographs of the specimens (plate, weld region and thin tube) having machined flaws are shown in Figure 3.4.

(a) Plate

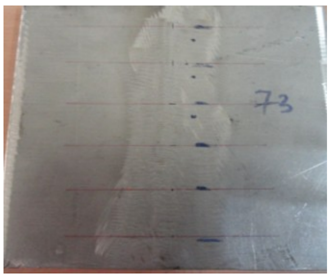

(b) Weld region

(c) Tube

Figure 3.4 Photographs of the specimens in which machined flaws have been introduced by EDM process.

3.4 Feritscope

In AISI type 316 stainless steel, magnetic delta ferrite in the welded region in the range of 5-7% is acceptable as it reduces micro fissuring and hot cracking susceptibility [64]. The presence of delta ferrite introduces variations in magnetic permeability. The delta ferrite content in welds is determined using Feritscope FMP30 (M/s. Fischer Technology), a hand-held device that works on the magnetic inductive principle and is shown in Figure 3.5. For the magnetic permeability measurement, magnetic field is induced on a material through magnetic field coupling using coil and the resulting field strength is measured to estimate the ratio of magnetic induction to magnetic field strength. The delta ferrite content is obtained with an accuracy of 0.1%.

Figure 3.5 The photograph of Feritscope used for measurement of delta ferrite.

In order to obtain the comparable measurements, calibration of the Feritscope has been carried out using the standard specimens having varying ferrite content in the range of 2.54% to 34.2 %. After completing the calibration procedure, the Feritscope probe has been placed on the weld surface and delta ferrite measurements were carried out in a raster manner at a step size of 2.0 mm starting from one end of the specimen to the other end, as depicted in Figure 3.6. The profile of the permeability variation is shown in Figure 3.6.

The delta ferrite in the base metal was found to be 0.4%, and in the weld region was found to be 4%. It is also observed that for the delta ferrite % decreases with distance from the weld centerline.

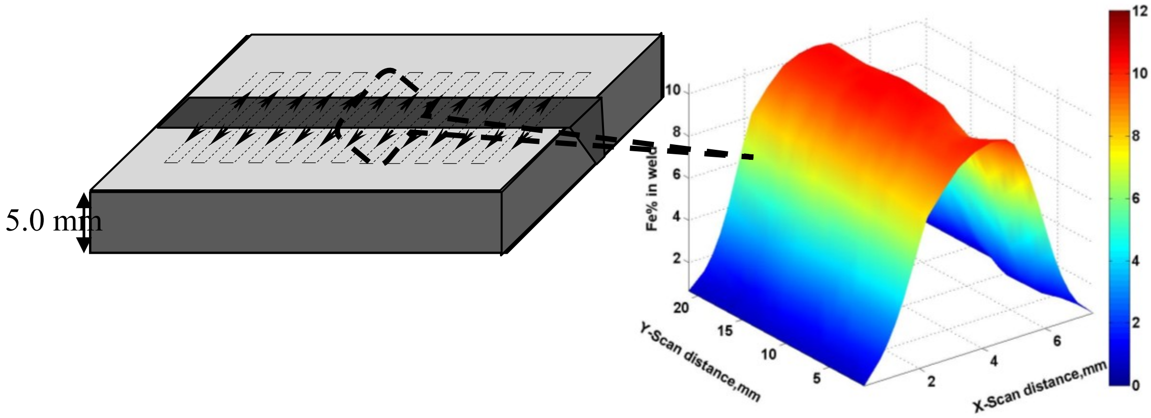

(a) (b)

Figure 3.6 (a) Schematic of raster scan of weld region and (b) the corresponding delta ferrite measured using Feritscope.

3.5 Generation of EC images

EC imaging of the test specimens is carried out by scanning the ECT probe over EDM notches machined. EC images of notches under variations in lift-off, material properties and geometrical variations are acquired. The EC images are processed using the proposed approaches for noise removal.

3.5.1 EC imaging of plates

Figure 3.7 (a) shows the raster scanning of an EC probe over the plate B1 having four flaws F1 to F4 (listed in Table 3.2). Typical EC image acquired with a constant lift-off of 0.5 mm from plate B1 is shown in Figure 3.7 (b). To simulate the variation in lift-off situation encounter during remote inspection of curved surfaces and weld region of components, random lift-off variation (< 1.5 mm) is specifically introduced during scanning by the movement of flexible probe holder. Figure 3.7 (c) shows the EC image acquired from the same notches with random lift-off variations (0.0 mm to 1.5 mm), simulating the situation encountered during remote inspection of curved surfaces and weld regions of components. Figure 3.7 (c) shows clearly the influence of flaw detection where small amplitudes from two shallow flaws (F1 and F2) are masked by noise due to variations in lift-off.

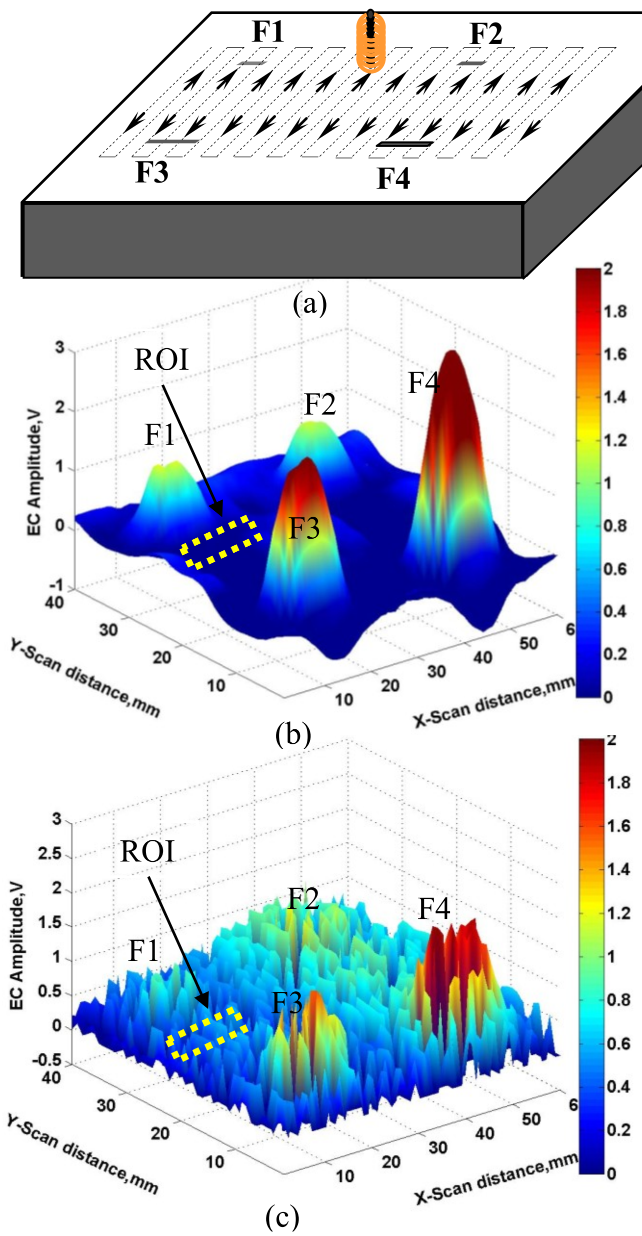

Figure 3.7 (a) Raster scan on a SS plate, EC images of flaws (F1-F4, in Table 3.2), acquired (b) at constant lift-off of 0.5 mm and (c) variations in lift-off (0.0 mm to 1.5 mm).

In order to assess the noise removal capability of the proposed approaches, a new parameter called the noise reduction percentage (NRP), has been proposed.

The NRP is calculated as

$$NRP = \left(\frac{N_I - N_P}{N_I}\right) * 100 \qquad 3.1$$

where N_I is the rms of noise in ROI in the input image before processing and N_P is the rms of noise in ROI in the image after processing. For NRP estimation, region between two flaws is considered as the region of interest (ROI) of noise as shown in Figure 3.7 (b) and (c). These ROIs from the identical region are used for estimating *rms* of noise in the input image as well as in the processed image. The higher the NRP, better the noise reduction capability.

Apart from noise reduction, the quality of flaw information is assessed on the basis of Signal to Noise Ratio (SNR) which is defined as logarithmic ratio of the mean value of the flaw signal (μ_{signal}) to the standard deviation of the noise (σ_{noise}) [14].

$$SNR = 20\,log\,\frac{\mu_{flaw\ ROI}}{\sigma_{noise\ ROI}} \qquad 3.2$$

The retention ability of flaw information is being assessed on the basis of reduction in peak amplitude of flaw image. A new parameter called Flaw reduction percentage (FRP), has been proposed. The degradation in flaw amplitude is estimated in terms of FRP as

$$FRP = \left(\frac{F_c - F_d}{F_c}\right) * 100 \qquad 3.3$$

where F_c is the peak amplitude of flaw in the image obtained at constant lift-off (0.3 mm) and F_d is the peak amplitude of flaw in the output image processed through the proposed approaches, where the input images are obtained at variable lift-off. The smaller the FRP, the better the flaw retention ability and is desirable.

3.5.2 EC imaging of weld plates

Figure 3.8 (a) shows the raster scan of an EC probe over the weld region. Figure 3.8 (b) shows the EC images acquired from the base metal region having machined EDM notches of the same dimension in weld plate W2 (F33 and F34 listed in Table 3.3).

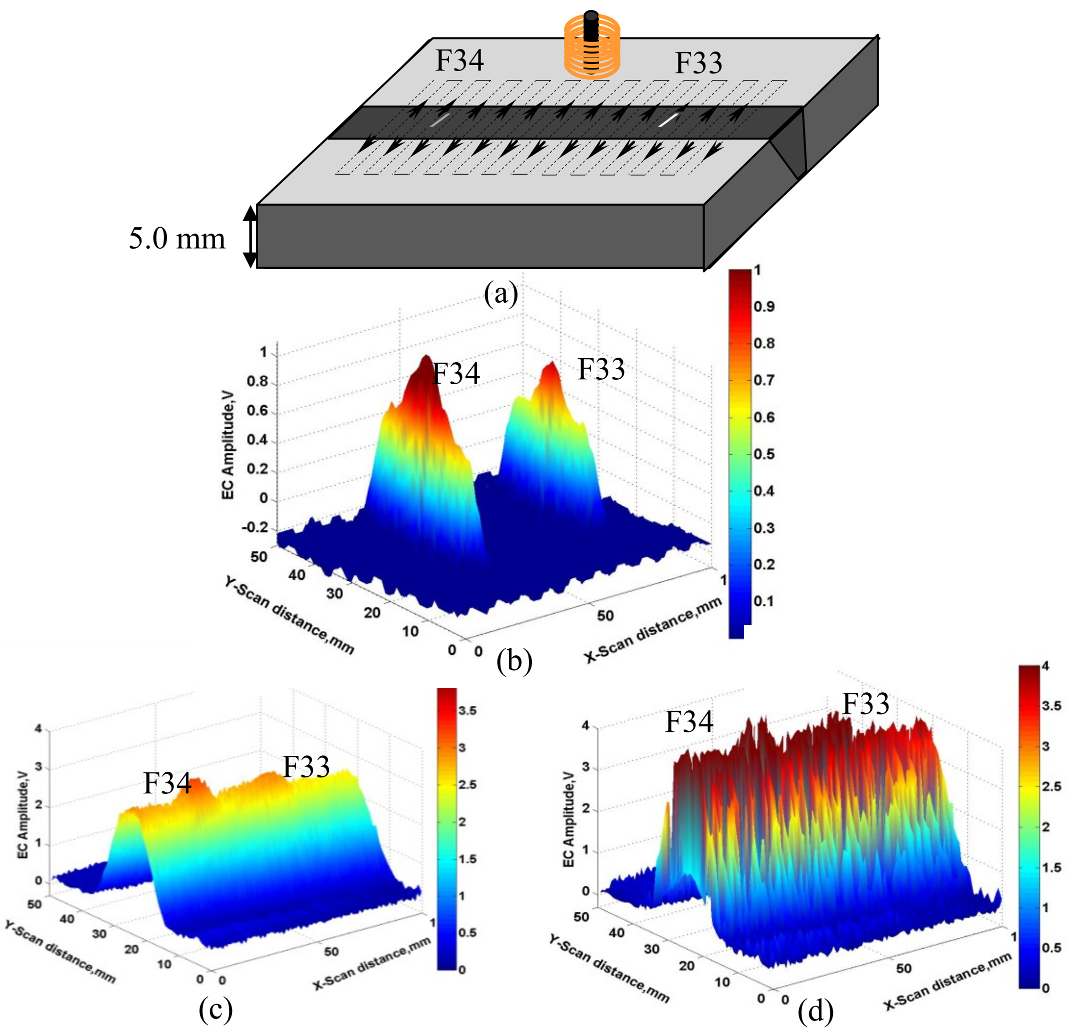

Figure 3.8 (a) Raster scan on a weld plate, EC images of flaws (F33 and F34 in Table 3.3) in (b) base metal region (c) weld region (lift-off 0.5 mm) and (d) variations in lift-off (0.0 mm to 1.5 mm).

Figure 3.8 (c) shows the typical EC image of the two flaws (F33 and F34) in weld plate W2 acquired at constant lift-off (0.5 mm). During imaging, large amplitude signal is observed across the weld region as compared to the base metal region (Figure 3.8 a). This is attributed to the noise due to material properties variations (refer Section1.3.2).In order to assess the electromagnetic characteristics across the weld region, the percentage of delta ferrite has been measured using Feritscope (refer Section 3.4). Further, added influence due to lift-off variations is shown in Figure 3.8 (d). From Figure 3.8, it is evident that the flaws are buried in the composite noise, necessitating the need for noise reduction for reliable detection of flaws in the base metal as well as in the weld region.

3.6 Summary

An EC imaging setup comprising of EC instrument, probe, scanning system, and data acquisition system has been established. A separate scanning system has been developed for imaging of SS plates and SS tubes. The notches of varying depths have been machined by EDM process in the base metal region and weld region of plates and thin walled clad tubes made of AISI type 316 stainless steel. EC images with a) variations in lift-off, b) variations in material properties and c) composite noise (variations in material properties and lift-off) have been acquired and two new parameters viz NRP and FRP have been proposed, for the first time, to assess the noise reduction and flaw retention capabilities of the proposed approaches.

Chapter 4 : Discrete wavelet transform based approach for automated noise removal

Preamble

This chapter proposes optimisation of wavelet filter, decomposition level and thresholding in DWT based approach for automated noise removal. The chapter presents criteria for optimisation of wavelet filter, decomposition level and selective elimination of noise through the implementation of semi-local paradigm for wavelet thresholding method. The denoising capability of the DWT based approach has been studied using experimental EC images of flaws in SS plates and welds. The performance of the DWT based approach has been analysed using the metrics NRP, SNR, FRP and flaw amplitude, in the presence of variations in lift-off.

4.1 Proposed DWT based approach

As discussed in Section 1.4.3, multiresolution capability of wavelet filters is utilised to analyse the localisation of space-frequency information in EC images. For effective noise removal as well as flaw separation in EC images, selection of an optimum wavelet filter among the 47 wavelet filters is required. The selection involves reconstruction of wavelet coefficients at different decomposition level for every wavelet filter for every image. This process requires a large number of trials and this makes the wavelet filter selection cumbersome. This limitation necessitates reducing large numbers of reconstruction trials by evolving optimisation criteria that can rank the wavelet filters. In view of this, maximum energy characteristic of the wavelet coefficients has been selected as a criterion for optimisation of wavelet filter (refer Section1.4.3.2). For optimisation of decomposition level, minimum entropy criterion has been selected.

Generally, denoising methods estimate a thresholding for the whole image. This may not be flexible to handle realistic test situations, where the existence and nature of desired signals are not known. This situation exists in EC images, especially where the flaw information is embedded within noise. The thresholding methods inadvertently remove the flaw information along with noise. Hence, an alternative approach for flexible sub-band level thresholding, a semi-local paradigm is proposed, for the first time, for EC images. The flow chart of the proposed DWT based approach for optimisation of wavelet filter, decomposition level, and thresholding for effective noise removal is shown in Figure 4.1.

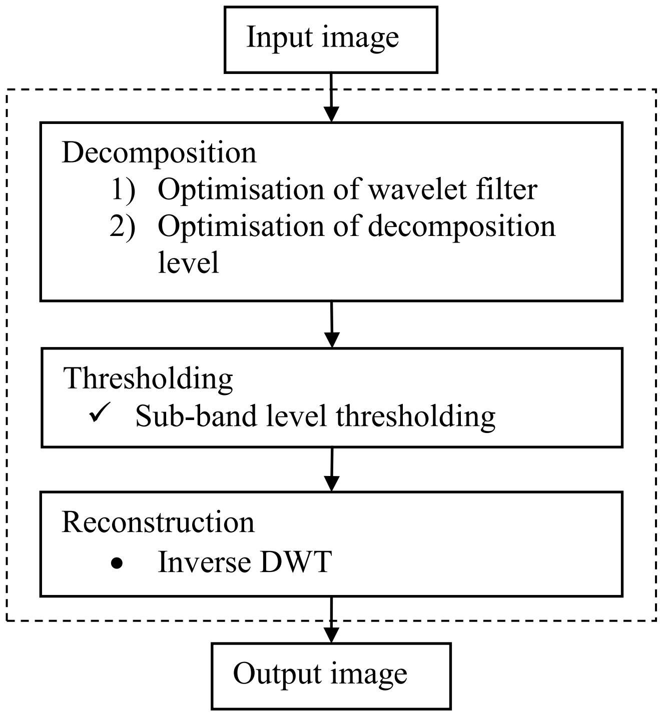

Figure 4.1 Flow chart of the proposed DWT based approach.

4.1.1 Optimisation of wavelet filter

The criterion 'maximum energy' of wavelet coefficients is chosen to assess the performance of the wavelet filters at the decomposition stage. The maximum energy among the wavelet filters is considered based on the following characteristics of optimum wavelet filter (refer Section 1.4.3.2):

a) maximum correlation with a particular frequency
b) extraction of higher magnitudes of coefficients at a particular decomposition level (scale)
c) coefficients with negligible magnitude at other levels

In order to study, the characteristic of wavelet coefficients at each decomposition level (scale), the decomposition of EC image is carried out. Typical 2D DWT on an EC image of a flaw (F29) in a weld plate using Bior6.8 wavelet and wavelet coefficients at each sub-band level (finer scale - HL(N)) and coarser scale-LL(N)) are shown in Figure 4.2. It is observed that coarser scale coefficients (sub-bands LL1 to LL3) retain information related to both flaw and material properties variations. The LL4 sub-band level extracts the information related to material properties variations (noise). The finer scale coefficients at HL(4) and HL(5) sub-band levels, extract information related to flaw. Since the study focuses only on removal of noise, the coarser scale coefficients (LL(N)) are not considered. Hence, the finer scale coefficients HL(N) (refer Section 1.4.3.2), that extracting information related to flaw have been considered for DWT processing. The maximum extraction of flaw information in the HL(4) and HL(5) sub-band levels is attributed to the maximum correlation of scaling functions g(4) and g(5) (refer Section 1.4.3) with flaw component. Hence, maximum energy of wavelet coefficients is considered as a criterion for optimisation of wavelet filter.

The maximum energy of wavelet coefficients can happen in two ways:

(a) one or more number of sub-band levels have coefficients with higher magnitude (i.e., wide spectrum) or

(b) a few sub-band levels have coefficients with higher magnitude (i.e., narrow spectrum) and other levels have negligible magnitude

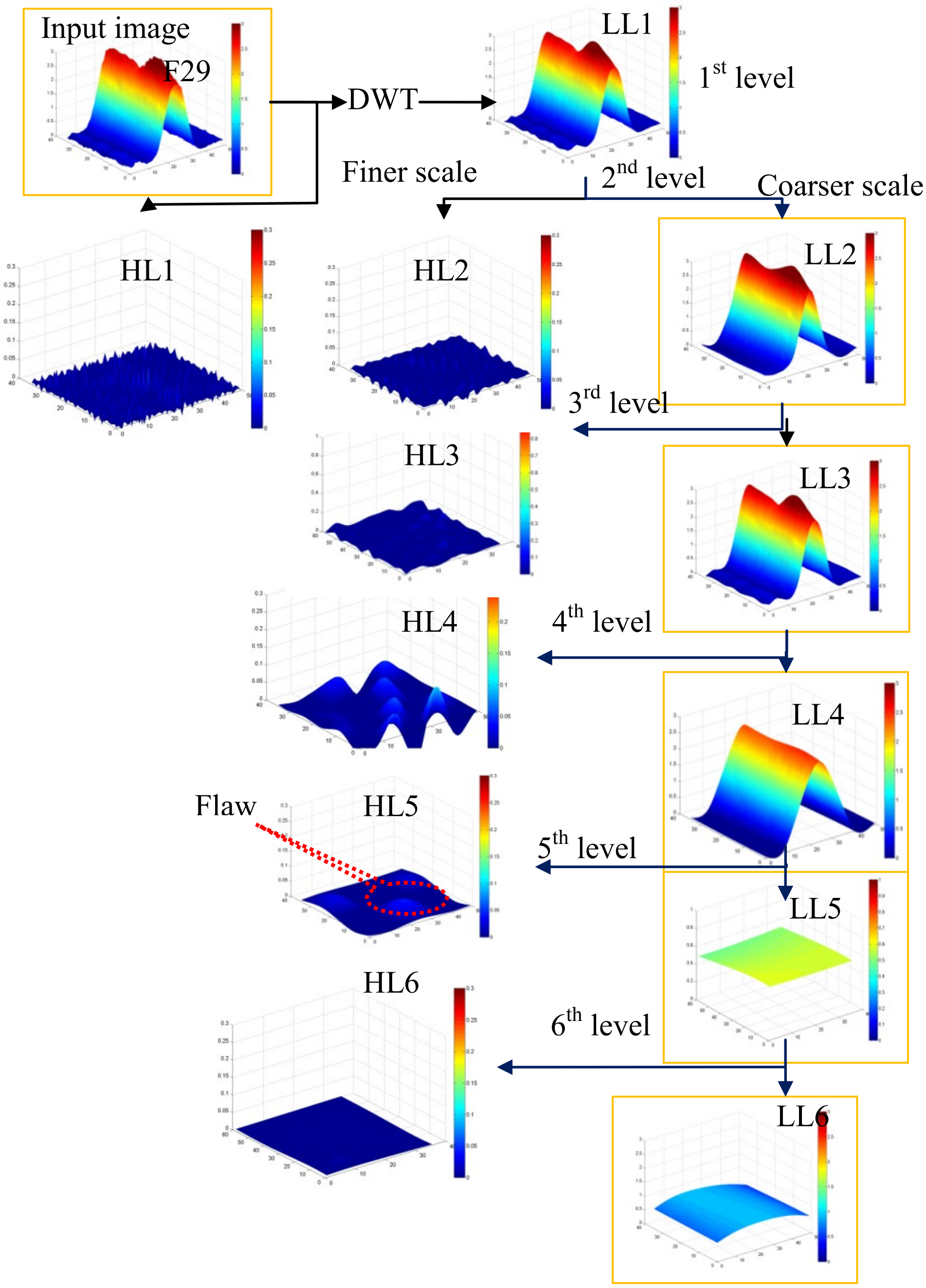

Figure 4.2 Wavelet coefficients at various sub-band levels.

The maximum energy of wavelet coefficients is due to the maximum correlation at a particular level. This represents a narrow filtering when the flaw information concentrate on a particular level reduces multilevel dependency, and is desirable. Based on this, an energy criterion has been optimised as ($0.9*E_{max} \le E \le E_{max}$), for selecting a set of wavelet filters that extract energy within 90% of E_{max}. The flow chart of the optimisation of wavelet filter is shown in Figure 4.3. This optimisation of wavelet filter has the following three steps:

a) Decomposition of EC image using 47 wavelet filters up to HL(6) sub-band level
b) Estimation of energy of wavelet coefficients for all wavelet filters at each sub-band level
c) Ranking the wavelet filters with maximum energy using the energy criterion ($0.9*E_{max} \le E \le E_{max}$), selected as an optimum wavelet filter

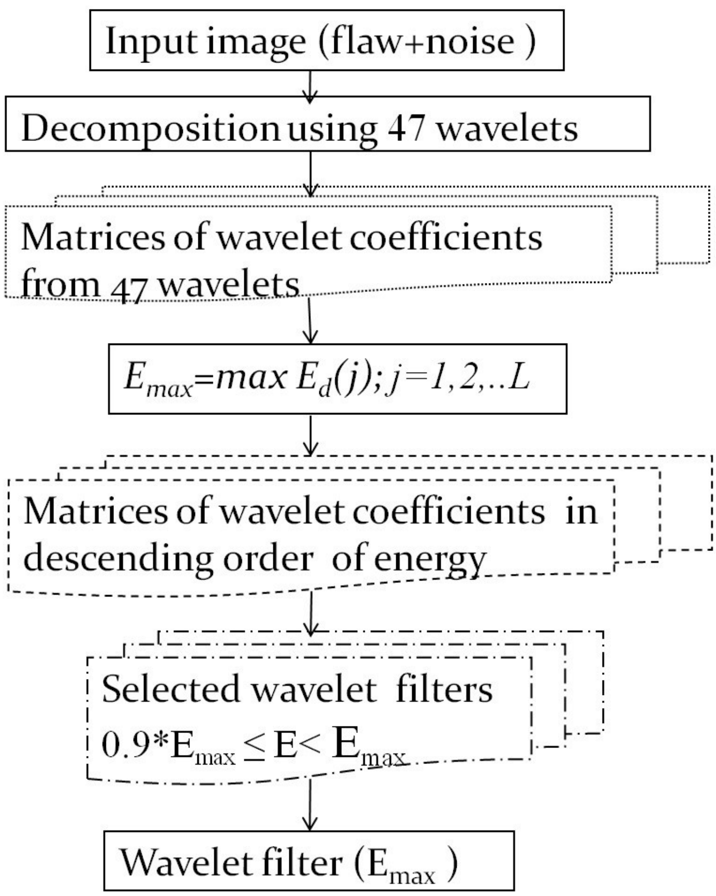

Figure 4.3 Flow chart of the optimisation of wavelet filter.

4.1.2 Optimisation of decomposition level

Although, DWT decorrelates the information well, it is found that strong intra-scale and inter-scale dependencies between wavelet coefficients exist. It is clear from Figure 4.2, the wavelet coefficients related to flaw are extracted at a few sub-band levels. It represents inter-scale dependency of flaw information and indicates the flaw has range of frequency components. Hence, the wavelet filter that extracts flaw information within a few sub-band level, known as localization of spectral components (refer Section 1.4.3.2) is preferred. The performance of denoising would be significantly improved if such dependencies could efficiently be exploited.

In view of this, to assess the inter-scale dependency between the wavelet coefficients, the minimum distribution difference (minimum entropy) among the decomposition levels is considered. To estimate the minimum entropy, criterion called *weighted risk factor* is incorporated.

The optimisation of decomposition level involves the following three steps:

i. Estimation of entropy for selected wavelet filters at every decomposition level
ii. Estimation of minimum entropy among decomposition levels using proposed criterion called *weighted risk factor*
iii. Ranking the decomposition levels having coefficients with minimum entropy, selected as an optimum decomposition level.

The flow chart of the optimisation of decomposition level is shown in Figure 4.4. A criterion named, weighted risk factor, has been proposed, for the first time, to select an appropriate wavelet filter having minimum entropy among the inter-scale wavelet coefficients.

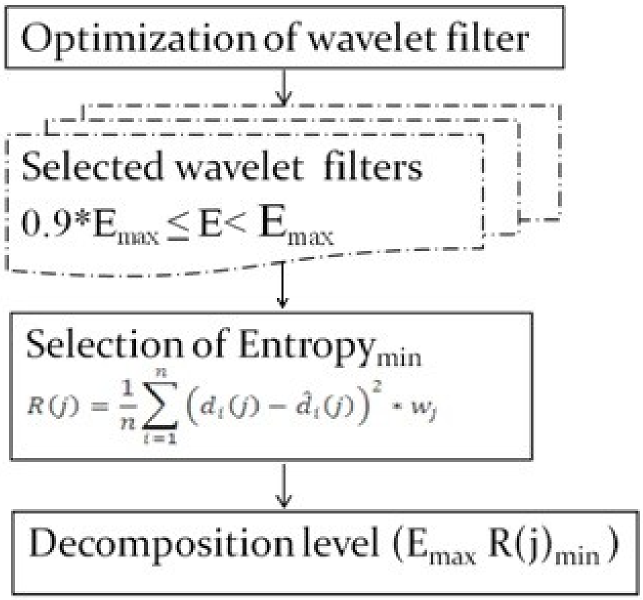

Figure 4.4 Flow chart of the optimisation of decomposition level.

It is formulated based on the feature that if the energy distribution of inter sub-band level wavelet coefficients is sufficiently close, (better frequency localization) then the difference between the coefficients have a minimum mean square error (i.e., minimum risk, minimum entropy). Let, the image is decomposed to N levels and the finer scale HL(j) is strongly correlated with level HL(j+1). The correlation in the subsequent levels j+2,J+3,…L decreases, then it represents the better localization of spectral content, at each level wavelet filters, as observed in Figure 4.2. However, subsequent sub band level HL(6) shows negligible magnitude of the coefficients and it is found that the coefficients correspond to flaw decay rapidly along the finer scales, hence wavelet coefficients up to HL6) sub-band level have been considered for entropy estimation.

The proposed weighted risk factor is described as

$$R(j) = \frac{1}{n}\sum_{i=1}^{n}\left(d_i(j) - \hat{d}_i(j)\right)^2 * w_j \qquad 4.1$$

where $w_j = L - j + 1$, i is the wavelet, j sub-band level, L is the user-defined wavelet multiresolution level of decomposition

$d_i(j)$ coefficient of the raw image at sub-band level (HL(j))

$\hat{d}_i(j)$ coefficient (hard threshold) at sub-band level (HL(j))

n number of wavelet coefficients at each sub-band level

w_j is the assigned weight, calculated according to j and L values

The weighted risk factor estimates the expected value of the mean squared error associated at each decomposition level. This favours the decomposition level (the corresponding wavelet filter) that estimates the lowest error. Thus, it implicitly incorporates estimation of minimum entropy among the wavelet coefficients in the decomposition levels. The weighted risk factor estimates the difference between the coefficients at adjacent scales j and $j+1$.

4.1.3 Optimisation of thresholding

As the conventional thresholding methods inadvertently remove the flaw information along with the noise, a semi local paradigm for wavelet thresholding is proposed. This involves the division of an image into blocks, which are then individually denoised. An appropriate threshold limit is estimated for coefficients at each sub-band level, allows more flexible denoising. To denoise the blocks, classical thresholding methods viz., Sqtwolog Rigrsure and Heursure (refer Section 1.4.3.3) are used to choose the thresholding limit. This allows some parts of the images to be denoised more selectively than others, providing a flexibility of eliminating noise and preserving desired localized coefficients. The rationale of operating on the small blocks than whole block at each sub-band level is as follows:

- ✓ First, the individual denoising of small block is analogous to local regression, in which all the information in a neighbourhood is used to obtain a fitted value at a particular location. This helps to have the denoised versions of adjacent small blocks are in complete overlapping with each other.
- ✓ Second, any edge effects during denoising of large blocks will not be manifested due to the overlapping between blocks.

Figure 4.5 shows the flow chart of the semi local paradigm proposed for wavelet thresholding at the sub-band level coefficients.

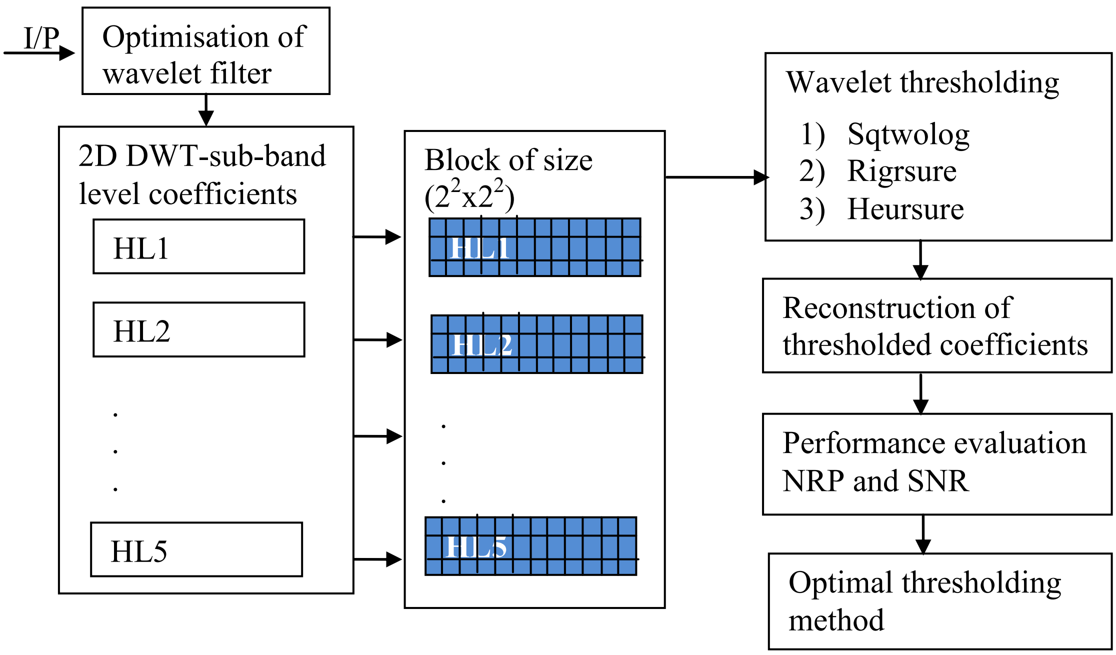

Figure 4.5 Flow chart of the semi local paradigm proposed for wavelet thresholding.

The sequence of thresholding is as follows:

1) The sub-band level wavelet coefficients from DWT using an optimum wavelet filter up to the appropriate decomposition level, are divided into a small non overlapping blocks of size (2^2x2^2).

2) If the dimensions of the sub-band level coefficients are not multiples of 2^n, sub-band level coefficients are augmented (with zero padding) to have the dimensions of multiples of 2^n.
3) The threshold value for each block is estimated using classical thresholding methods viz., Sqtwolog, Rigrsure and Heursure (refer Section 1.4.3.3)
4) The centers of the denoised blocks are extracted and reassembled, yielding a denoised version of the wavelet coefficients at sub-band levels, HL(N).
5) After denoising, by the level based thresholding on each block, the wavelet coefficients are reconstructed to get denoised images.

Each block in each sub-band level HL(N) is subjected to thresholding, that directly takes into account of the local characteristics of the image at each sub-band level.

4.1.4 Reconstruction of wavelet coefficients

Each block of denoised wavelet coefficients are reconstructed by a reverse process of synthesis filtering, and this is implemented as inverse DWT (refer Section 1.4.3.4).

4.2 Experimental studies on EC images

The number of EC images with a single source of noise (due to variations in lift-off) and composite noise (due to variations in lift-off and material properties) are processed for evaluating the proposed optimisation of wavelet filter, decomposition level and thresholding.

4.2.1 Optimisation of wavelet filter for images with noise

The optimisation of wavelet filter for EC images having a) noise due to variations in lift-off (single source) and b) composite noise have been studied.

4.2.1.1 Images with noise from single source: Variations in lift-off

For an input EC image of a flaw (F1, length 4.0 mm, width 0.5 mm, depth 0.3 mm) acquired with variations in lift-off (0.0 mm to 1.0 mm), estimated energy of wavelet filter is estimated and is tabulated in Table 4.1. Among the wavelet filters, Db5 that estimates maximum energy of 72.3, is selected as the optimal wavelet filter.

Table 4.1 Estimated energy for various wavelet filters.

Wavelet filter	Energy
Bior1.1	44.8
Bior1.3	52.3
Bior2.4	54.7
Bior2.6	56.8
Bior4.4	54.5
Bior3.5	61.4
Bior6.8	***67.0***
Coif1	60.0
Coif2	52.0
Coif3	55.0
Coif5	***65.0***
Db2	45.8
Db4	47.8
Db5	**72.3**
Db8	***69.0***
Db10	51.7
Db20	61.5
Sym2	55.0
Sym3	52.0
Sym4	42.5
Sym6	45.1
Sym8	48.7

The performance of the optimisation of wavelet filter is evaluated on EC image of a flaw (F1, length 4.0 mm, width 0.5 mm, depth 0.3 mm) in a plate (B1) acquired with variations in lift-off (0.0 mm to 1.5 mm). To compare the performance of wavelet filter Db5,with wavelet filters that extract energy within 90% of the E_{max} (Table 4.1)) is considered and the results are shown in Figure 4.6. The NRP and SNR have been determined. It is observed that NRP of 90% is achieved by Db5 as compared to the processed images from other three wavelet filters (Bior6.8, coif5, Db8, selected using the energy criteria).

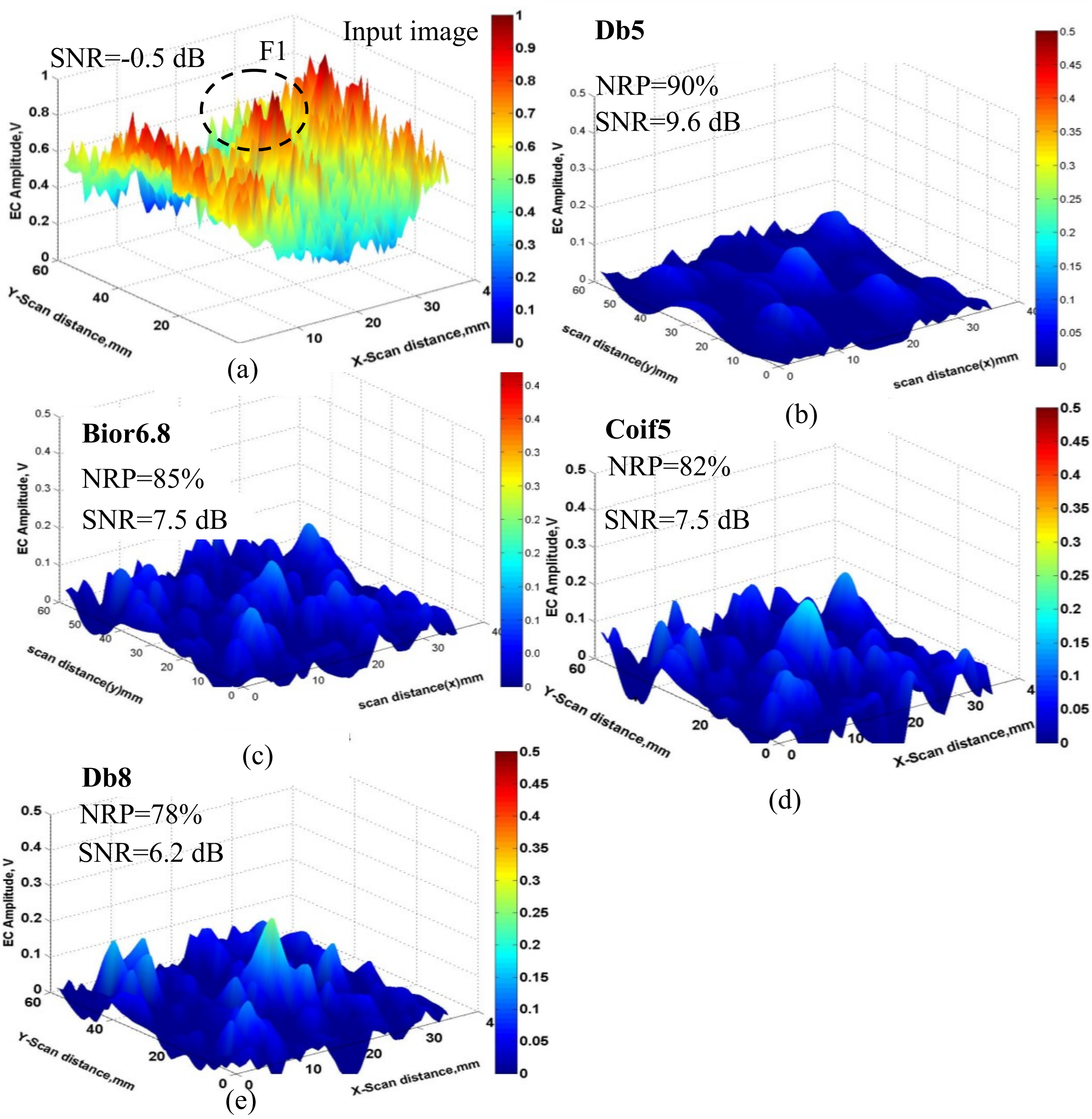

Figure 4.6 EC image of (a) a flaw (F1) acquired with variations in lift-off (0.0 mm to 1.0 mm) and (b-e) the DWT processed images using Db5, Bior6.8, coif5, Db8 wavelet filters.

From Figure 4.6, no uniformity in noise removal as well as separation of flaw is found among these wavelet filters. They differ in their flaw retention capability in the presence of noise. However, the optimal wavelet filter, Db5 shows better performance. The optimal wavelet filters for a number of EC images having flaws as well as noise are identified by the proposed DWT based approach. Table 4.2 tabulates the optimal wavelet for the EC images and the estimated NRP of the processed image. Studies reveal that Db5 is the optimal wavelet for images from plates with single source of noise.

Table 4.2 Optimisation of wavelet filter for EC images with a single source of noise.

Image	Plate No.	Flaw No.	Noise	Optimal wavelet filter, level	NRP, %
1	B1	F1	Lift-off	Db5, Level5	90
2	B2	F6	-do-	-do-	90
3	B3	F9, F10	-do-	-do-	92
4	B4	F14, F15	-do-	-do-	92
5	B5	F21	-do-	-do-	92

4.2.1.2 Images with composite noise: Variations in lift-off and material properties

Table 4.3 lists the estimated the energy of wavelet coefficients for the EC image of a flaw (F29, length 6.0 mm, width 0.25 mm, depth 0.5 mm) in a weld plate (Figure 4.2). It is observed from the Table 4.3 that Bior6.8 wavelet filter that estimates maximum energy of 68.8 among the wavelet filters is selected as the optimal wavelet filter.

The optimal wavelet filters for number of EC images having flaws as well as composite noise are identified by the proposed approach. Table 4.4 tabulates the optimal wavelet filter for the EC images with composite noise and estimated NRP of the processed image. Studies reveal that Bior6.8 is the optimal wavelet for images from weld plates with composite noise.

Table 4.3 Estimated energy for various wavelet filters.

Wavelet filter	Energy
Bior1.1	53.4
Bior1.3	61.4
Bior2.4	54.4
Bior2.6	58.7
Bior 4.4	52.3
Bior5.5	54.5
Bior6.8	68.8
Coif1	46.1
Coif2	46.1
Coif3	54.8
Coif5	63.6
Db2	49.1
Db4	56.1
Db5	67.0
Db8	65.0
Db10	45.1
Db20	60.1
Sym2	50.1
Sym3	44.5
Sym4	50.1
Sym6	38.4
Sym8	46.5

Table 4.4 Optimisation of wavelet filter for EC images with composite noise.

Image	Plate No.	Flaw No.	Noise	Optimal wavelet filter, level	NRP, %
1	W1	F28	Composite noise	Bior6.8, Level5	80
2	W1	F29	-do-	-do-	82
3	W2	F31	-do-	-do-	80
4	W2	F35	-do-	-do-	85

4.2.2 Optimisation of decomposition level for images with noise

Table 4.5 lists the estimated the entropy of wavelet coefficients at each sub-band level of the EC image of a flaw (F1, length 4.0 mm, width 0.5 mm, depth 0.3 mm) in a plate B1

(Figure 4.2). Among the selected wavelet filters, Db5 at decomposition level 5 (HL(5)) that estimates minimum entropy of 1.3 is selected as the optimum decomposition level.

Table 4.5 Estimated entropy for an EC image with noise from a single source.

Wavelet filter	Energy ($0.9^*E_{max} \leq E \leq E_{max}$)	Entropy					
		Decomposition level					
		1	2	3	4	5	6
Bior6.8	67.0	3.2	3.2	2.5	2.1	2.0	2.6
Coif5	65.0	3.0	2.8	2.7	3.4	3.6	3.8
Db5	72.3	2.5	2.7	2.4	1.7	1.3	1.8
Db8	66.2	3.3	3.0	2.6	2.4	2.2	2.0

The optimisation of decomposition level for images with composite noise has also been studied. Table 4.6 lists the estimated the entropy of wavelet coefficients at each sub-band level of the EC image of a flaw (F29, length 6.0 mm, width 0.25 mm, depth 0.5 mm) in a weld plate (Figure 4.2). It is observed from the Table 4.6 that wavelet filter Bior6.8 at decomposition level 5 that results in the minimum entropy, is selected as the optimum decomposition level.

Table 4.6 Estimated entropy for an EC image with composite noise.

Wavelet filter	Energy ($0.9^*E_{max} \leq E \leq E_{max}$)	Entropy					
		Decomposition level					
		1	2	3	4	5	6
Bior6.8	68.8	3.6	3.8	3.4	3.0	2.3	2.8
Db5	67.0	4.5	4.0	3.8	4.2	3.0	3.8
Db8	65.0	3.5	3.8	4.2	4.8	3.5	4.2
Coif5	63.6	4.4	3.6	4.8	4.6	3.8	5.3

From the entropy estimation, wavelet filter Db5, level 5 is found to be optimum for EC images with noise due to variations in lift-off. For an EC image of composite noise, wavelet filter Bior6.8, level 5 is found to be optimum wavelet filter with minimal entropy of 2.3 among the selected wavelet filters.

4.2.2.1 Denoising performance of optimal wavelet filter and decomposition level

The efficacy of the automated selection of optimal wavelet filter, decomposition level in the proposed DWT based approach has been evaluated in terms of NRP and SNR. Figure 4.7 shows the noise removal capability of the optimal wavelet filter Db5 selected for EC images having flaw and noise from a single source. A NRP of 92% is observed in the processed image by the wavelet filter Db5, level 5 and this indicates the effectiveness of the wavelet filter selection.

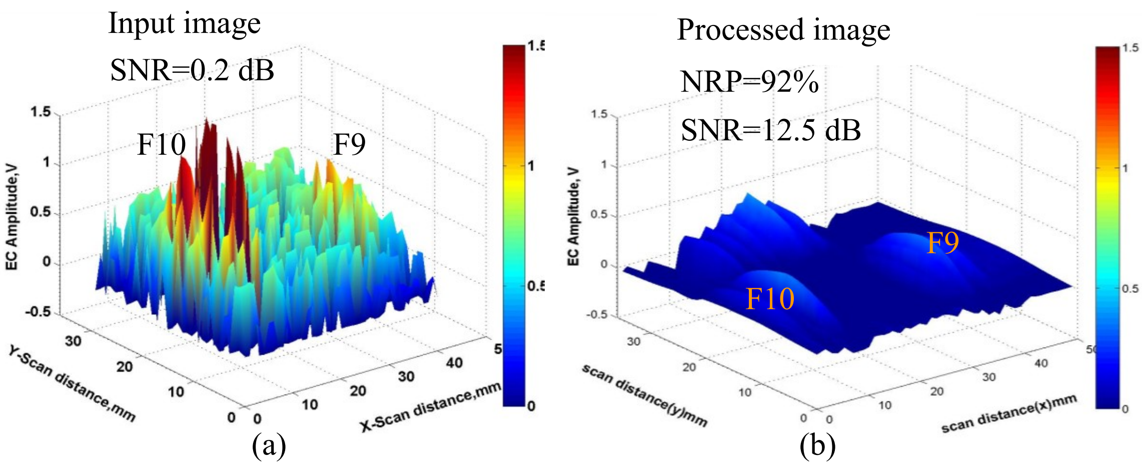

Figure 4.7 EC image of (a) two flaws (F9, F10) in a plate (B3), (b) processed image from DWT based approach using wavelet filter Db5, level 5.

EC image of a weld plate (W1) having a buried flaw (F26, length 4.0 mm, width 0.25 mm, depth 0.2 mm) in composite noise is shown in Figure 4.8 (a). The processed image using the wavelet filter Bior6.8, level 5 is shown in Figure 4.8 (b). A NRP of 80% is observed in the processed image by the wavelet filter Bior6.8, level 5, and this indicates the effectiveness of the wavelet filter selection in the case of composite noise.

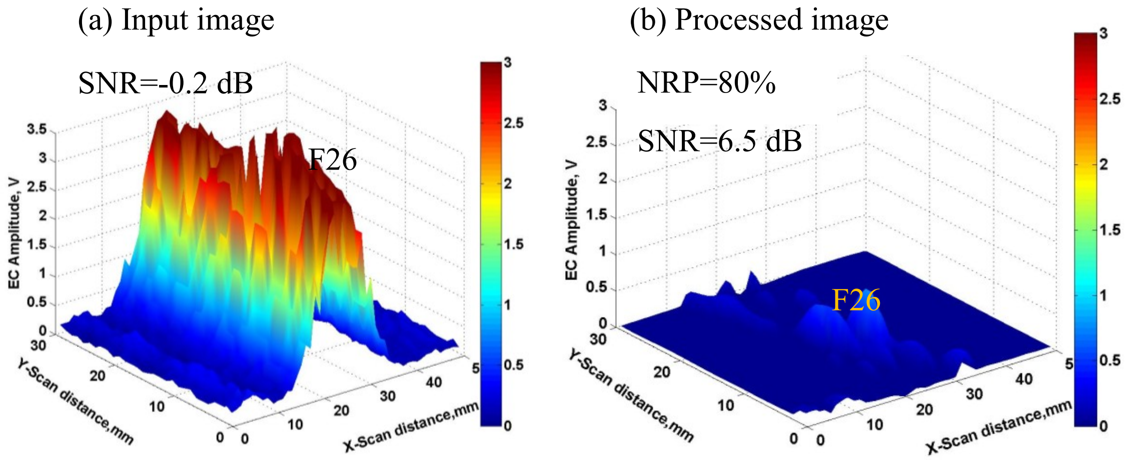

Figure 4.8 EC image of (a) a flaw (F26) in a weld plate (W1) and (b) processed image from DWT based approach using wavelet filter Bior6.8, level 5.

It has been observed, for the first time that for plates wavelet Db5-level 5 and for weld plates wavelet Bior6.8-level 5 are found optimum. For EC images of plates, similarity to the shape of flaw of Db5 wavelet filter yields better correlation. In the case of weld plates, orthogonality and similarity properties (refer Section 1.4.3.1) of Bior6.8 wavelet filter are attributed to the better removal of noise. The similarity yields a maximum correlation, while orthogonality of wavelet filter decomposes coefficients into non overlapping sub band frequency (refer Section 1.4.3.1), plays a role for removal of multiple sources of noise. This, in turn, reduces the inter-scale dependency and results in minimum entropy.

However, in the case of EC images with composite noise, the undulations present in the processed image pose ambiguity in flaw detection (false call). This necessitates further removal of noise. In view of this, selective elimination of noise by wavelet thresholding method is attempted and this is discussed in the next section.

4.2.3 Optimisation of thresholding for images with noise

The denoising performance of Heursure, Rigrsure and Sqtwolog thresholding methods has been assessed using NRP. The effective selection of appropriate coefficients by sub-band level dependent thresholding is evaluated on EC images of a weld plate (W1). Figure 4.9 (a) shows an EC image of a flaw (F26) in weld plate W1, buried in the composite noise. The DWT processed image using wavelet filter bior6.8, level 5 is subjected to sub-band level thresholding. The denoised image from Heursure, Rigrsure and Sqtwolog thresholding methods are shown in Figure 4.9 (b-d) respectively.

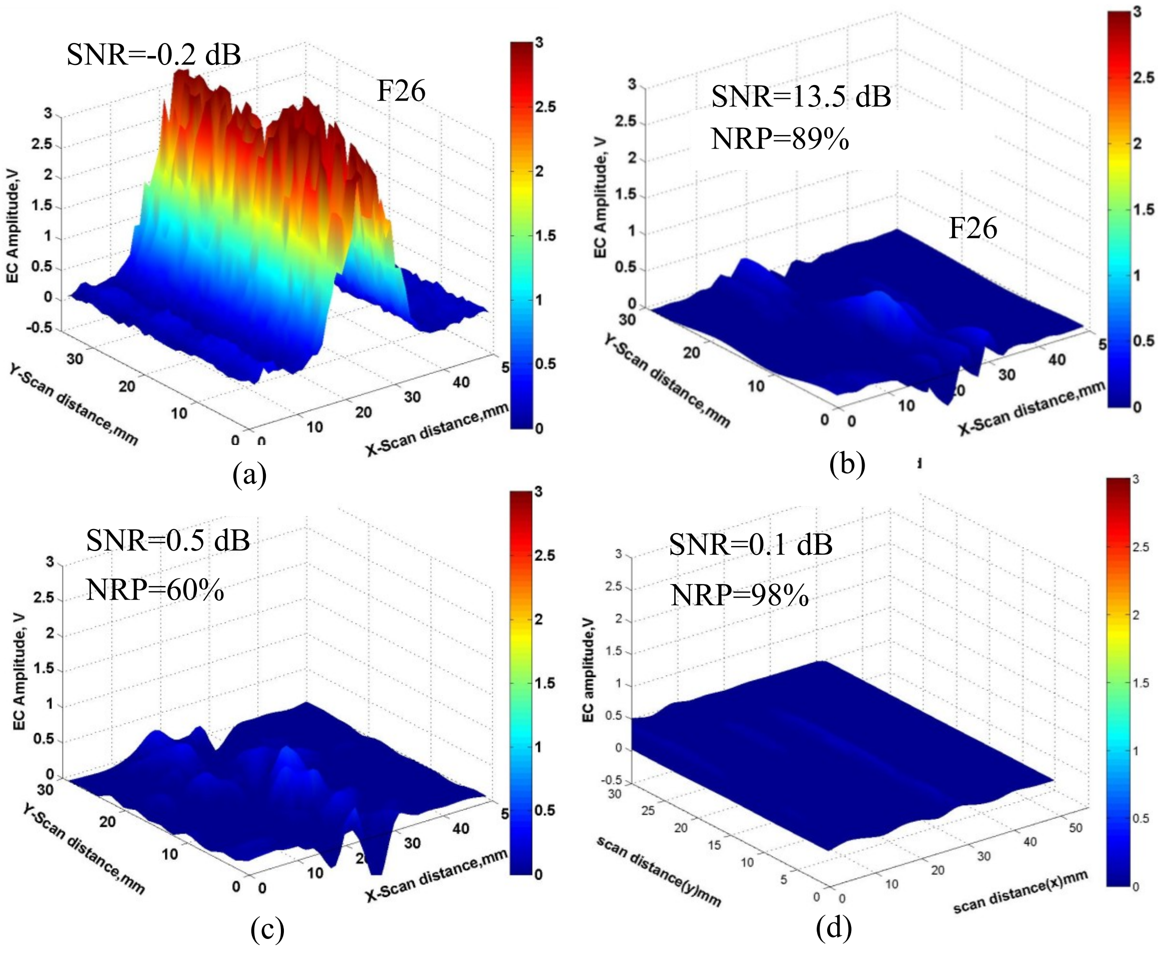

Figure 4.9 EC image of (a) a flaw (F26) in weld plate W1 buried in composite noise and thresholded image from (b) Heursure, (c) Rigrsure and (d) Sqtwolog thresholding.

Rigrsure achieves NRP of 60% and retains some of the composite noise components and introduces ambiguity in the identification of flaw region. This is due to the estimation of universal threshold limit based on Stein's Unbiased Risk Estimator. The Sqtwolog thresholding method, results in maximum a NRP of 98%, due to the hard thresholding, however it removes all the information due to large thresholding.

Among these methods, Heursure thresholding method achieves NRP of 89%. As seen in Figure 4.9 (b), denoised image from the Heursure thresholding method achieves SNR of 13.5 dB and FRP of 10%. It is noted that sub-band level thresholding, subsequent to DWT processing (shown in Figure 4.8(b)) improves NRP from 80% to 89% and removes all the undulation and results unambiguous detection of the flaw. This improvement confirms the requirement of selective elimination of sub-band level wavelet coefficient using Heursure thresholding method.

The denoising capability of the Heursure thresholding method is attributed to be due to the combined thresholding by Stein's unbiased likelihood estimation and Sqtwolog thresholding methods. This method allows two ways of estimation of threshold limit, depending on the data. In order to avoid any loss of desired information when data are over smoothed, SURE estimation is chosen while Sqtwolog is used when data are under smoothed condition. This allows denoising either more conservatively or more selectively based on the local characteristics of the image. Hence, Heursure thresholding method is adopted and incorporated into the proposed DWT based approach.

4.3 Performance evaluation of the proposed DWT based approach

The proposed DWT based approach has been evaluated for a number of EC images having i) a single source of noise and ii) composite noise.

4.3.1 Removal of noise from single source

The denoising ability of the DWT based approach has been evaluated on an EC image of a flaw-free region in a plate (B1) acquired with variations in lift-off (0.0 mm to 0.5 mm) and is shown in Figure 4.10 (a). The processed image using the wavelet filter Db5, Level 5 is shown in Figure 4.10 (b). Further denoised image from Heursure sub-band level thresholding is shown in Figure 4.10 (c). A NRP of 99% is observed.

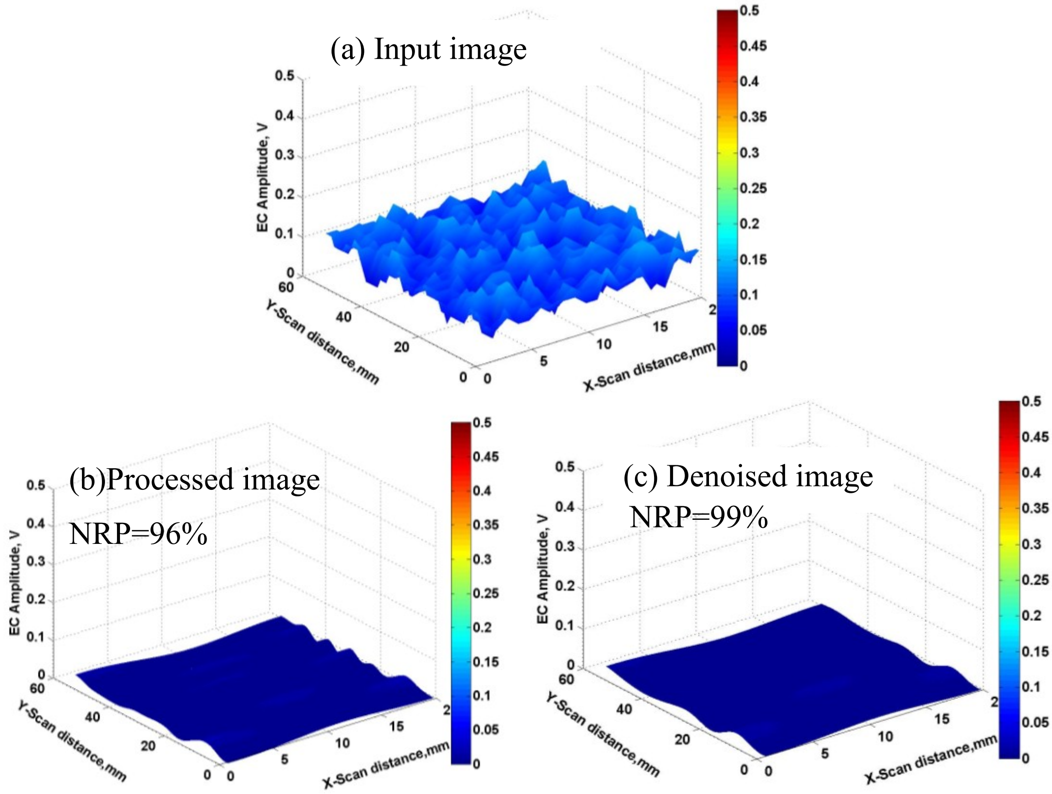

Figure 4.10 EC image of (a) flaw free region in a plate (B1) with variations in lift-off (b) processed from DWT using wavelet filter Db5, level 5 and c) denoised image from Heursure sub-band level thresholding.

Figure 4.11 (a) shows the EC image of two flaws (F9, F10, length 5.0 mm, width 0.5 mm, depths 0.7 mm, 1.0 mm) in a plate (B3). The processed image using the wavelet filter Db5, Level 5 is shown in Figure 4.11 (b) and the denoised image from Heursure sub-band level thresholding is shown in Figure 4.11 (c). A significant improvement in NRP of 95% and SNR of 14.5 dB are observed.

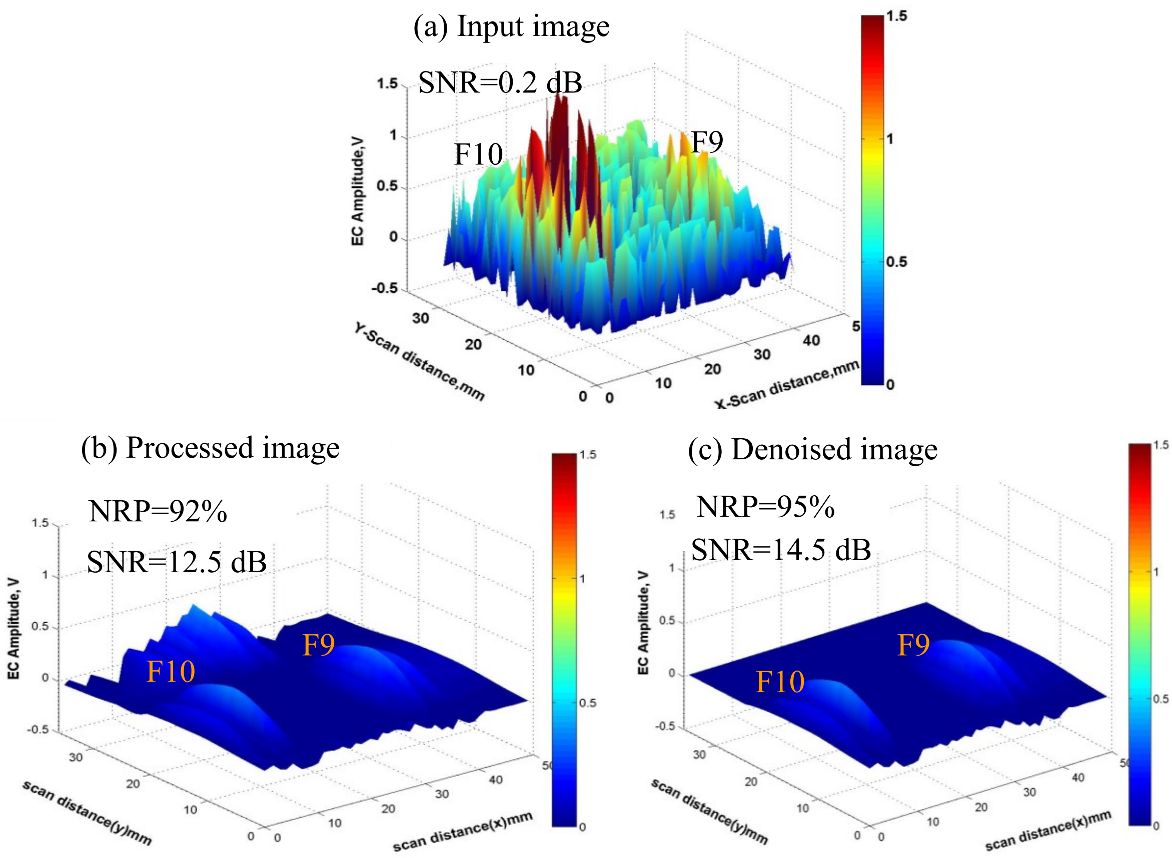

Figure 4.11 EC image of (a) two flaws (F9, F10) in a plate (B3), (b) processed from DWT based approach using wavelet filter Db5, level 5 and (c) denoised images from Heursure sub-band level thresholding.

The denoising ability of the DWT based approach has been evaluated on a single source of noise from weld plate (W1) acquired at constant lift-off of 0.3 mm and is shown in Figure 4.12 (a). The processed image using the wavelet filter Bior6.8, Level 5 is shown in Figure 4.12 (b) and the denoised image from Heursure sub-band level thresholding is shown in Figure 4.12 (c). A NRP 98% is observed.

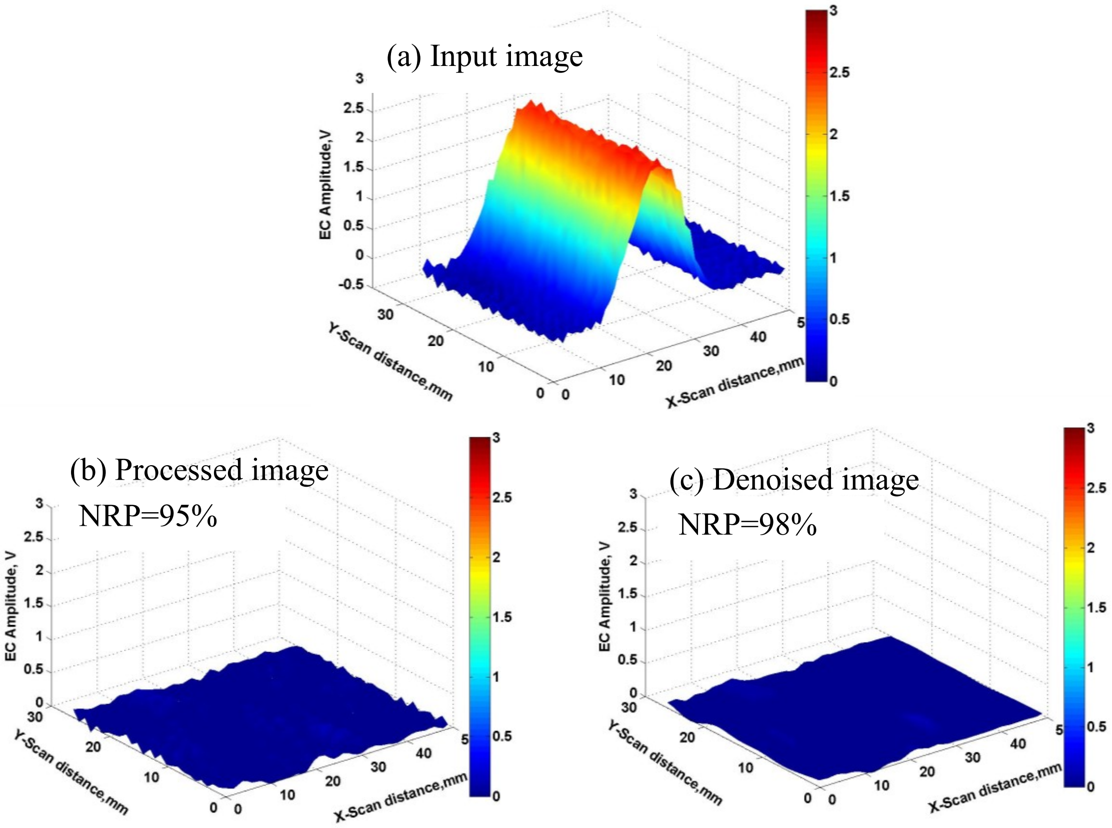

Figure 4.12 EC image of (a) flaw free region in a weld plate (W1) with variations in material properties, (b) processed image from DWT using wavelet filter Bior6.8, level 5 and (c) denoised image from Heursure sub-band level thresholding.

The DWT based approach has been evaluated on an EC image of a flaw (F26, length 4.0 mm, width 0.25 mm, depth 0.2 mm) in a weld plate (W1), with single source of noise from material properties variations and is shown in Figure 4.13 (a). The processed image using the wavelet filter Bior6.8, Level 5 is shown in Figure 4.13 (b) and the denoised image from Heursure sub-band level thresholding is shown in Figure 4.13 (c). A NRP of 97% and SNR of 14.5 dB are observed.

From these results, it is evident that the proposed DWT based approach ensures effective noise removal and improved flaw detection in EC images having noise from a single source.

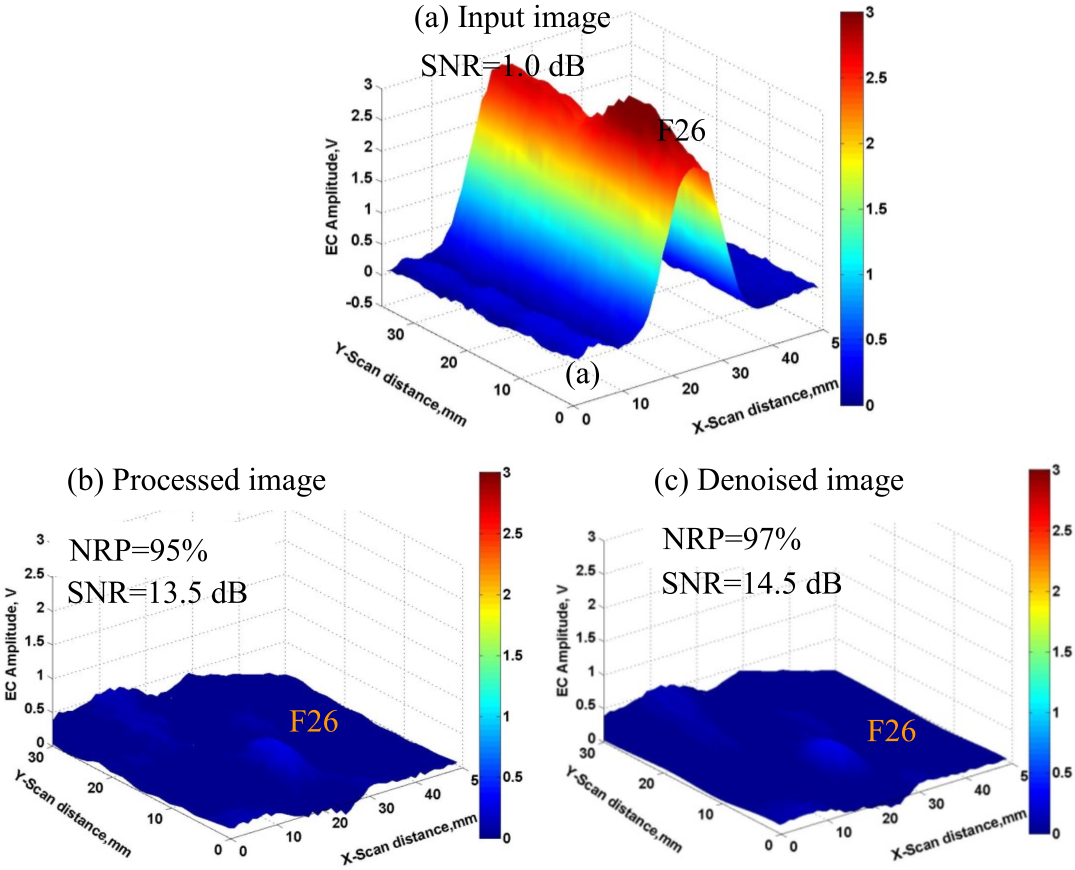

Figure 4.13 EC image of (a) a flaw (F26) in a weld plate (W1), with variations in material properties, (b) processed image from DWT using Bior6.8, level 5 and (c) denoised image from Heursure sub-band level thresholding.

4.3.2 Removal of composite noise

The proposed DWT based approach has been evaluated for removal of composite noise in EC images acquired in the weld region with variations in lift-off (0.0 mm to 1.0 mm). Figure 4.14 (a) shows the EC image of two flaws (F34, F35, length 8.0 mm, width 0.25 mm, depths 0.5 mm, 0.6 mm) with composite noise. The processed image using the wavelet filter Bior6.8, Level 5 is shown in Figure 4.14 (b) and the denoised image from Heursure sub-band level thresholding is shown in Figure 4.14 (c). A NRP of 90% and SNR of 13.0 dB are observed.

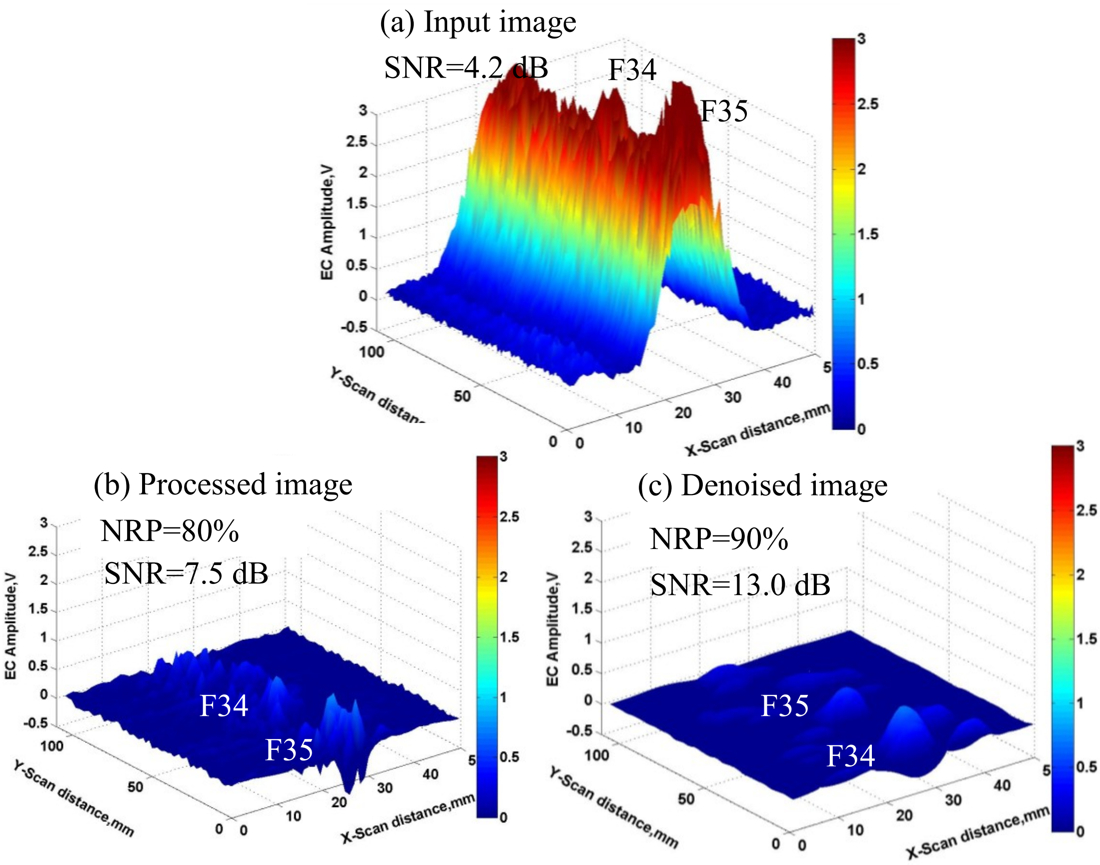

Figure 4.14 EC image of (a) two flaws (F33, F34) in a weld plate (W1) with composite noise, (b) processed image from DWT using wavelet filter Bior6.8, level 5 and (c) denoised image from Heursure sub-band level thresholding.

From these results, it is observed that the proposed DWT based approach promises effective removal of noise from single source as well as composite noise. Apart from noise reduction, retention ability of flaw information is being assessed on the basis of reduction in peak amplitude of flaw image. The degradation in flaw amplitude is estimated in terms of FRP. For estimation of FRP, the original amplitude flaw (F_c) is estimated from the EC images obtained at constant lift-off of 0.3 mm.

4.3.3 Flaw retention ability

The flaw retention ability of the proposed DWT based approach has been evaluated for several EC images of plates (B1, B2, B3, B4 and B5) and weld plates (W1 and W2) with variations in lift-off (0.0 mm to 1.0 mm). Table 4.7 and Table 4.8 list the estimated NRP, SNR, peak amplitude and FRP from the processed images.

Table 4.7 Performance evaluation of the DWT based approach for EC images with a single source of noise.

Plate No.	Flaw No.	Flaw Dimension (length x width x depth), mm	Input image SNR, dB	Denoised image NRP, %	SNR, dB	Flaw amplitude, V	FRP, %
B1	F1	4.0x 0.5 x 0.3	6.8	90	14.2	0.24	20
	F2	4.0x 0.5 x 0.5	7.2		13.5	0.42	15
	F3	6.0x 0.5 x 0.7	6.5	92	13.4	0.8	20
	F4	6.0x 0.5 x 1.0	8.5		13.9	1.2	14
B2	F5	20.0 x 0.5 0.7	6.2	90	12.9	0.8	16
	F6	4.0x 0.5 x 0.7	7.0	88	13.2	0.8	20
B3	F7	4.0x 0.3 x 0.5	6.2	88	14.5	0.42	15
	F8	4.0x 0.3 x 1.0	7.5		14.0	1.2	14
	F9	6.0x 0.5 x 0.7	7.0	93	14.5	0.72	12
	F10	6.0x 0.5 x 1.0	8.0		14.5	1.1	11
B4	F11	4.0 x 0.3x 0.3	4.5	90	14.5	0.20	26
	F12	4.0 x 0.3x 0.5	5.2		14.0	0.42	20
	F13	6.0 x 0.3x 0.7	6.2		13.2	0.82	18
	F14	6.0 x 0.3x 1.5	8.5	92	13.6	1.8	10
	F15	8.0 x 0.3x 1.0	7.5		13.5	1.2	14
	F16	8.0 x 0.3x 2.0	9.2		13.5	2.1	12
	F17	8.0 x 0.5x 0.5	5.5		11.3	0.4	15
	F18	8.0 x 0.5x 1.0	7.5	92	14.5	1.3	12
	F19	8.0 x 0.5x 2.0	9.2		14.0	2.2	7

Table 4.8 Performance evaluation of the DWT based approach for EC images with composite noise.

Weld Plate No.	Flaw No.	Flaw Dimension (length x width x depth), mm	Input image SNR, dB	Denoised image NRP, %	SNR, dB	Flaw amplitude, V	FRP, %
W1	F26	4.0 x 0.25 x 0.2	4.0	89	13.5	0.13	35
	F27	4.0 x 0.25 x 0.3	4.2	89	13.2	0.22	26
	F28	4.0 x 0.25 x 0.5	4.8	86	13.2	0.38	25
	F29	6.0 x 0.25 x 0.5	4.8	90	13.0	0.4	25
	F30	6.0 x 0.25 x 1.0	5.5	88	13.2	0.85	20
W2	F31	6.0 x 0.25 x 0.5	4.5	88	13.6	0.39	22
	F32	6.0 x 0.25 x 2.0	5.5	90	13.2	2.1	15
	F33	8.0 x 0.25 x 0.3	4.2	90	13.8	0.2	33
	F34	8.0 x 0.25 x 0.5	4.5	90	13.5	0.4	20
	F35	8.0 x 0.25 x 0.6	4.8	90	13.7	0.53	18

From the tables, the retention ability of the proposed DWT based approach in the presence of noise due to a single source and composite noise is analysed using FRP. The estimated FRP for flaws of various depths for the case of single source of noise and composite noise is shown in Figure 4.15 and Figure 4.16.

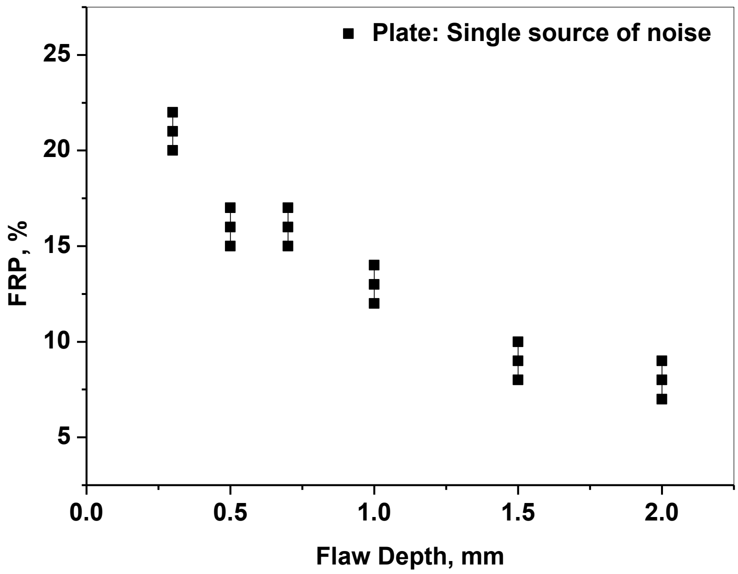

Figure 4.15 Estimated FRP for flaws of various depths in the denoised images.

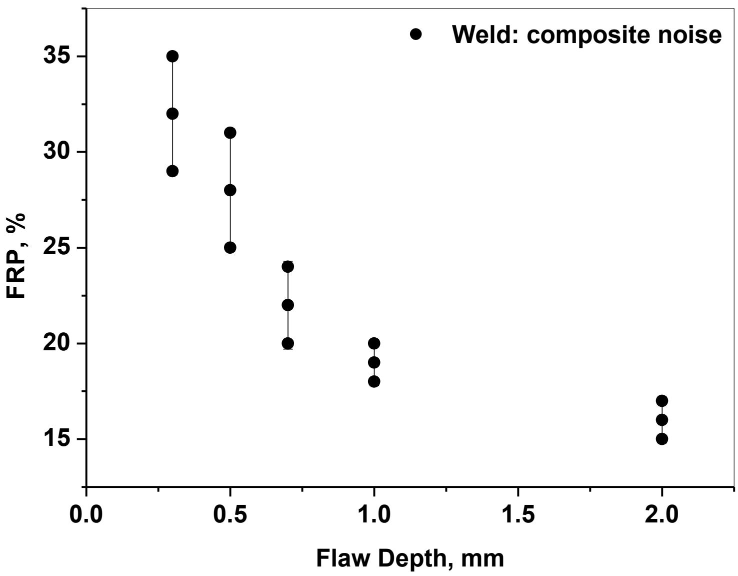

Figure 4.16 Estimated FRP for flaws of various depths in the denoised images.

Some reduction in the flaw amplitude is observed in the processed images. The FRP of ~26% is observed (flaw depth 0.5 mm) in the case of composite noise removal. This is higher as compared ~15% for the case of single source of noise. In general, FRP is less for higher flaw amplitude. The reduction in peak amplitude results in underestimation of severity of flaw, thus in turn affects the structural assessment of the component.

4.3.4 Influence of test parameters

In ECT, depending on the dimension and expected depth location of the flaw, various test frequencies and probes of different diameters are used. The variation in test frequency and *psf* of the probe change the field-flaw interaction resulting in variation in flaw information and noise. Hence, the influence of these parameters on noise reduction capability of the proposed DWT based approach has been studied.

Several EC images of plates (B1, B2, B3) and weld plates (W1, W2) are acquired using probes of 5.0 mm and 20.0 mm diameter at evaluation frequencies of 75 kHz and 20 kHz are processed using the proposed DWT based approach. It is observed that DWT based approach has selected same wavelet Db5, Level 5 for EC images of the plates and wavelet filter Bior6.8, Level 5 for EC images of the weld plates acquired at test frequencies of 20 kHz, 75 kHz and 150 kHz using probes of 3.0 mm, 5.0 mm and 20.0 mm diameter.

The denoising ability of the proposed approach for EC images acquired at 75 kHz using 5.0 mm diameter probe for SS plates and welds are shown in Figure 4.17 and Figure 4.18 respectively.

EC image of four flaws (F1, F2- length 4.0 mm, width 0.5 mm, depths 0.3 mm, 0.5 mm; F3, F4 - length 6.0 mm, width 0.5 mm, depths 0.7 mm, 1.0 mm) in a plate (B1) with variation in lift-off (0.0 mm to 1.0 mm) is shown in Figure 4.17 (a). The denoised image is shown in Figure 4.17 (b). The NRP of 92% and SNR of 13.9 dB are observed.

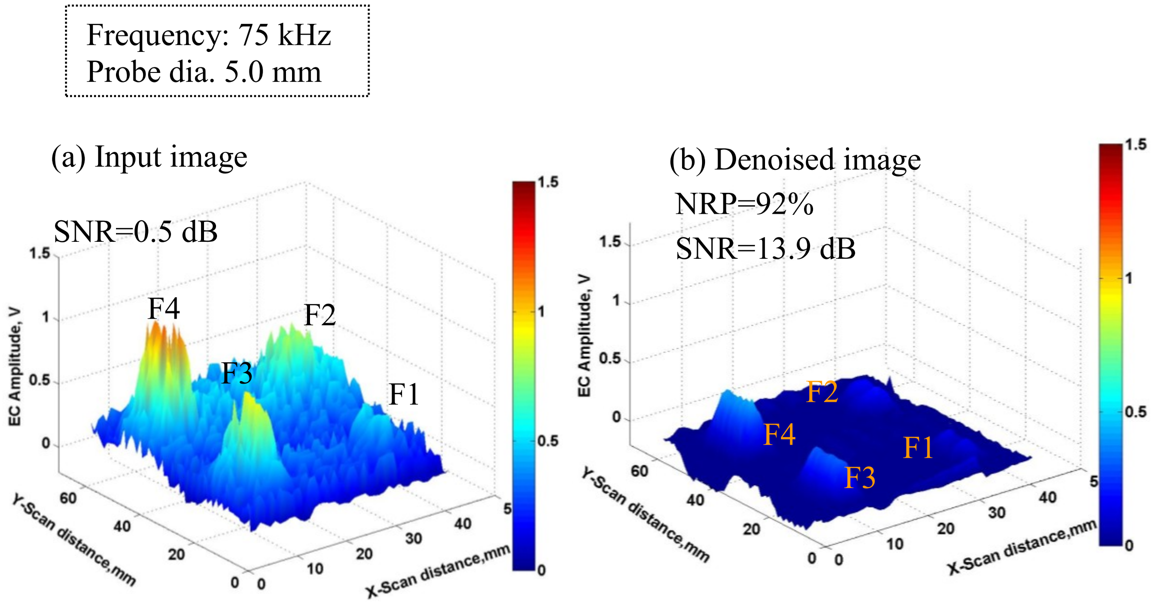

Figure 4.17 EC image of (a) four flaws (F1-F4) in a plate (B1) using 5.0 mm diameter probe (5 kHz), (b) denoised image from DWT based approach.

Figure 4.18 (a) shows the EC image of a flaw (F26, length 4.0 mm, width 0.25 mm, depths 0.2 mm) in a weld plate (W1) with variations in lift-off (0.0 mm to 1.0 mm). The denoised image is shown in Figure 4.18 (b). NRP of 89% and SNR of 13.5 dB are observed. From these results, it is observed that testing parameters viz. diameter of 3.0, 5.0, 20.0 mm and frequencies of 20 kHz, 75 kHz and 150 kHz do not have significant influence on the proposed DWT based approach.

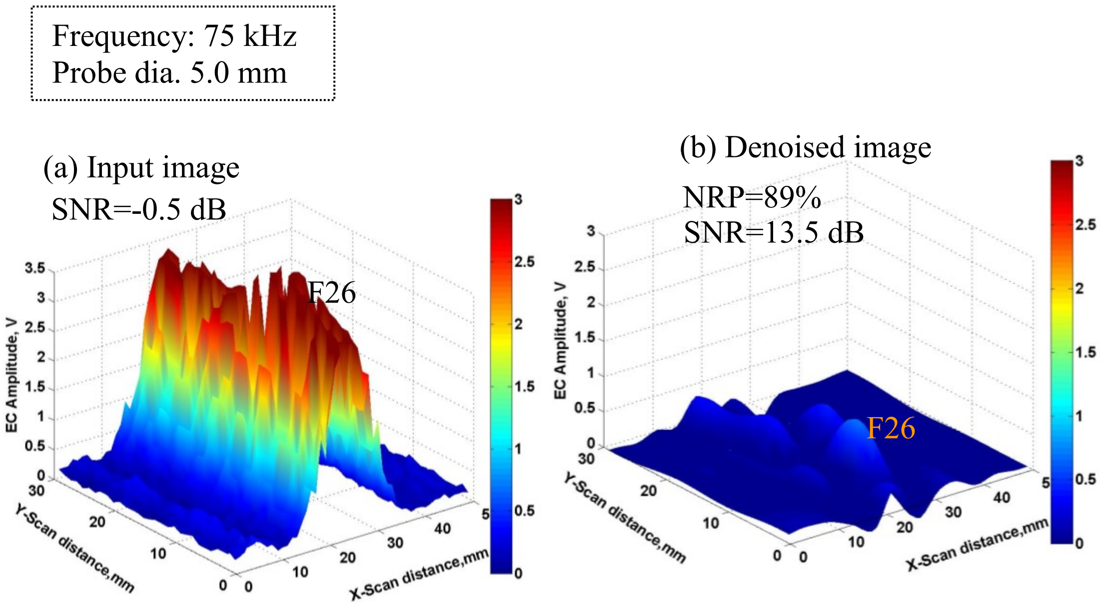

Figure 4.18 EC image of (a) a flaw (F26) in a weld plate (W1) using 5.0 mm diameter probe (5 kHz), (b) denoised image from DWT based approach.

4.3.5 Evaluation of noise tolerance

4.3.5.1 Noise from single source: Variations in lift-off

The variations in lift-off are mainly encountered during the remote EC inspection of curved surfaces. Surface condition is also a concern because EC signals from shallow flaws on the surface consist of lift-off noise. This reduces the sensitivity to shallow surface flaws. In view of this, noise tolerance of the proposed DWT based approach is evaluated for higher amount of noise from variations in lift-off (0.0 mm to 1.5 mm, 0.0 mm to 2.0 mm).

The input images of a flaw (F5, length 20.0 mm, width 0.5 mm, depth 0.7 mm) in plate B2 acquired with variations in lift-off are shown in the first column of Figure 4.19. The corresponding denoised images obtained from the proposed DWT based approach are shown in the second column of Figure 4.19.

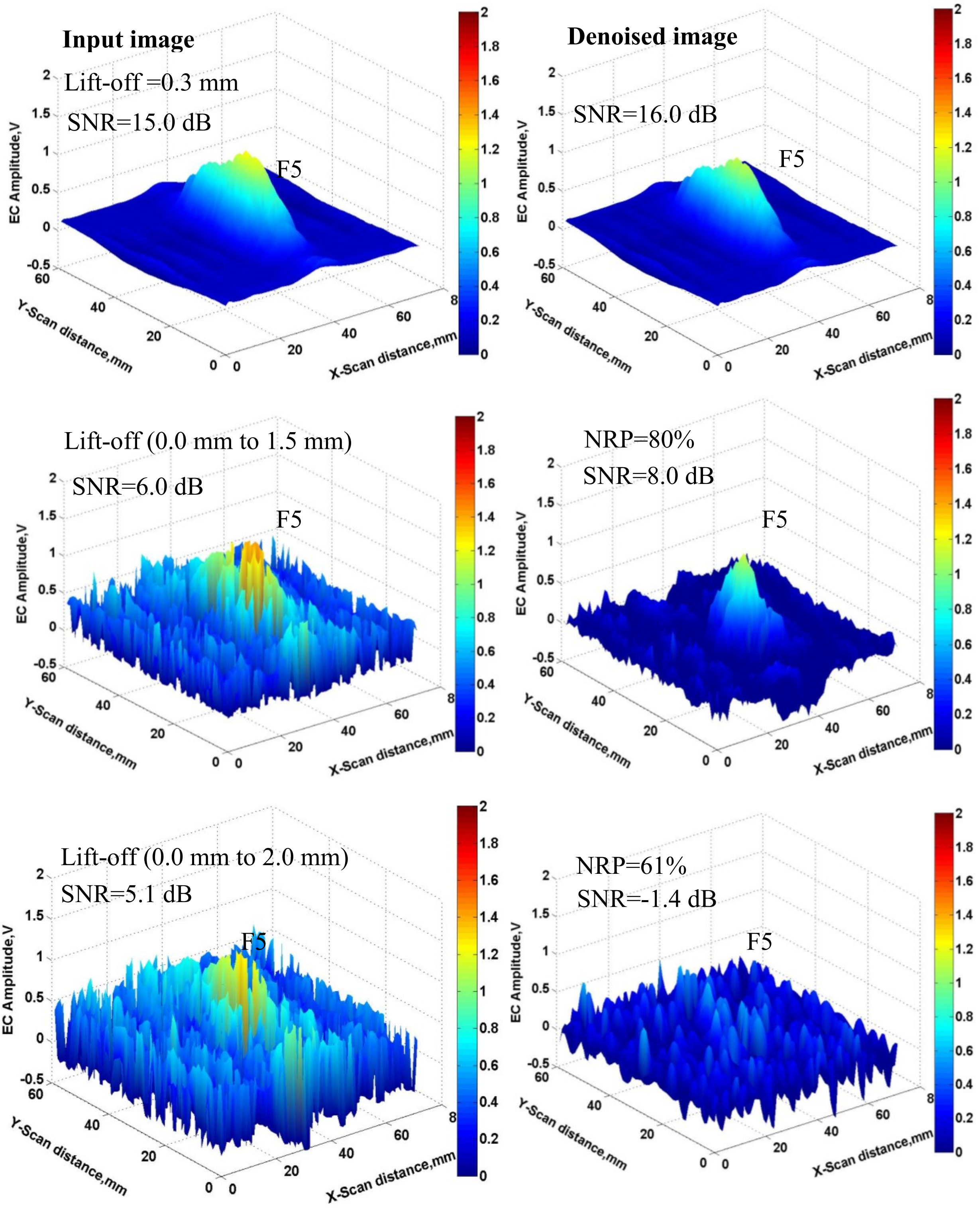

Figure 4.19 Performance of the DWT based approach for variations in lift-off.

It is observed that, NRP as well as SNR decrease with increase in variations in lift-off. The influence of the noise on flaw retention ability is estimated in terms of FRP and is shown in Figure 4.20. From Figure 4.20, FRP of 10% is observed for 0.0 mm to 1.0 mm variations in lift-off. However, at higher variations in lift-off (0.0 mm to 1.5 mm), FRP increases to 40% indicating the influence of noise on flaw retention ability of the DWT based approach. Table 4.9 lists the estimated NRP, SNR flaw amplitude and FRP from the processed images.

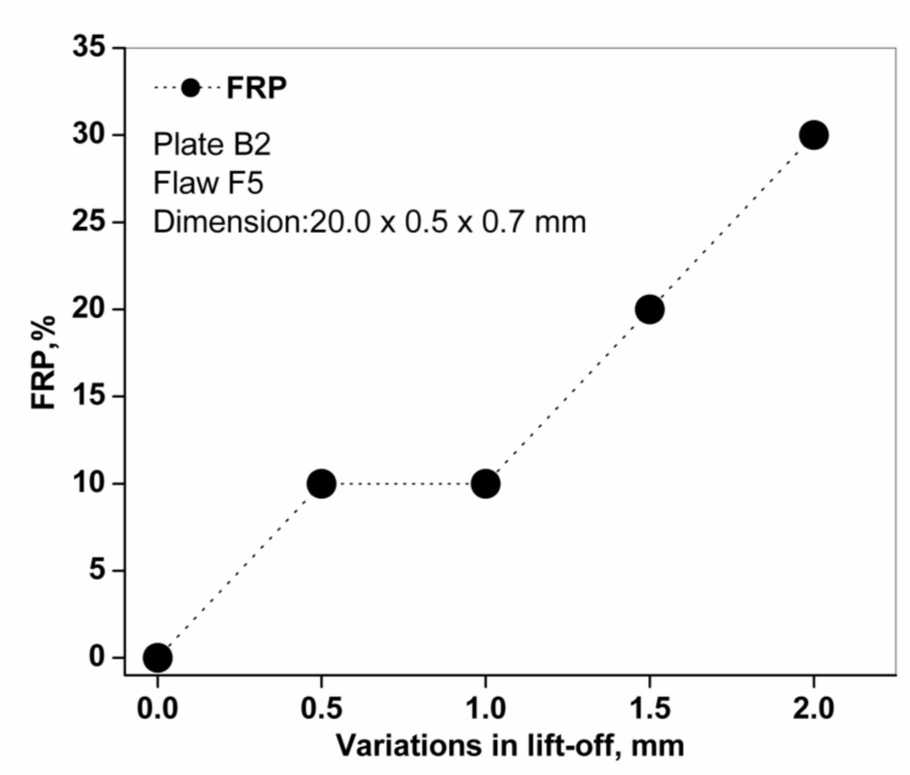

Figure 4.20 Estimated FRP from the DWT processed image of a flaw (F5) in a plate B2 with variations in lift-off.

Table 4.9 Evaluation of the proposed DWT based approach for variations in lift-off noise.

Plate No.	Flaw No.	Variations in lift-off, mm	Input image SNR, dB	Denoised image			
				NRP, %	SNR, dB	Flaw amplitude, V	FRP, %
B1	F1	≤0.5	8.0	90	13.5	0.45	10
		≤1.0	6.8	85	10.2	0.45	10
		≤1.5	5.0	82	9.6	0.4	20
		≤2.0	4.5	70	-0.8	0.35	30
B2	F5	≤0.5	10.0	92	14.0	0.9	10
		≤1.0	7.9	85	10.9	0.9	10
		≤1.5	6.0	80	8.04	0.8	20
		≤2.0	5.1	61	-1.2	0.6	30
B3	F8	≤0.5	10.0	93	14.0	1.2	12
		≤1.0	7.5	87	10.8	1.2	14
		≤1.5	7.2	84	9.8	0.9	35
		≤2.0	6.2	70	-0.7	0.7	50
B4	F15	≤0.5	9.5	92	13.5	1.2	14
		≤1.0	8.2	88	11.5	1.1	21
		≤1.5	7.5	82	9.4	0.8	42
		≤2.0	6.0	69	-0.9	0.7	50

4.3.5.2 Noise from composite source: Variations in lift-off

The noise tolerance of the proposed DWT based approach for EC images of weld plates acquired with higher amount of noise from variations in lift-off (0.0 mm to 1.5 mm, 0.0 mm to 2.0 mm) has been evaluated. EC images of a flaw (F28, length 4.0 mm, width 0.25 mm, depth 0.5 mm) in a weld plate (W1) acquired with variations in lift-off is shown in the first column of Figure 4.21. The corresponding denoised images resulted by the DWT based approach are shown in the second column of Figure 4.21.The estimated NRP, SNR, flaw amplitude and FRP from the processed images are given in Table 4.10.

.

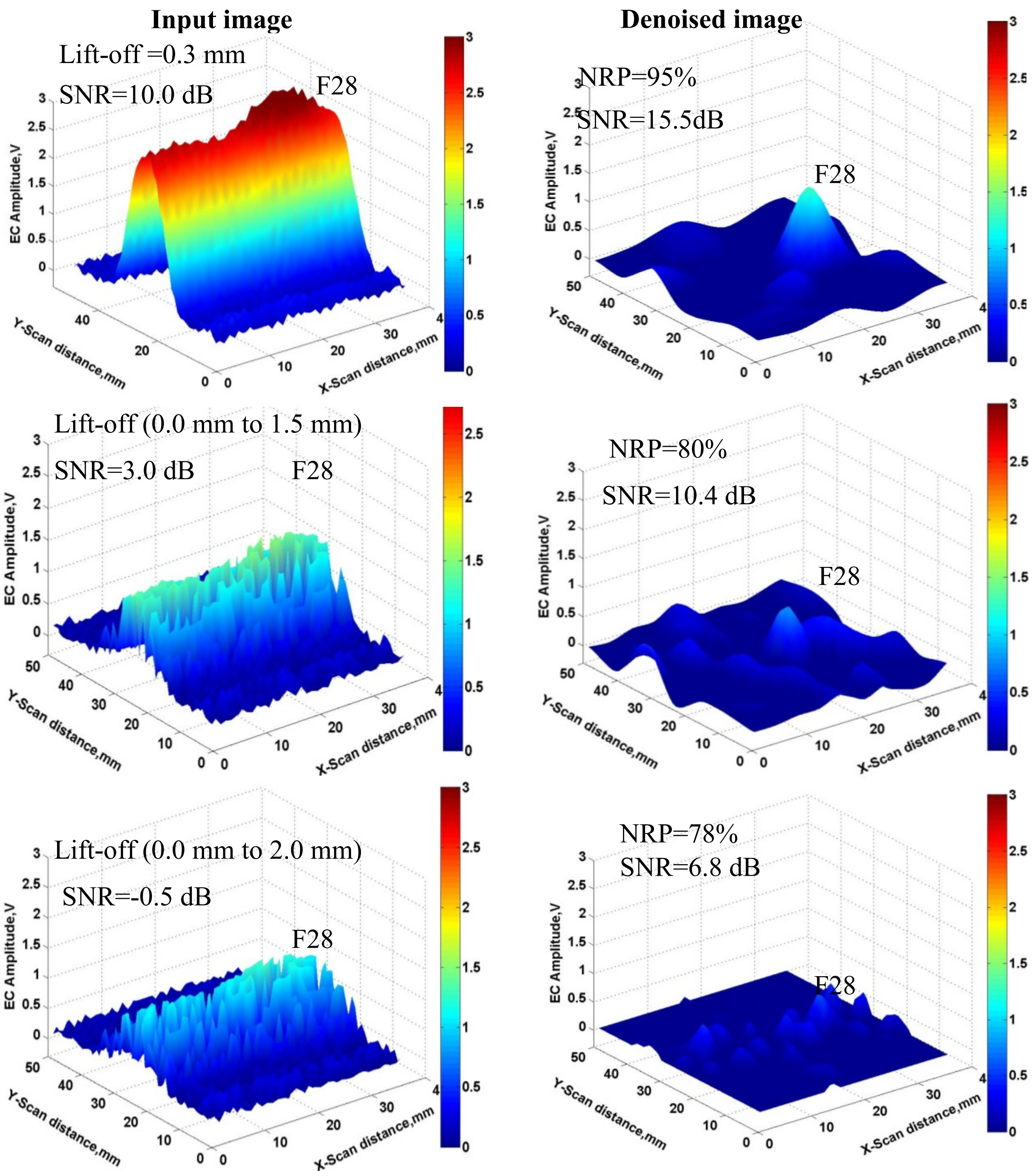

Figure 4.21 Performance of the DWT based approach for variations in composite noise.

Table 4.10 Results of the DWT based approach for variations in composite noise.

Plate No.	Flaw No.	Variations in lift-off, mm	Input image SNR, dB	Denoised image			
				NRP, %	SNR, dB	Flaw amplitude, V	FRP, %
W1	F28	≤0.5	8.0	85	14.0	0.45	10
		≤1.0	4.8	82	12.2	0.38	24
		≤1.5	3.0	80	10.4	0.30	40
		≤2.0	-0.5	78	6.8	0.25	50
W2	F31	≤0.5	7.8	84	14.0	0.48	14
		≤1.0	4.5	80	12.6	0.39	22
		≤1.5	3.2	78	10.2	0.34	32
		≤2.0	-1.0	72	7.8	0.28	44

The influence of the noise on flaw retention ability is estimated in terms of FRP and is shown in Figure 4.22. From Figure 4.22, FRP of 24% is observed. However, at higher variations in lift-off (0.0 mm to 1.5 mm), FRP increases to 50% indicating the higher influence of composite noise on flaw retention ability of the DWT based approach. Though this is an expected result, it has been quantitatively analysed for the first time.

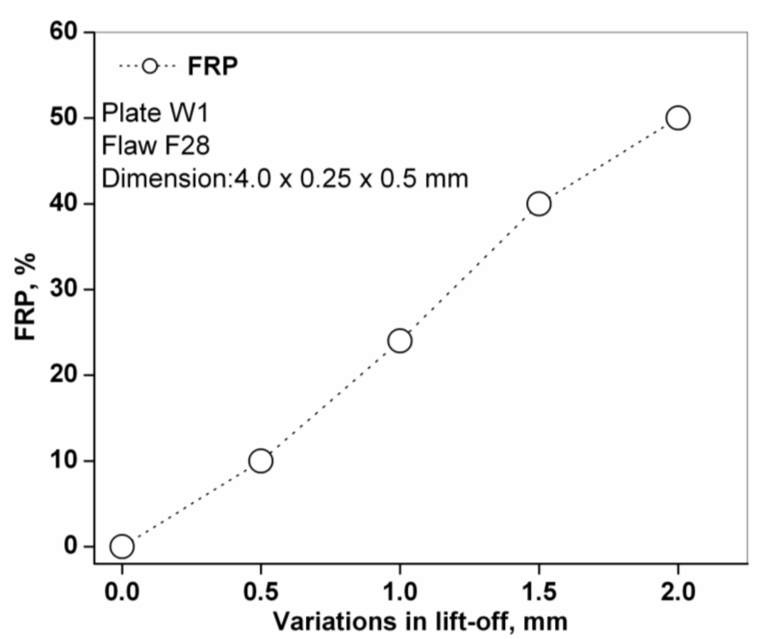

Figure 4.22 Estimated FRP from the DWT processed image of a flaw (F28) in a weld plate W1 for variations in lift-off.

The degradation in flaw amplitude due to the variations in lift-off (single source) and composite noise (two sources) is compared in Figure 4.23 for the shallow surface flaws of depth 0.5 mm using FRP.

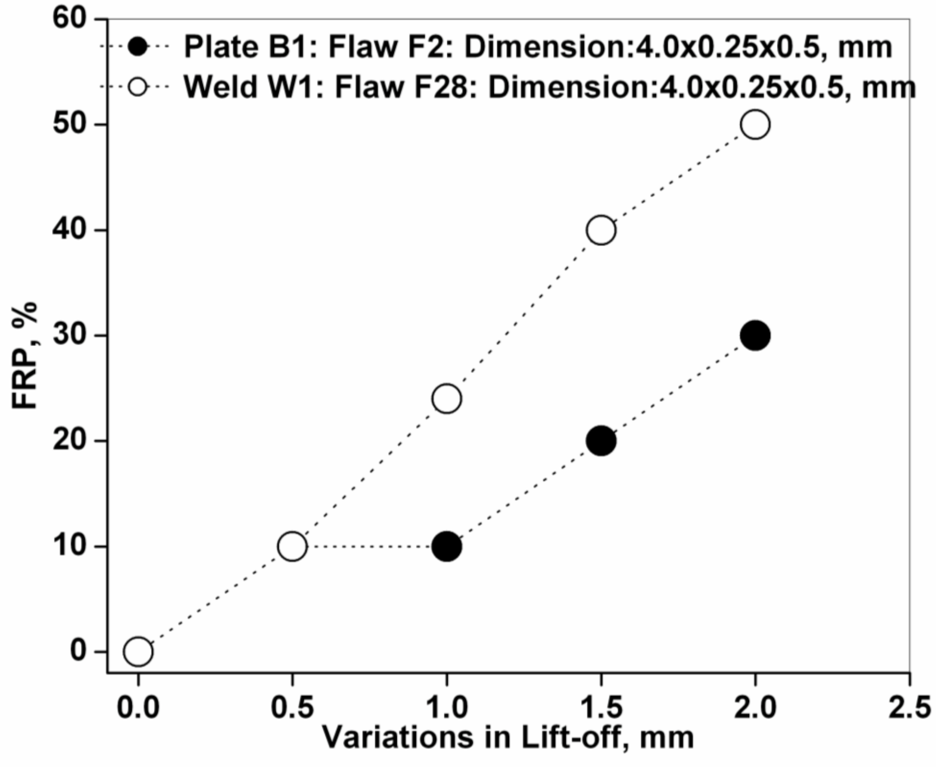

Figure 4.23 Comparison of FRP for single source of noise and composite noise (weld).

From Figure 4.23, no degradation in flaw amplitude is observed for EC images acquired at constant lift-off of 0.3mm. However, FRP increases with increase in lift-off. It indicates the influence of noise on flaw retention ability. This is observed more for the composite noise than for the single source of noise. DWT shows better noise removal of single source of noise as well as composite noise. However, the observation of reduction in flaw amplitude indicates the influence of noise on denoising ability of the proposed DWT based approach and this demands further studies.

4.4 Summary

DWT based approach has been proposed for removal of noise from single source of noise and composite noise in 5.0 mm thick stainless steel plates. Systematic studies on the denoising ability of the proposed approach reveal a definite improvement in noise removal, as a result of optimisation of wavelet filter, decomposition level and thresholding. The observed results are the following:

- The DWT based approach ensures the automated selection of optimal wavelet filter, and decomposition level for processing of EC images.
- It has been established, for the first time, that the wavelet Db5, level 5 is the optimal wavelet for denoising EC images of flaws in SS plates and wavelet Bior6.8, level 5 for denoising EC images of flaws in weld plates.
- The sub-band level thresholding complied with Heursure thresholding method, is established as an optimum thresholding method from this study.
- This semi local paradigm for wavelet thresholding enables selective elimination of noise and achieves enhancement in SNR of 14. 5 dB and NRP of 92% in the presence of single source of noise and SNR of 13.5 dB and NRP of 89% for composite noise.
- The varying test frequencies in the range of 20 kHz-150 kHz and probes of 3.0 mm, 5.0 mm and 20.0 mm have no significant influence on the denoising ability of the proposed approach.
- The flaw retention ability of the proposed approach establishes its noise tolerance up to the variations in lift-off ≤1.0 mm.
- The proposed approach is expected to ensure simultaneous removal of composite noise and detection of shallow flaws in stainless steel plates and welds.

Chapter 5 : Independent component analysis based approach for automated noise removal

Preamble

This chapter proposes an ICA based approach for automated noise removal. In order to considerably reduce the randomness in the estimation of de-mixing matrix, iterative process with flexible learning rule using non-linear functions has been proposed. The denoising capability of ICA based approach has been studied using experimental EC images of flaws in SS plates and welds. The performance of the ICA based approach has been analysed and compared with that of the DWT based approach using NRP, SNR, FRP and flaw amplitude.

5.1 Proposed ICA based approach

ICA that recovers non-gaussianity of the data based on their statistical independency is used for separation of noise from EC images. The statistical independence of the noise characteristics has been utilised for identifying noise in EC images. Hence, the independent component analysis (ICA) technique that calculates the ICs by the maximization of non-Gaussianity or minimization of the mutual information between signals by seeking statistical independence is utilised in this study.

The challenging task in noise removal in EC images is identification and separation of noise as well as flaw information. As per the central limit theorem (§1.4.4.2), Gaussian *pdf* of noise (refer Figure 1.12) shows evidence of its statistical independence of noise in EC images. Following this, ICA based approach that utilises the measure of non-Gaussianity for separation of statistically independent information (noise) is proposed in this study.

The flow chart of the proposed ICA based approach is shown in Figure 5.1. This approach has the following three steps:

1) Pre-processing of input data: The primary step involves centering and whitening of an input image (refer Section §1.4.4.2). It is generally carried out before performing ICA. This pre-processing converts an input image to have zero mean and unit variance data. The reduction in estimation of number of parameters achieved through whitening reduces the computational complexity of the ICA.

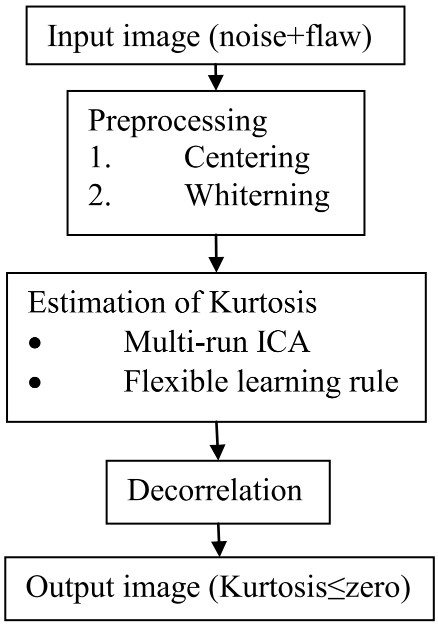

Figure 5.1 Flow chart of the proposed ICA based approach.

2) Iterative estimation of de-mixing matrix (**W**):

   Multi-run ICA is carried out to eliminate randomness in estimation of de-mixing matrix. In this iterative process, flexible learning rule with selection of suitable non-linear function based on the measurement of Kurtosis (refer Section 1.4.4.2) is incorporated.

3) Correlation of de-mixing matrix:

   To identify the independent components of data in the input image, correlation of de-mixing matrix, **W** is carried out. By maximising the non-Gaussianity of $\mathbf{W}^T\mathbf{x}$, **W** separates the statistically independent data (noise), having value of Kurtosis greater than zero. The remaining data having zero value of Kurtosis are statistically dependent and are separated as the flaw components.

5.1.1 *Iterative estimation of de-mixing matrix*

The quality of separation of statistically independent data depends mainly on the estimation of the de-mixing matrix, **W**. The randomness associated with the estimation of the de-mixing matrix influences the quality of separation (refer Section 1.4.4.2). Hence, to overcome this associated randomness, **W** is estimated by an iterative process as shown in Figure 5.2.

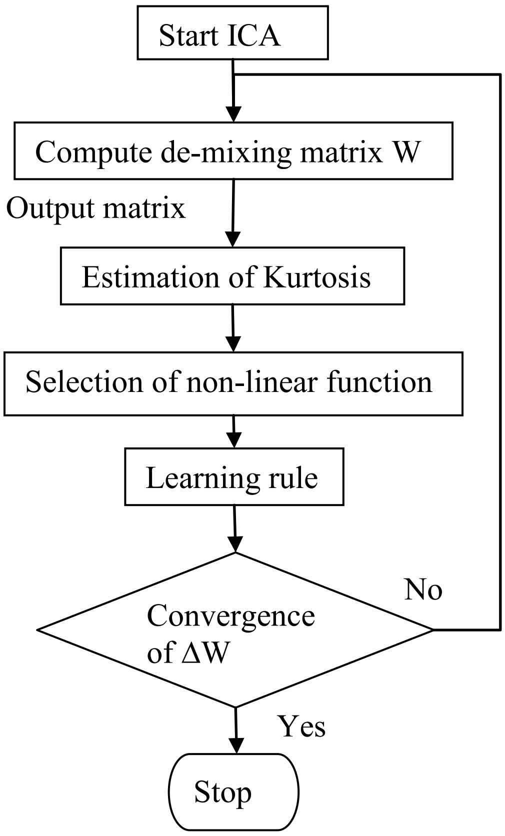

Figure 5.2 Flow chart of iterative estimation of de-mixing matrix.

A multi-run ICA processing is incorporated for an iterative estimation of de-mixing matrix. The iterative estimation process incorporates and establishes a flexible universal learning rule that selectively uses non-linear functions based on Kurtosis of data. At eachrun of ICA processing, the universal learning rule estimates the de-mixing matrices (**$W_1 \ldots W_n$**). For convergence of **W,** a suitable nonlinear filter is selected based on Kurtosis. Generally, the natural gradient rule has emerged as a technique for solving the iterative optimisation problem of **W** taking into account of the gradient of the loss function and is expressed as [63]

$$.\frac{\partial\varphi(W)}{\partial W} = -(WW^T)^{-1}W + f(y)x^T \qquad 5.1$$

where $f_i(y_i) = -\frac{\partial\, log(P_i(y_i))}{\partial y_i}$ *5.2*

The preconditioned filtered gradient rule is given as

$$\Delta W(t) = \eta(t)\big[I - y(t)g\big(y^T(t)\big)\big]W(t) \qquad 5.3$$

However, the conventional learning rule strongly depends on the shape of the activation function $f_i(y_i)$ and $g_i(y_i)$. The selection of this function depends on the nature of the *pdf*s of source signals. The limitation reported is that equation 5.1 is able to separate the source signals, if *pdf* is a heavy tailed super Gaussian signal, whereas the equation 5.2 can separate the source signals with a light tailed *pdf* similar to a sub-Gaussian signal. In EC images, the measured data contain a mixture of both sub-Gaussian and super Gaussian sources (shown in Figure 1.11), then these algorithms fail to separate these signals effectively. To make the learning rule more flexible, the two learning rules (equations 5.1 and 5.3) are combined to form more general and flexible universal learning rule given by.

$$\Delta W(t) = \eta(t)\left[I - f[y(t)]g\left(y^{T}(t)\right)\right]W(t) \qquad 5.4$$

where *f(y(t))* and *g(y(t))* are suitably designed nonlinear functions, e.g.

$$f_i y_i = \begin{cases} \tanh(\beta_i y_i) & for\ k_4(y_i) > \delta \\ . & \\ sign(y_i)|y_i|^{r_i - 1} & otherwise \end{cases} \qquad 5.5$$

$$g_i y_i = \begin{cases} sign(y_i)|y_i|^{r_i - 1} & for\ k_4(y_i) > -\delta \\ \tanh(\beta_i y_i) & otherwise \end{cases} \qquad 5.6$$

where $1 \leq \beta \leq 2$ is a constant $r_i \geq 2$, $k_4(y_i) = E\{y_i^4\}/E^2\{y_i^2\} - 3$ is the normalised value of Kurtosis and $\delta \geq 0$ is a threshold. The value of Kurtosis is evaluated using

$$E\{y_i^q(k+1)\} = (1-\eta)E\{y^q(k)\} + \eta|y_i(k)|^q, \quad (q = 2,4) \qquad 5.7$$

The above learning algorithm monitors and estimates the statistics of each output of the process and depending on sign or value of its normalised Kurtosis (a measure of distance from Gaussianity), automatically selects suitable non-linear functions. Kurtosis is used in view of its simplicity both computational and theoretical. This implementation of learning rule has the following advantages:

- The prior knowledge of source signal (*pdf*) is not required for estimating the independent components of non-Gaussian distribution.
- Suitable selection of nonlinear activation function enables faster convergence rate and stability in separation of all nonGaussian sources.
- One by one estimation of independent components reduces computation cost dramatically.

5.2 Performance evaluation of ICA based approach

The proposed ICA based approach has been systematically evaluated for removal of noise from 1) two single sources viz variations in lift-off or variations in material properties and 2) composite noise viz variations in lift-off and variations in material properties. For this, six numbers of EC images contain these noise are considered for processing. Table 5.1 gives the details of EC images of flaws acquired from plates and weld plates. The performance of ICA based approach has been assessed using NRP, SNR, FRP and flaw amplitude.

Table 5.1 EC images considered for ICA based approach.

EC image -1	EC image-2	EC image -3
• Plate (B1) • variation in lift-off	• Plate (B1) • Flaws (F3,F4) + variation in lift-off	• Plate (B2) • Flaws (F9, F10) + variation in lift-off
EC image -4	**EC image-5**	**EC image -6**
• Weld plate (W1) • variation in lift-off +material property	• Weld plate (W1) • Flaws (F29) + variation in lift-off+ material property	• Weld plate (W1) • Flaws (F31) + variation in lift-off+ material property

5.2.1 Removal of noise from single source

The denoising ability of the proposed ICA approach has been evaluated on an EC image of a flaw-free region in a plate (B1) acquired with variation in lift-off (0.0 mm to 0.5 mm) and is shown in Figure 5.3 (a). The output images of flaw and noise components from ICA based approach are shown in Figure 5.3 (b and c) respectively. A NRP of 99% is observed in the output image.

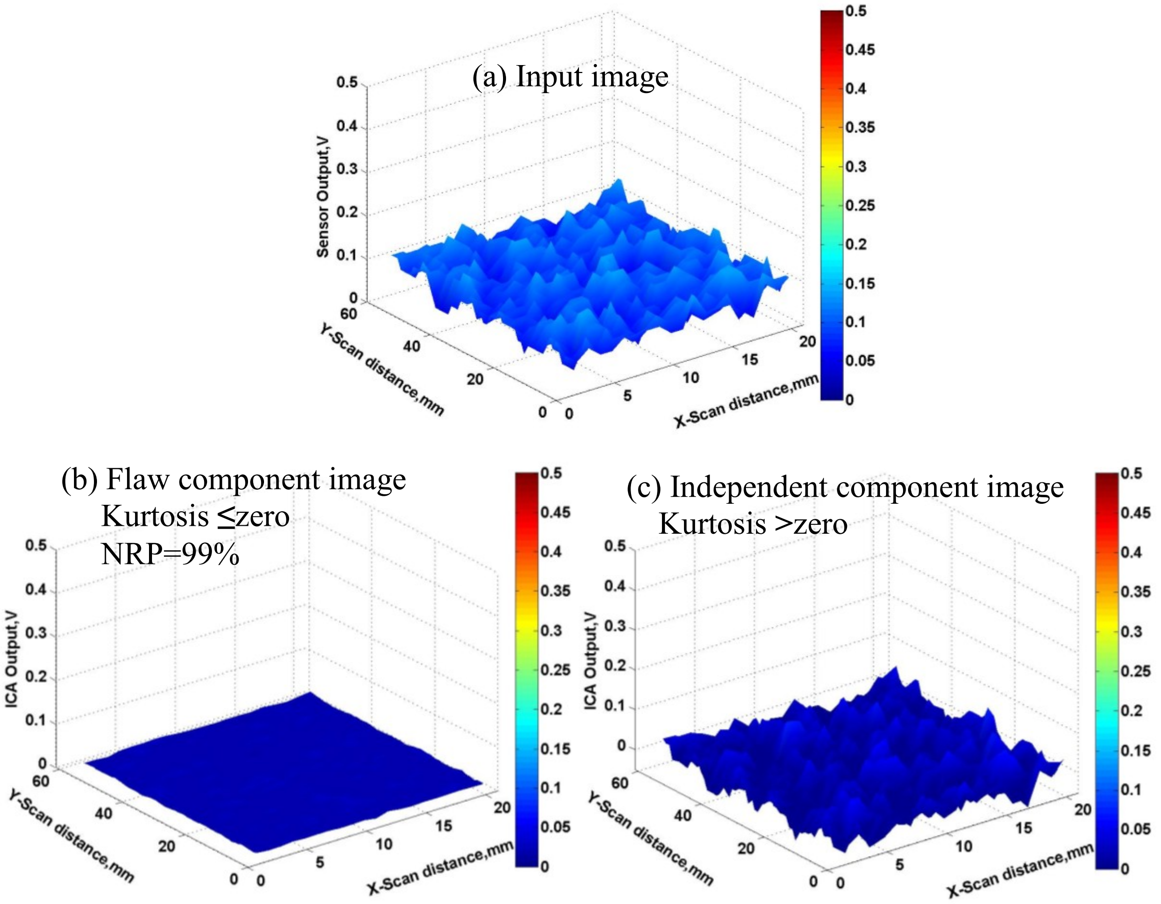

Figure 5.3 EC images of (a) flaw free region in a plate (B1) with variations in lift-off, (b) flaw component image and (c) noise component image from ICA based approach.

Figure 5.4 (a) shows an EC image of a flaw (F3 and F4, length 6.0 mm, width 0.5 mm, depths 0.7 mm and 1.0 mm) in a plate B1 acquired with variation in lift-off (0.0 mm to 1.0 mm). The output images of flaw and noise components from ICA based approach are shown Figure 5.4 (b and c) respectively. A significant improvement in NRP of 94% and SNR of 15.5 dB is observed.

The results of the ICA based approach for single source of noise (variations in material properties) from weld plate (W1) obtained at constant lift-off of 0.3 mm are shown in Figure 5.5. A NRP of 99% is observed.

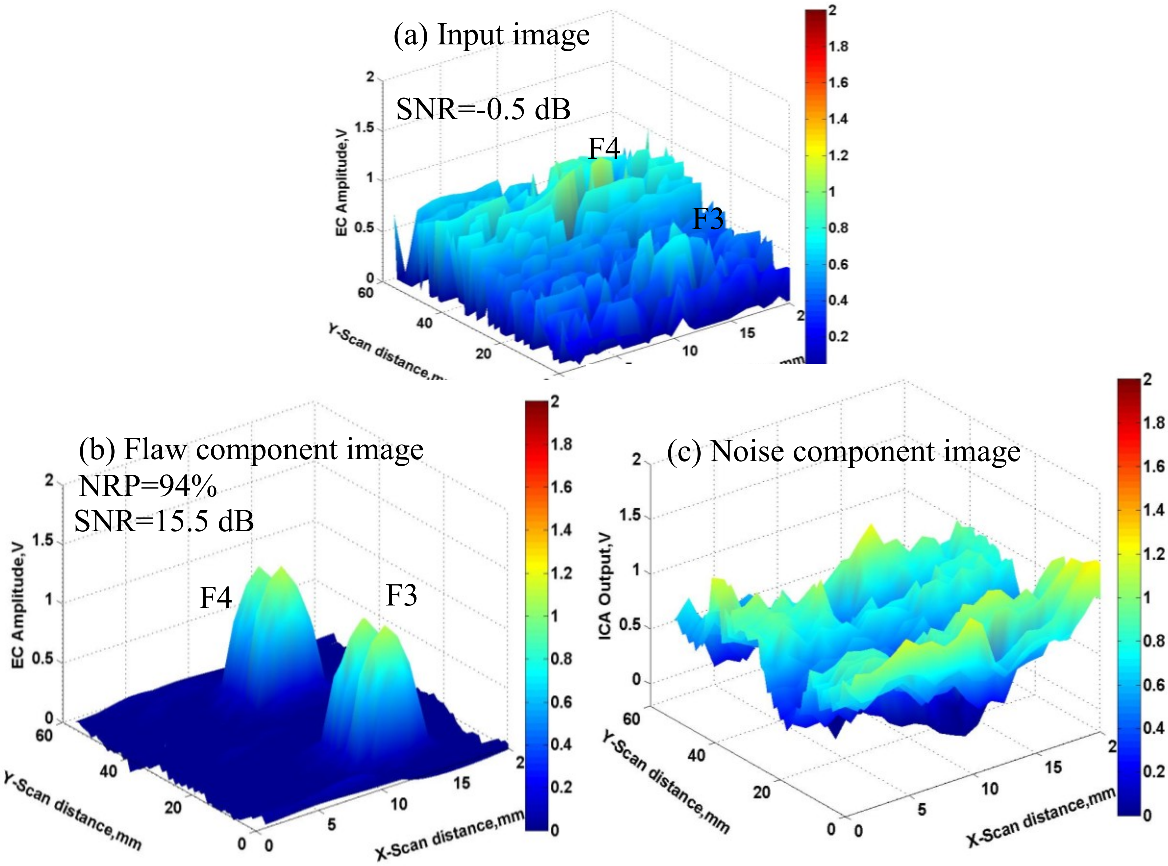

Figure 5.4 EC image of (a) two flaws (F3, F4) in a plate (B1) buried in noise due to variations in lift-off, output images from ICA based approach (b) flaw component (Kurtosis ≤zero) and (c) noise component (Kurtosis>zero).

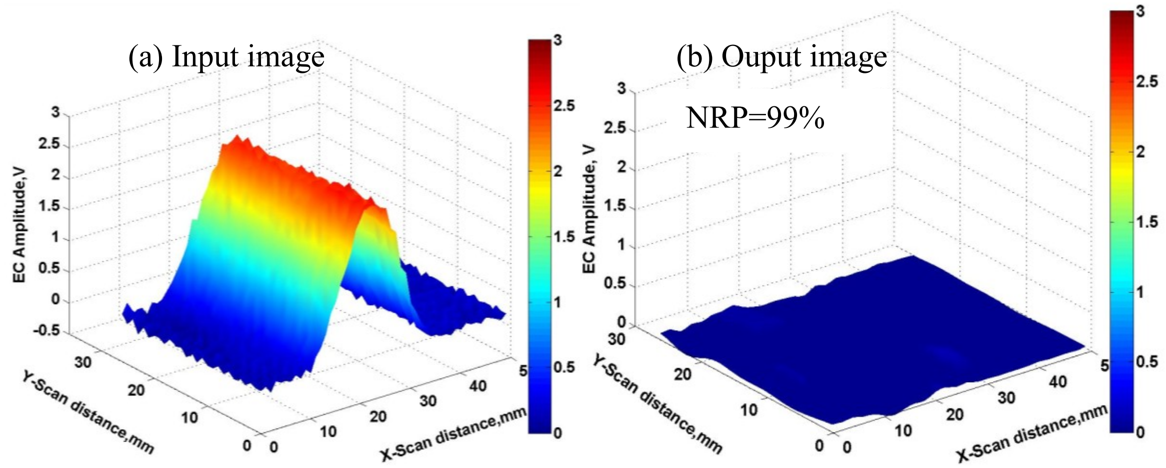

Figure 5.5 EC image of (a) flaw free region in a weld plate (W1) with variations in material properties (single source of noise), (b) output image from ICA based approach.

The flaw separation ability of ICA based approach has been evaluated on an EC image of a flaw (F26, length 4.0 mm, width 0.25 mm, depth 0.2 mm) in a weld plate (W1), with single source of noise from variations in material properties and the results are shown in Figure 5.6 (a). A significant improvement in NRP of 94% and SNR of 14.5 dB are observed.

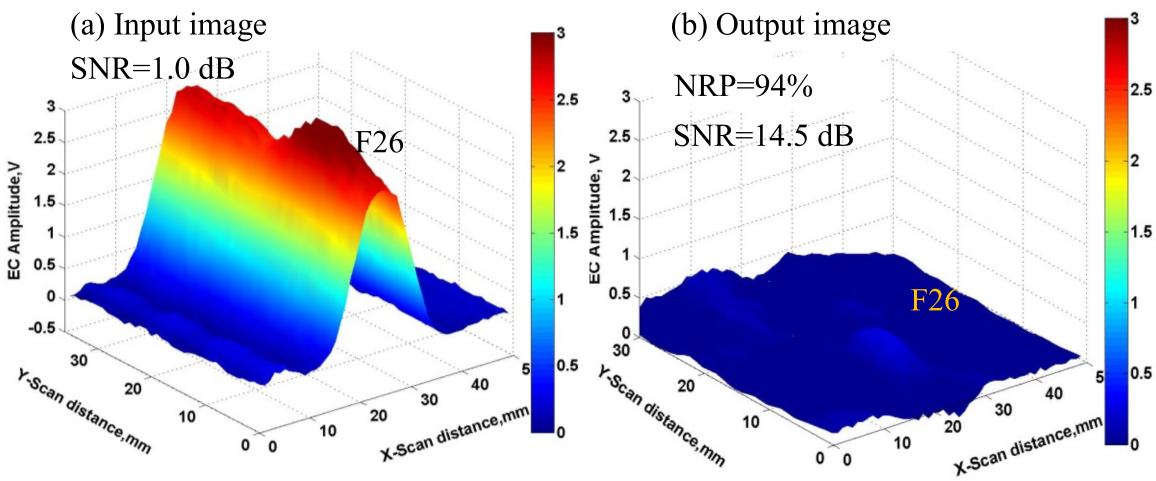

Figure 5.6 EC image of (a) a flaw (F26) in a weld plate (W1), with single source of noise (variations in material properties), (b) output image from ICA based approach.

5.2.2 Removal of composite noise

The proposed ICA based approach has been evaluated for removal of composite noise in EC images acquired in the weld region with variations in lift-off (0.0 mm to 1.0 mm). Figure 5.7 shows an EC image of a flaw (F31, length 6.0 mm, width 0.25 mm, depth 0.5 mm) in a weld plate W2 with composite noise and the results. The NRP and SNR are 82% and 12.5 dB respectively.

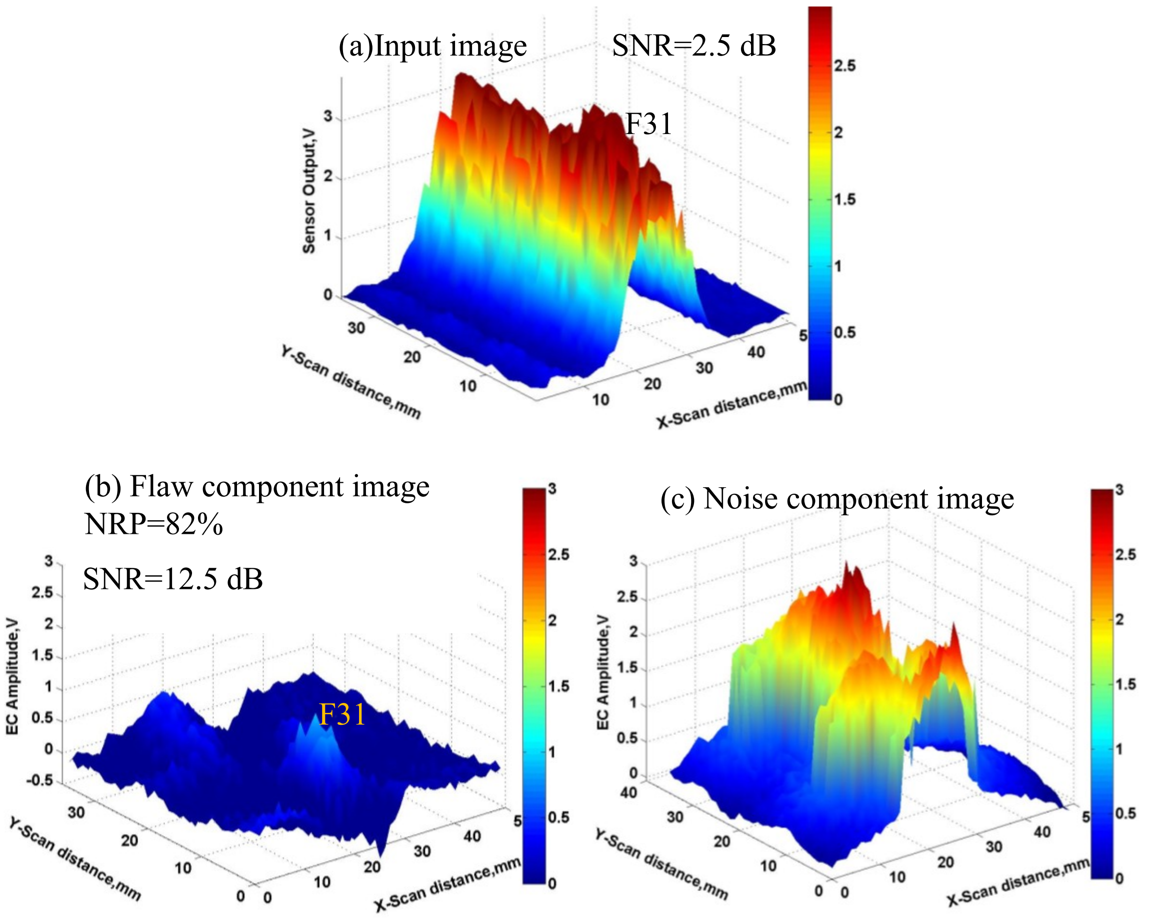

Figure 5.7 EC image (a) of a flaw (F31) in a weld plate (W2) buried in composite noise, output image from ICA based approach (b) flaw component and (c) noise component.

From the results, efficient removal of single source of noise is observed as compared to the composite noise removal. The retention of small amount of noise component is attributed to the statistical dependency of noise, since ICA based approach has limitation in separating the statistically dependent component. On comparing the denoising ability with the proposed DWT based approach, the DWT based approach shows effective removal of composite noise with improved NRP of 90% and SNR of 13.0 dB.

Apart from noise reduction, retention ability of flaw information has been assessed on the reduction in peak amplitude of flaw. The degradation in flaw amplitude is estimated using FRP.

5.2.3 Flaw retention ability

The flaw retention ability of the proposed ICA based approach is evaluated in the presence of noise. The EC image of four flaws (F11, F12, F13 and F14) in a plate (B4) is processed using the proposed ICA based approach and the results are shown in Figure 5.8. The ICA based approach resulted in a NRP of 92% and SNR of 14.0 dB.

The retention capability of flaw information is assessed in terms of flaw amplitude. The same amplitude (1.0 V and 1.4 V) for identical flaws F12 and F13 (length 4.0 mm, width 0.3 mm, depth 0.7 mm and length 6.0 mm, width 0.3 mm, depth 1.0 mm) and flaws F3 and F4 (shown in Figure 5.4) in B1 has been observed, irrespective of the variations in noise distribution in both the plates (B1 and B4).

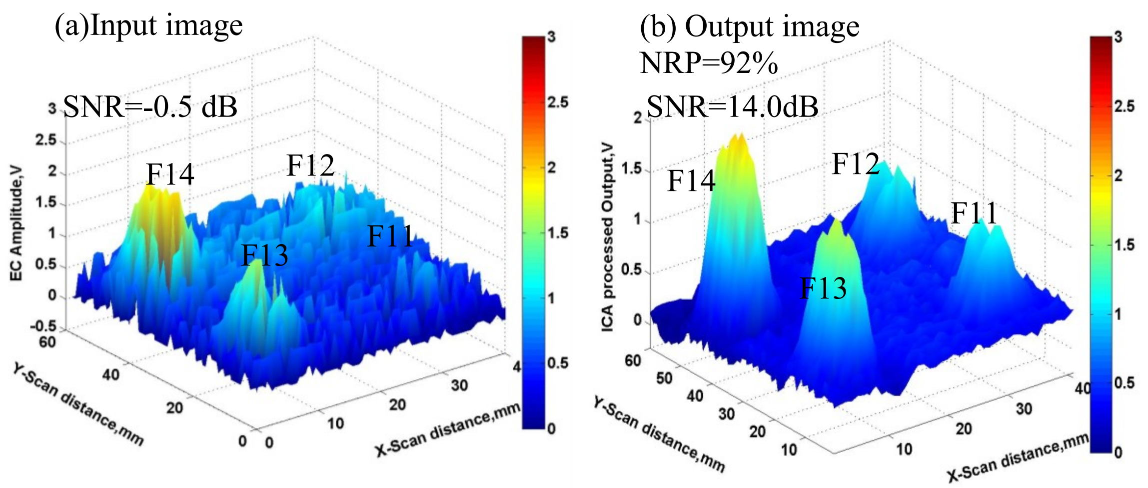

Figure 5.8 EC image of (a) the four flaws (F11, F12, F13, F14) in a plate (B4) buried in noise due to variations in lift-off, (b) output image from ICA based approach.

The noise removal and flaw retention ability of the proposed ICA based approach for several EC images of plates (B1, B2, B3, B4 and B5) and weld plates (W1 and W2) with variations in lift-off (0.0 mm to 1.0 mm) are evaluated. Table 5.2 and Table 5.3 give the estimated NRP, SNR and flaw amplitude from the processed images. From the tables, it is observed that the proposed ICA based approach retains the original amplitude (acquired at constant lift-off) of flaw in plates as well as in weld plates. No reduction in flaw amplitude is observed as compared with the amplitude estimated from the image obtained at constant lift-off of 0.3 mm. The FRP estimated for various flaws is 0%. The flaw retention ability of the proposed ICA approach is noise tolerant up to the variations in lift-off (0.0 mm to 1.0 mm).

Table 5.2 Performance evaluation of the ICA based approach for EC images with a single source of noise.

Plate No.	**Flaw No.**	**Flaw Dimension (length x width x depth), mm**	**Input image SNR, dB**	**Denoised image**			
				NRP, %	**SNR, dB**	**Flaw amplitude, V**	**FRP, %**
B1	F1	4.0x 0.5 x 0.3	6.8	93	14.2	0.3	0
	F2	4.0x 0.5 x 0.5	7.2		14.1	0.5	0
	F3	6.0x 0.5 x 0.7	6.5	92	15.5	1.0	0
	F4	6.0x 0.5 x 1.0	8.5		15.5	1.4	0
B2	F5	20.0 x 0.5x 0.7	6.2	93	13.9	1.0	0
	F6	4.0x 0.5 x 0.7	7.0	93	14.2	1.0	0
B3	F7	4.0x 0.3 x 0.5	6.2	92	14.5	0.5	0
	F8	4.0x 0.3 x 1.0	7.5		14.0	1.4	0
	F9	6.0x 0.5 x 0.7	7.0	93	13.8	1.0	0
	F10	6.0x 0.5 x 1.0	8.0		14.5	1.4	0
B4	F11	4.0 x 0.3x 0.3	4.5	92	14.0	0.3	0
	F12	4.0 x 0.3x 0.5	5.2		14.0	0.5	0
	F13	6.0 x 0.3x 0.7	6.2		14.0	0.9	1
	F14	6.0 x 0.3x 1.5	8.5	93	15.2	1.8	0
	F15	8.0 x 0.3x 1.0	7.5		15.5	1.4	0
	F16	8.0 x 0.3x 2.0	9.2		16.5	2.4	0
	F17	8.0 x 0.5x 0.5	5.5		13.3	0.5	0
	F18	8.0 x 0.5x 1.0	7.5	93	14.5	1.4	0
	F19	8.0 x 0.5x 2.0	9.2		14.0	2.4	0

Table 5.3 Performance evaluation of the ICA based approach for EC images with composite noise.

Weld Plate No.	Flaw No.	Flaw Dimension (length x width x depth), mm	Input image SNR, dB	Denoised image			
				NRP, %	SNR, dB	Flaw amplitude, V	FRP, %
W1	F26	4.0 x 0.25 x 0.2	4.0	80	12.8	0.2	0
	F27	4.0 x 0.25 x 0.3	4.2	80	13.0	0.3	0
	F28	4.0 x 0.25 x 0.5	4.8	83	13.0	0.5	0
	F29	6.0 x 0.25 x 0.5	4.8	85	12.5	0.5	0
	F30	6.0 x 0.25 x 1.0	5.5	80	13.0	1.4	0
W2	F31	6.0 x 0.25 x 0.5	4.5	80	12.5	0.5	0
	F32	6.0 x 0.25 x 2.0	5.5	80	12.9	2.4	0
	F33	8.0 x 0.25 x 0.3	4.2	82	13.0	0.3	0
	F34	8.0 x 0.25 x 0.5	4.5	82	13.0	0.5	0
	F35	8.0 x 0.25 x 0.6	4.8	82	13.0	0.65	0

The significant removal of noise and enhancement in SNR is observed from Table 5.2 and Table 5.3. The proposed ICA approach could detect the shallowest flaw (depth 0.2 mm, <10% of wall thickness) with an improved SNR of 12.8 dB.

5.2.4 Evaluation of noise tolerance on denoising ability

5.2.4.1 Noise from single source: Variations in lift-off

The noise tolerance of the proposed ICA based approach for higher amount of noise from variations in lift-off ≥ 1.0 mm (0.0 mm to 1.5 mm, 0.0 mm to 2.0 mm) is evaluated. The input input images of a flaw (F5, length 20.0 mm, width 0.5 mm, depth 0.7 mm) in a plate B2 acquired with variations in lift-off are shown in the first column of Figure 5.9. The corresponding denoised EC images from the proposed ICA based approach are shown in the second column of Figure 5.9. It is observed that, NRP as well as SNR decrease with increase in the variations in lift-off Figure 5.9. From Figure 5.9, the noise removal as well as flaw retention abilities of the proposed ICA approach is observed for higher amount ofnoise variations (lift-off of ≤ 1.5 mm).

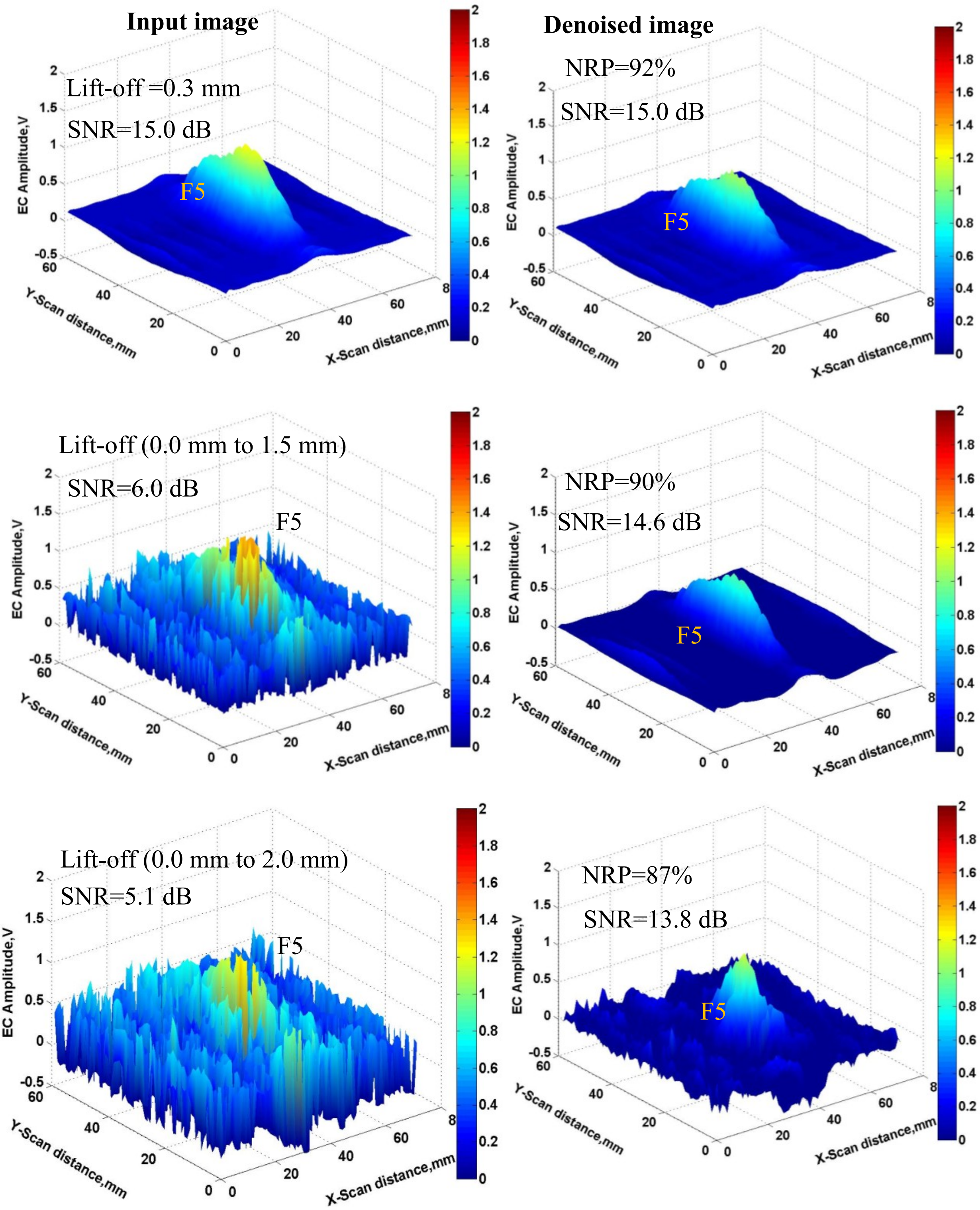

Figure 5.9 Performance of the ICA based approach for variations in lift-off.

Figure 5.10 shows the estimated FRP for the processed EC image of a flaw F5 in plate B2 for variations in lift-off. From Figure 5.10, it is observed that the FRP (F5, length 20.0 mm, width 0.5mm, depth 0.7 mm) is estimated as 0% and retained up to variations in lift-off ≤1.5 mm. FRP of 10% is observed for 0.0 mm to 2.0 mm variations in lift-off. It is noted that the reduction in amplitude is less (FRP of 10%) for the ICA based approach as compared to the DWT based approach (FRP of 50%).

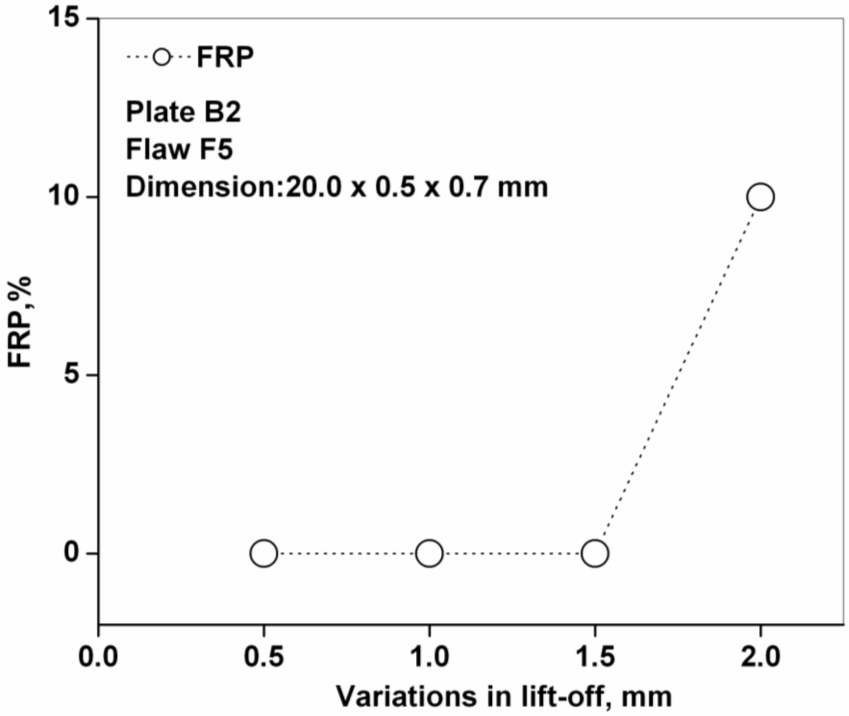

Figure 5.10 Estimated FRP from the ICA processed image of a flaw (F5) in a plate B2 for variations in lift-off.

The NRP, SNR, flaw amplitude and FRP are estimated from a number of processed images and are given in Table 5.4. From the table, the decrease in NRP as well as SNR is observed for the increase in variations in the lift-off. However, the reduction in flaw amplitude in the processed image is less as compared with the peak amplitude of flaws obtained at constant lift-off of 0.3 mm. The estimated value of FRP is less as compared to the DWT based approach (Table 4.8) in the presence of noise due to variations in lift-off(> 1.5 mm).

Table 5.4 Evaluation of the proposed ICA based approach for variations in lift-off.

Plate No.	Flaw No.	Variations in lift-off, mm	Input image SNR, dB	Denoised image			
				NRP, %	SNR, dB	Flaw amplitude, V	FRP, %
B1	F1	≤0.5	8.0	93	12.0	0.5	0
		≤1.0	6.8	92	10.2	0.5	0
		≤1.5	5.0	90	9.6	0.5	0
		≤2.0	4.5	88	-0.8	0.45	10
B2	F5	≤0.5	10.0	92	15.0	1.0	0
		≤1.0	7.9	91	14.6	1.0	0
		≤1.5	6.0	90	14.6	1.0	0
		≤2.0	5.1	87	13.8	0.9	10
B3	F8	≤0.5	10.0	93	14.0	1.4	0
		≤1.0	7.5	90	10.8	1.4	0
		≤1.5	7.2	90	9.8	1.38	1
		≤2.0	6.2	86	-0.7	1.25	8.5
B4	F15	≤0.5	9.5	92	13.2	1.4	0
		≤1.0	8.2	90	11.5	1.4	0
		≤1.5	7.5	90	9.4	1.37	2
		≤2.0	6.0	85	-0.9	1.28	8

5.2.4.2 Noise from composite source: Variations in lift-off

The noise tolerance of the proposed ICA based approach has also been evaluated for EC images of weld plates acquired with higher amount of noise from variations in lift-off (0.0 mm to 1.5 mm, 0.0 mm to 2.0mm. EC images of a flaw (F28, length 4.0 mm, width 0.25 mm, depth 0.5 mm) in a weld plate (W1) acquired with variations in lift-off and results are shown in Figure 5.11. It is observed that, NRP as well as SNR decrease with increase in the variations in lift-off.

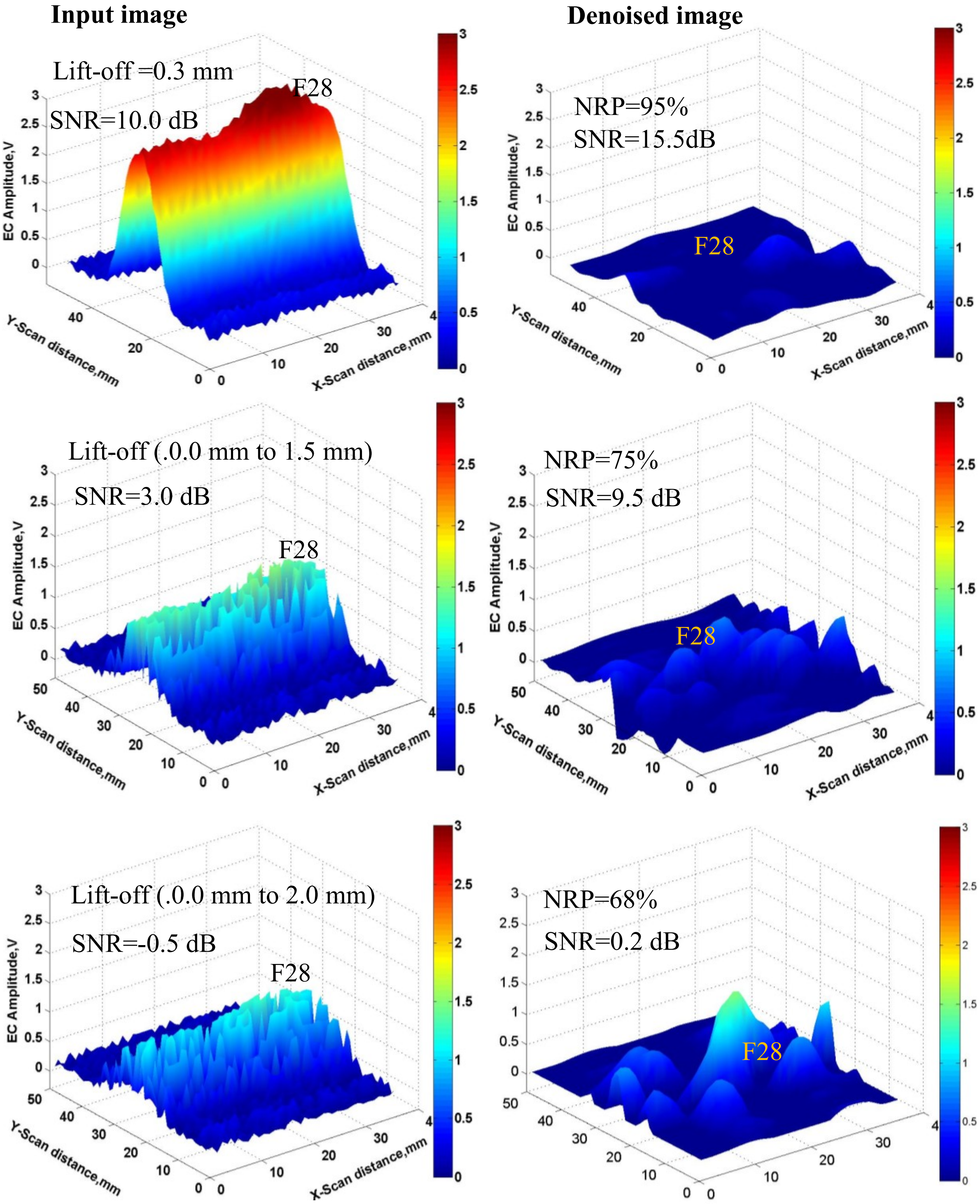

Figure 5.11 Performance of the ICA based approach for variations in composite noise.

Figure 5.12 shows the estimated FRP for the processed EC image of a flaw (F28, length 4.0 mm, width 0.25 mm, depth 0.5 mm) in a weld plate (W1) for variations in lift-off. As can be seen the FRP is estimated as 0% up to variations in lift-off (0.0 mm to 1.0 mm) and this degrades to 16% (FRP for 0.0 mm to 2.0 mm variations in lift-off. It is noted that the reduction in amplitude is less (FRP of 16%) as compared to the DWT based approach (FRP of 50%).

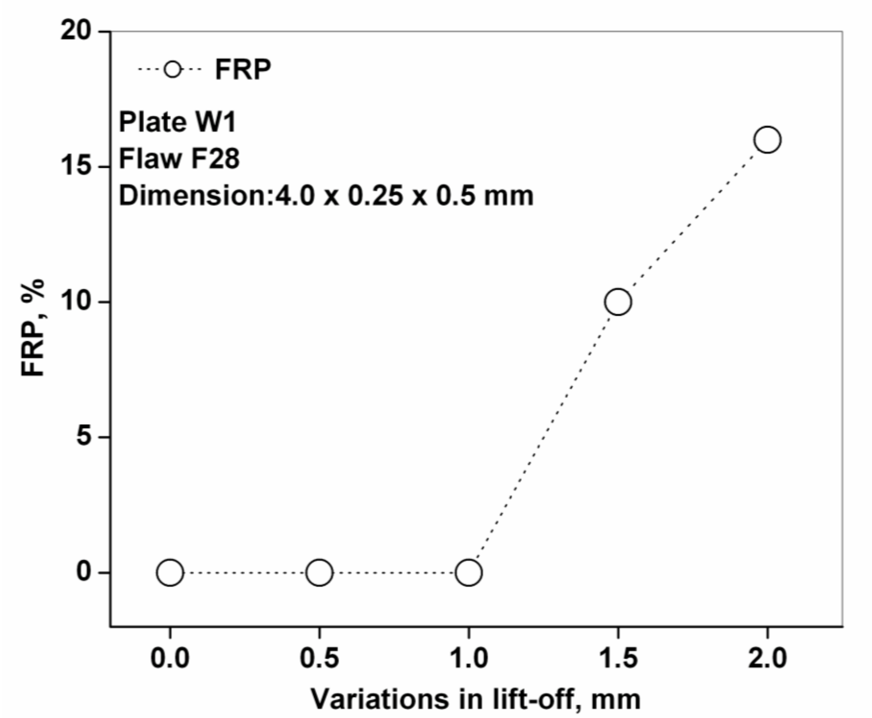

Figure 5.12 Estimated FPR from the ICA processed image of a flaw (F28) in a plate W1 for variations in lift-off.

The NRP, SNR, flaw amplitude and FRP are estimated from a number of processed images and are given in Table 5.5. From the table, the decrease in NRP as well as SNR is observed for the increase in variations in composite noise as compared to the lift-off (single source, Table 5.4) noise. However, it is found that the same amplitude of flaw is retained as compared to the DWT based approach (Table 4.8).

Table 5.5 Evaluation of the proposed ICA based approach for variations in lift-off.

Plate No.	Flaw No.	Variations in lift-off, mm	Input image SNR, dB	Denoised image			
				NRP, %	SNR, dB	Flaw amplitude, V	FRP, %
W1	F28	≤0.5	8.0	85	14.0	0.5	0
		≤1.0	4.8	80	10.2	0.5	0
		≤1.5	3.0	75	9.5	0.45	10
		≤2.0	-0.5	68	0.2	0.42	16
W2	F31	≤0.5	7.8	85	14.0	0.5	0
		≤1.0	4.5	80	10.0	0.5	0
		≤1.5	3.2	73	8.4	0.45	10
		≤2.0	-1.0	71	0.2	0.42	16

The degradation in flaw amplitude due to the influence of varying amount of noise viz. variations in lift-off (single source) and composite noise (two sources) is compared for the shallow surface flaws of depth 0.5 mm using FRP are shown in Figure 5.13. From Figure 5.13, no degradation in flaw amplitude is observed for EC images acquired at constant lift-off as well as up to the variations in lift-off 0.0 mm to 1.0 mm. It indicates the less influence of noise on flaw retention ability as compared to the DWT based approach.

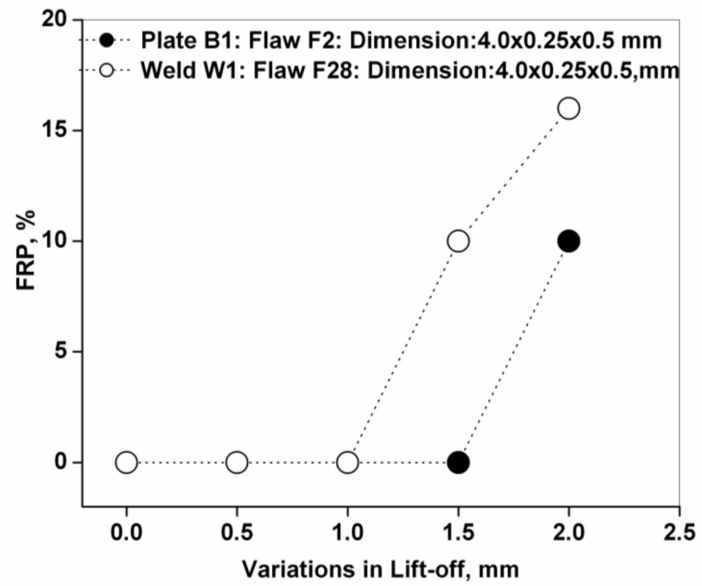

Figure 5.13 Evaluation of noise tolerance of ICA based approach in the presence of single source and composite noise.

5.2.5 *Influence of test parameters*

The influence of testing frequency and diameter of the EC probe on denoising ability of the proposed ICA based approach is evaluated. The several EC images of plates (B1, B2, B3) and weld plates (W1, W2) acquired using probes of 5.0 mm and 20.0 mm diameter at testing frequencies of 75 kHz and 20 kHz are processed using the proposed ICA based approach.

Figure 5.14 (a) shows the EC image of four flaws (F1, F2 - length 4.0 mm, width 0.5 mm, depths 0.3 mm, 0.5 mm and F3, F4 - length 6.0 mm, width 0.5 mm, depths 0.7 mm, 1.0 mm) in a plate (B1) acquired with variations in lift-off (0.0 mm to 1.5 mm) using probe of 5.0 mm diameter operating at test frequency of 75 kHz. The NRP of 92% and SNR of 14.2 dB are observed in the output image (Figure 5.14 (b) and promises the same ability of noise removal.

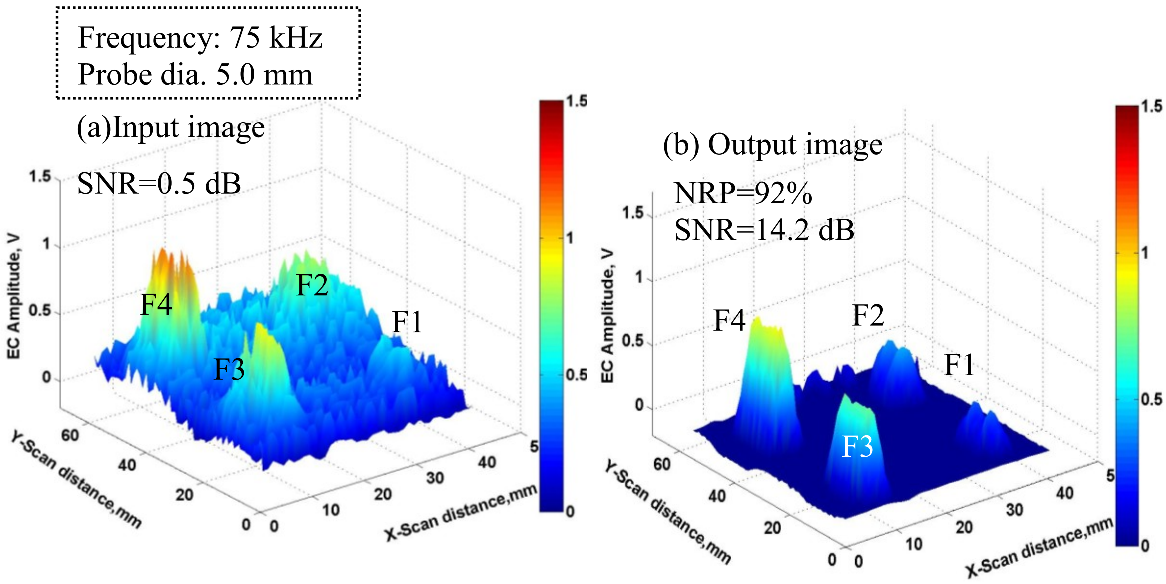

Figure 5.14 EC image of (a) four flaws (F1-F4) in a plate (B1) using 5.0 mm diameter probe (5 kHz), (b) output image from ICA based approach.

Figure 5.15 (a) shows the EC image of a flaw (F26-length 4.0 mm, width 0.25 mm, depth 0.2 mm) in a weld plate (W1) acquired with variations in lift-off (0.0 mm to 1.5 mm) using 5 kHz probe operating at 75 kHz. The NRP of 80% and SNR of 12.8 dB are observed in the output image (in Figure 5.15 b).

From these results, it is observed that no significant influence of testing parameters viz. varying diameter of 3.0, 5.0, 20.0 mm and frequencies of 20 kHz, 75 kHz and 150 kHz, on the denoising ability of the proposed ICA based approach.

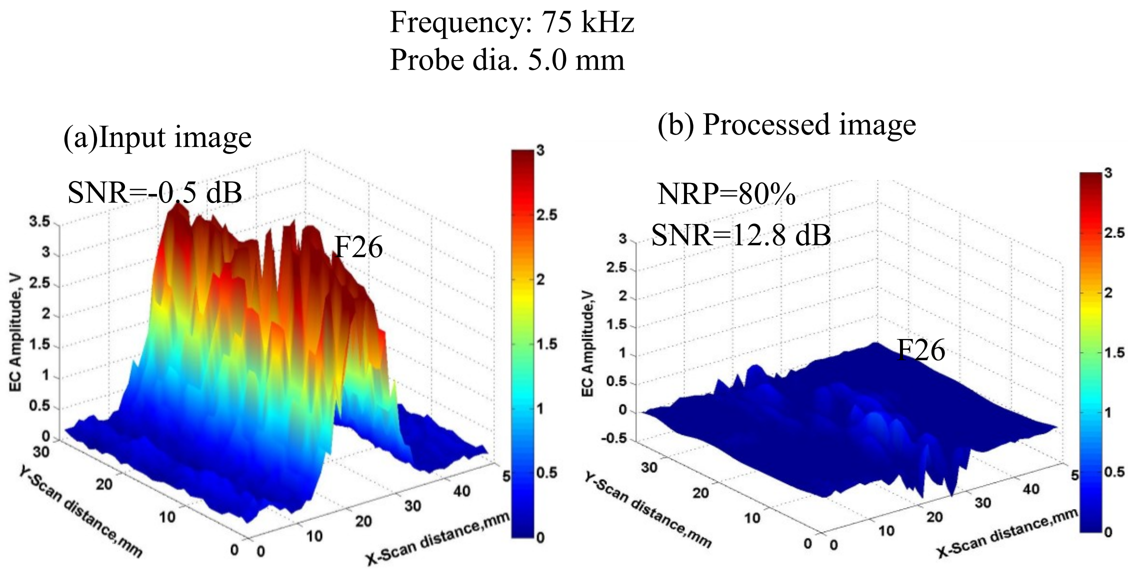

Figure 5.15 EC image of (a) a flaw (F26) in a weld plate (W1) using 5.0 mm diameter probe (5 kHz), (b) processed image from the proposed ICA based approach.

5.3 Comparative study on DWT and ICA based approaches

The denoising ability of the proposed DWT and ICA based approaches has been compared using NRP and flaw amplitude for a flaw (F28) in a weld plate (W1) and the results are shown in Figure 5.16.

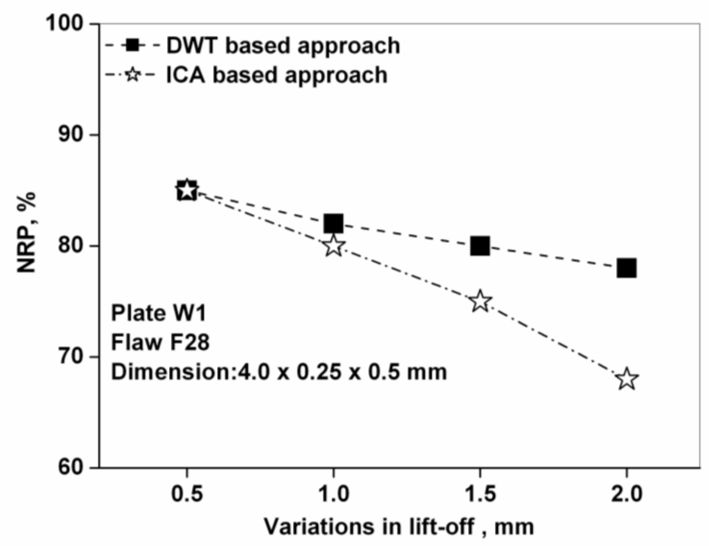

Figure 5.16 Estimated NRP of the processed images from the DWT and ICA based approaches.

A significant removal of composite noise at higher lift-off variations is achieved by the DWT based approach as compared to the ICA based approach. However, ICA based approach has shown promising performance for separation of flaw by retaining equal amplitude for identical flaws, despite variations in noise distribution in weld plates (refer Section 1.3.3).

The retention ability of flaw amplitude of the ICA and DWT based approaches for varying amount of noise due to lift-off variations (single source) and composite noise (two sources) is analysed. The denoised EC images of flaws of depth 0.5 mm (F1, F28) from plate (B1) and weld plate (W1) have been assessed for variations in lift-off noise. The peak amplitude at the flaw region of the processed image from DWT based approach and ICA based approach are plotted and are shown in Figure 5.17.

In the ICA based approach, the same amplitude of the flaw (0.5 V) has been retained even in the presence of (single source of noise) lift-off variations up to 1.5 mm. However, in the presence of composite noise, flaw retention ability is noise tolerant up to 1.0 mm variation in lift-off, higher as compared to the DWT based approach. For higher variations (≤2.0 mm), the reduction in amplitude in the presence of single source (lift-off) of noise is found to be 10% (0.05 V). In the case of composite noise, reduction is about 16% (0.08 V).

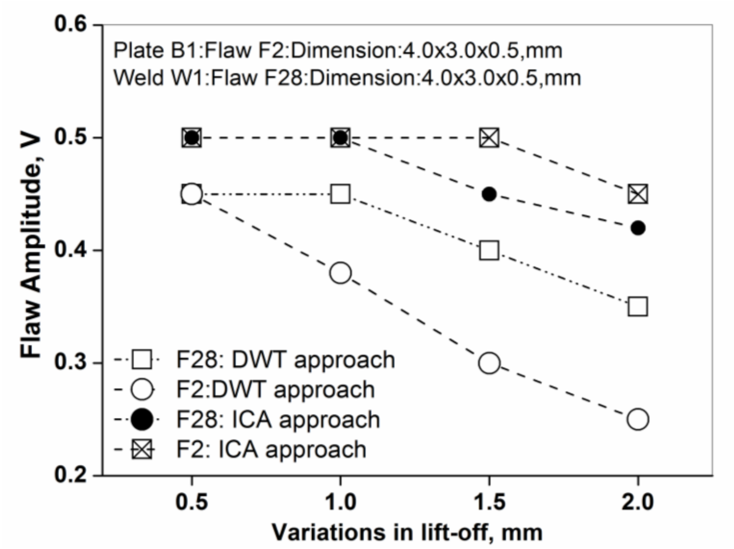

Figure 5.17 Flaw retention ability of the proposed DWT and ICA based approaches under the influence of variations in lift-off noise.

The flaw retention ability of the ICA based approach is attributed to the estimation of optimal de-mixing matrix that improves the separation of statistically dependent variable (flaw) from noise.

In the DWT based approach, better denoising ability is observed for composite noise as compared to the ICA based approach. However, the flaw retention ability of the ICA based approach is observed, despite variations in noise distributions. It indicates the flaw retention ability is noise tolerant as compared to the DWT based approach.

To enhance the noise removal ability of the ICA based approach, sub decomposition of the ICA components by a narrow band filtering is found attractive (refer Section 1.4.4.2). By the use of narrow band filtering process, the wide band of signals having dependency among them can be represented as the sum of a few independent subcomponents and dependent subcomponents with different frequency bands. DWT, a well known narrow band filtering based on spectral dependence and is found to be an attractive candidate.

The results indicate that combining the noise reduction ability of the DWT based approach and the flaw retention ability of the ICA based approach is advantageous for better noise reduction and flaw retention.

5.4 Summary

ICA based approach established with an iterative estimation of de-mixing matrix has been proposed for removal of noise from single source and composite noise in 5.0 mm thick stainless steel plates. The following results are observed:

- An iterative estimation algorithm to optimise the de-mixing matrix has been proposed.
- The proposed ICA based approach has ensured enhancement in SNR of 14. 5 dB and NRP of 93% in the presence of single source of noise and SNR of 13.5 dB and NRP of 80% for composite noise, which is three times the SNR of the input images (4.5 dB).
- The flaw retention ability of the proposed approach establishes its noise tolerance up to the variations in lift-off 0.0 mm to 1.5 mm for single source of noise and up to the variations in lift-off 0.0 mm to 1.0 mm for composite noise.

- No significant influence on the denoising ability of the proposed approach observed for various diameters of probes of 3.0 mm, 5.0 mm and 20.0 mm and varying test frequencies in the range of 20 kHz-150 kHz
- The approach could detect shallows flaws (depth 0.2 mm <10% wall thickness) of comparable amplitude with that of noise.

Chapter 6 : Hybrid image processing approach for automated noise removal

Preamble

This chapter proposes a hybrid image processing approach that combines the advantages of the DWT based approach and ICA based approach. This chapter presents the performance analysis of two sequences of combination of these approaches (DWT-ICA, ICA-DWT) using NRP, SNR and flaw amplitude. This chapter describes how ICA based approach followed by DWT based approach is the optimal sequence for achieving efficient noise removal and discusses the denoising ability of the proposed hybrid ICA-DWT based approach.

6.1 Hybrid Image processing approaches : DWT-ICA and ICA-DWT

A hybrid image processing approach has been proposed by combining the advantages of the noise reduction ability of the DWT approach discussed in Section 4.5 and the flaw retention ability of the ICA approach demonstrated in Section 5.3. In this approach, frequency dependency of flaws and statistical independence of noise is utilised to efficiently remove noise in EC images. The flaw retention ability of the ICA based approach is indeed the primary motivation to join the DWT and ICA based approaches. The orthogonality of the DWT components together with the linearity of the ICA components allows possible combination of the DWT and ICA based approaches to propose a hybrid image processing approach. Two possible combinations are 1) DWT-ICA and 2) ICA-DWT. The performance of these two approaches has been analysed using NRP, SNR, flaw amplitude and FRP.

6.1.1 Hybrid DWT-ICA based approach

In this approach, the input EC image is first processed by the DWT approach comprising optimisation of wavelet filter, decomposition level and Heursure sub-band level thresholding (refer Section 4.1.1). The output EC image is then processed by the ICA approach. The flow chart of the hybrid DWT-ICA based approach is shown in Figure 6.1.

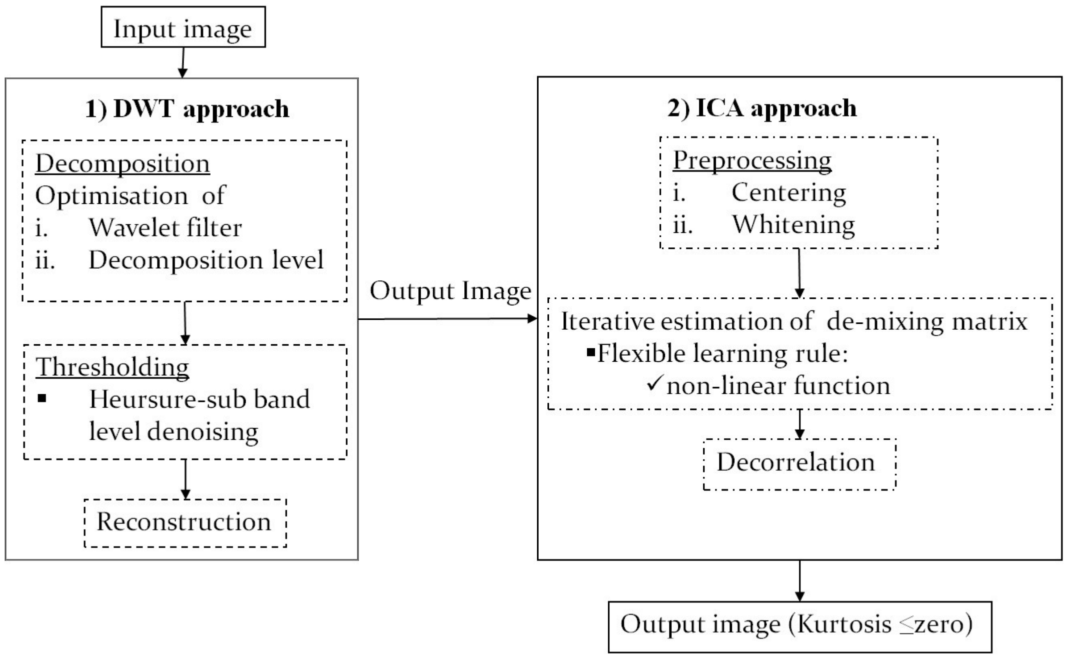

Figure 6.1 Flow chart of hybrid DWT-ICA based approach.

6.1.2 Hybrid ICA-DWT based approach

In this approach, the flaw component from the ICA approach is decomposed into frequency domain by the DWT approach. The flow chart of the hybrid ICA-DWT is shown in Figure 6.2.

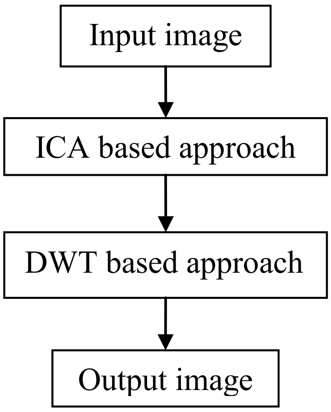

Figure 6.2 Flow chart of hybrid ICA-DWT based approach.

The denoising ability of the hybrid DWT-ICA and ICA-DWT based approaches have been evaluated on a number of EC images having noise due to a) single source of noise and b) composite noise and comparative assessment has been made.

6.2 Performance Evaluation of hybrid approaches

6.2.1 Removal of noise from single source

EC image of four flaws (F11, F12, F13 and F14) (length 4.0 mm, width 0.3 mm, depth 0.3 mm, 0.7 mm and length 6.0 mm, width 0.3 mm, depths 0.7 mm, 1.0 mm) in a plate (B4) has been processed by DWT-ICA and ICA-DWT based approaches. Figure 6.3 shows the input image and processed image from each stage of these approaches.

In the hybrid DWT-ICA based approach, at the first stage of processing, the proposed DWT based approach achieves NRP of 80%. Further processing through ICA based approach shows the improvement in NRP to 88% and SNR from 12.5 dB to 13.5 dB. However, the estimation of peak amplitude of the shallow flaw (F11) shows 10% (FRP) reduction. This is attributed to the removal of wavelet coefficients of flaw of having at the frequencies relevant to the noise information in a few DWT levels.

In the hybrid ICA-DWT based approach, the first stage of the ICA approach has achieved NRP of 90% and SNR of 14.0 dB with retention of small amount of noise. However, the subsequent DWT approach has improved FRP of 95% and SNR of 15.2 dB. From the results, it is clear that the ICA-DWT based approach keeps the flaw amplitude unchanged and good flaw retention ability. The flaw degradation (FRP) is less and is achieved by the removal of statistical dependence of the noise by frequency dependency by the proposed DWT based approach resulting in better denoising and enhanced SNR. On comparing both these approaches, the ICA-DWT based approach has shown effective denoising and flaw enhancement in the presence of noise due to variations in lift-off.

6.2.2 Removal of composite noise

The two hybrid approaches have been evaluated for removal of composite noise in EC images. EC image of a flaw (F31, length 6.0 mm, width 0.25 mm and depth 0.5 mm) in a weld plate (W2) acquired with variations in lift-off (0.0 mm to 1.5 mm) has been processed. The input image and processed images from the each stage of these approaches are shown in Figure 6.4.

In the hybrid DWT-ICA based approach, the results show that the DWT approach achieves NRP of 88%. The subsequent processing by the ICA approach improves the NRP to 90%. However, some of the statistical dependent noise is still present in the image due to the limitation of the ICA approach (statistical dependency of noise). It is observed that the amount of retained noise is less as compared to the noise removal by the individual DWT and ICA approaches.

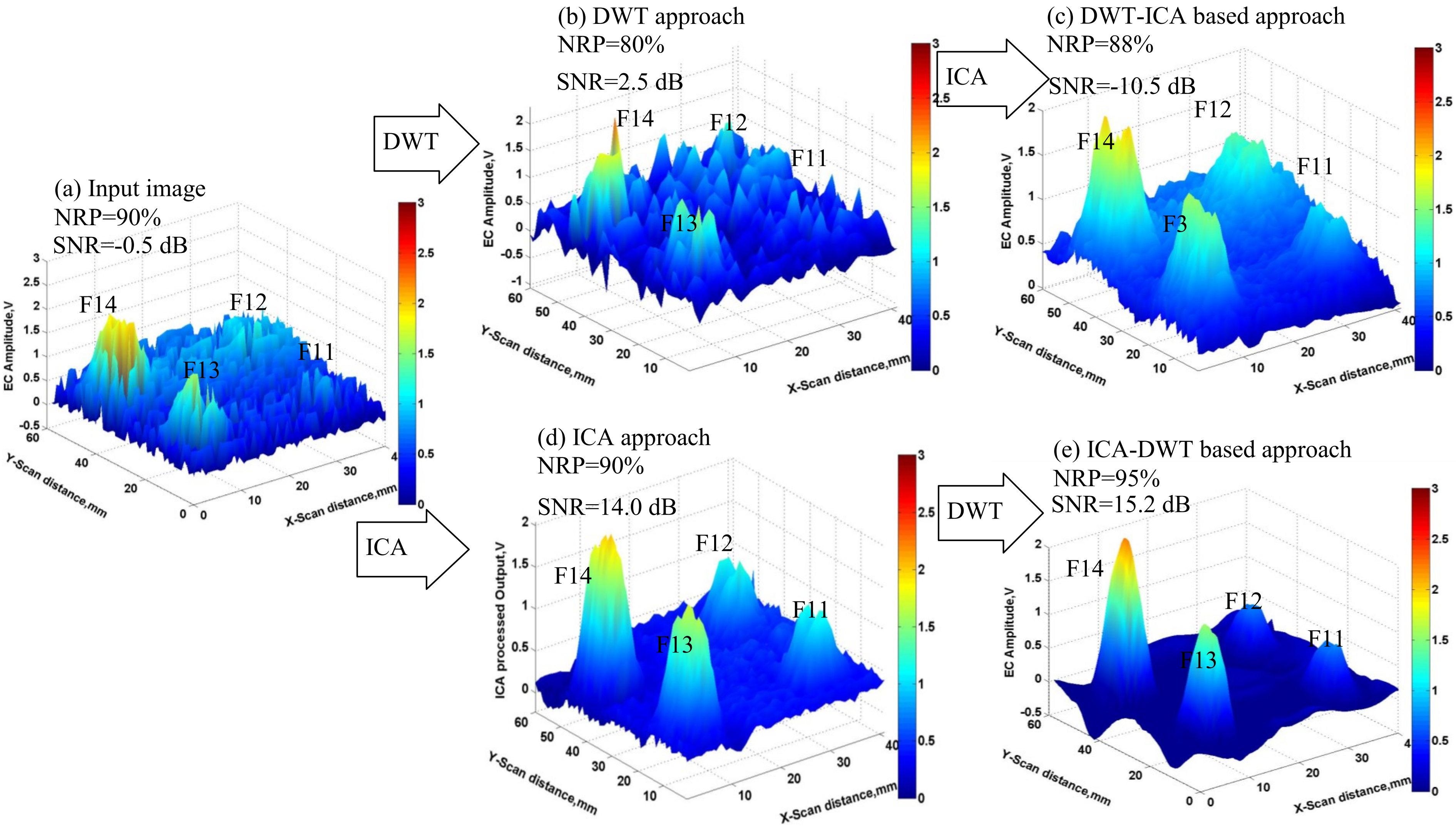

Figure 6.3 EC image of (a) four flaws (F11, F12, F13 and F14) in a plate (B4), with noise due to variations in lift-off, (b) and (c) output images from each stage of the hybrid DWT-ICA based approach and (d) and (e) from each stage of the hybrid ICA-DWT based approach.

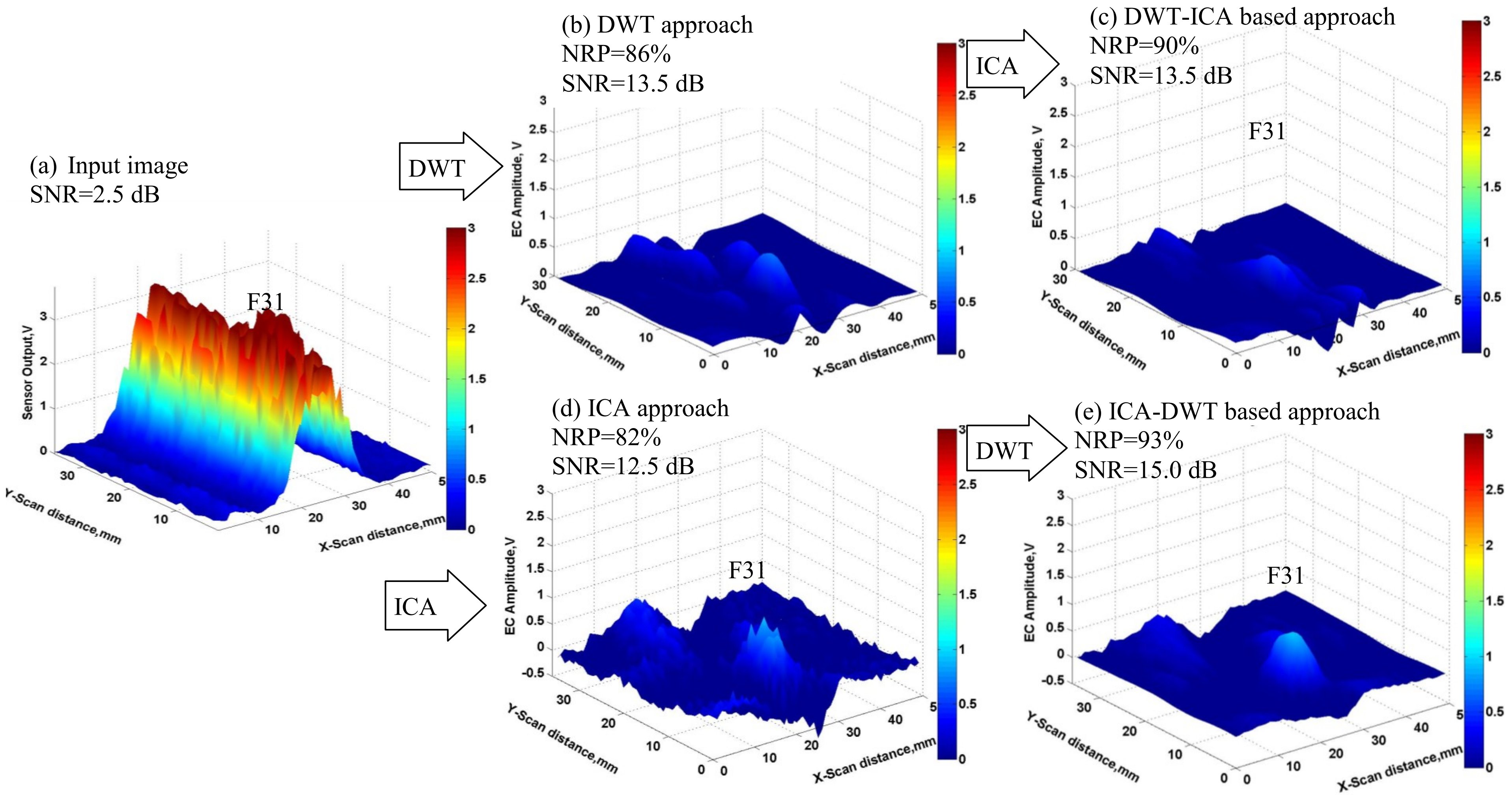

Figure 6.4 EC image of (a) flaw (F31) in a weld plate (W2) with composite noise, (b) and (c) output images from each stage of the hybrid DWT-ICA based approach, (d) and (e) from each stage of the hybrid ICA-DWT based approach.

The performance of these approaches has been evaluated on several images having noise from single source and composite noise. The estimated NRP, SNR, Flaw amplitude are given in Table 6.1. A significant improvement in noise reduction as well as flaw retention ability is observed by the ICA-DWT based approach as compared to the DWT-ICA based approach.

Table 6.1 Performance evaluation of hybrid DWT-ICA and hybrid ICA-DWT based approach on experimental images.

No.	Flaw No.	Input image SNR, dB	Denoised image					
			DWT-ICA based approach			ICA-DWT based approach		
			NRP, %	SNR, dB	Flaw amplitude, V	NRP, %	SNR, dB	Flaw amplitude, V
B1	F1	6.8	90	13.2	0.3	93	14.2	0.3
	F2	7.2		14.1	0.5		14.1	0.5
	F3	6.5	88	13.5	0.75	92	15.5	1.0
	F4	8.5		13.5	1.1		15.5	1.4
B2	F5	6.2	88	13.9	1.1	93	15.9	1.4
	F6	7.0	90	14.2	0.9	93	15.2	1.0
B3	F7	6.2	92	14.5	0.45	92	14.5	0.5
	F8	7.5		14.0	1.2		15.0	1.4
	F9	7.0	90	13.8	1.0	93	14.8	1.0
	F10	8.0		14.5	1.1		14.5	1.4
B4	F11	4.5	88	14.0	0.3	92	14.0	0.3
	F12	5.2		14.0	0.46		14.0	0.5
	F13	6.2		14.0	0.9		14.5	1.0
	F14	8.5	89	15.2	1.7	93	15.2	1.8
	F15	7.5		15.5	1.3		15.5	1.4
	F16	9.2		16.5	2.0		16.5	2.4
	F17	5.5		13.3	0.42		14.3	0.5
	F18	7.5		14.5	1.3		14.5	1.4
	F19	9.2		14.0	2.2		15.0	2.4
W1	F26	4.0	86	12.8	0.13	90	14.0	0.2
	F27	4.2	88	13.2	0.22	92	14.0	0.3
	F28	4.8	89	13.8	0.4	93	14.5	0.5
	F29	4.8	90	14.0	0.4	92	14.6	0.5
	F30	5.5	90	14.2	1.0	93	15.0	1.4
W2	F31	4.5	88	13.8	0.4	92	14.5	0.5
	F32	5.5	90	14.5	2.0	92	15.2	2.4
	F33	4.2	87	13.5	0.22	92	15.0	0.3
	F34	4.5	88	14.0	0.4		14.5	0.5
	F35	4.8	90	14.5	0.52		14.8	0.65

The ICA based approach has shown SNR of 12.5 dB and NRP of 82%, the DWT based approach has shown SNR of 10.0 dB and NRP of 75% and hybrid ICA-DWT based approach has shown SNR of 15.0 dB and NRP of 93%. It is noted that hybrid ICA-DWT based approach has enhanced the SNR by 2.5 dB and NRP by 11%.

The difference point between ICA-DWT and ICA approach are that ICA is processed the image through mixing matrix with the help of statistical independence of sources and do not estimate frequency dependencies. In the ICA-DWT based approach, ICA separates most of the noise and passes the data that contains information about Gaussianity to the DWT approach. ICA exploits the inherent non-linearity in the separation of components with mutual statistical independence. ICA maps the information from the R^{PxQ} domain (where P, Q are pixels along the width and height of source images) into a co-domain where information is split into sub-information by minimising the mutual information. The removal of mutual information reduces multi-scale dependency among the wavelet coefficients in the DWT processing and thus resulting in better localization of the flaw information. The marked advantages of the ICA-DWT based approach are a) better noise reduction ability and b) better flaw retention ability. Thus, the hybrid ICA-DWT based approach is a more efficient approach for noise reduction in EC images.

6.3 Performance of the proposed hybrid ICA-DWT based approach

6.3.1 Evaluation of noise tolerance: Noise from single source

The noise tolerance of the proposed hybrid ICA-DWT based approach for higher amount of noise from variations in lift-off ≥ 1.0 mm (0.0 mm to 1.5 mm, 0.0 mm to 2.0 mm) is evaluated on number of EC images. The input images of a flaw (F5, length 20.0 mm, width 0.5 mm, depth 1.0 mm) in a plate B2 acquired with variations in lift-off (0.0 mm to

1.5 mm, 0.0 mm to 2.0 mm) and the output of proposed hybrid ICA-DWT based approach are shown in Figure 6.5. As can be seen from Figure 6.5, the proposed hybrid ICA-DWT based approach is able to remove noise well while retaining flaw information even in the presence of higher variations in lift-off noise (≤ 2.0 mm).

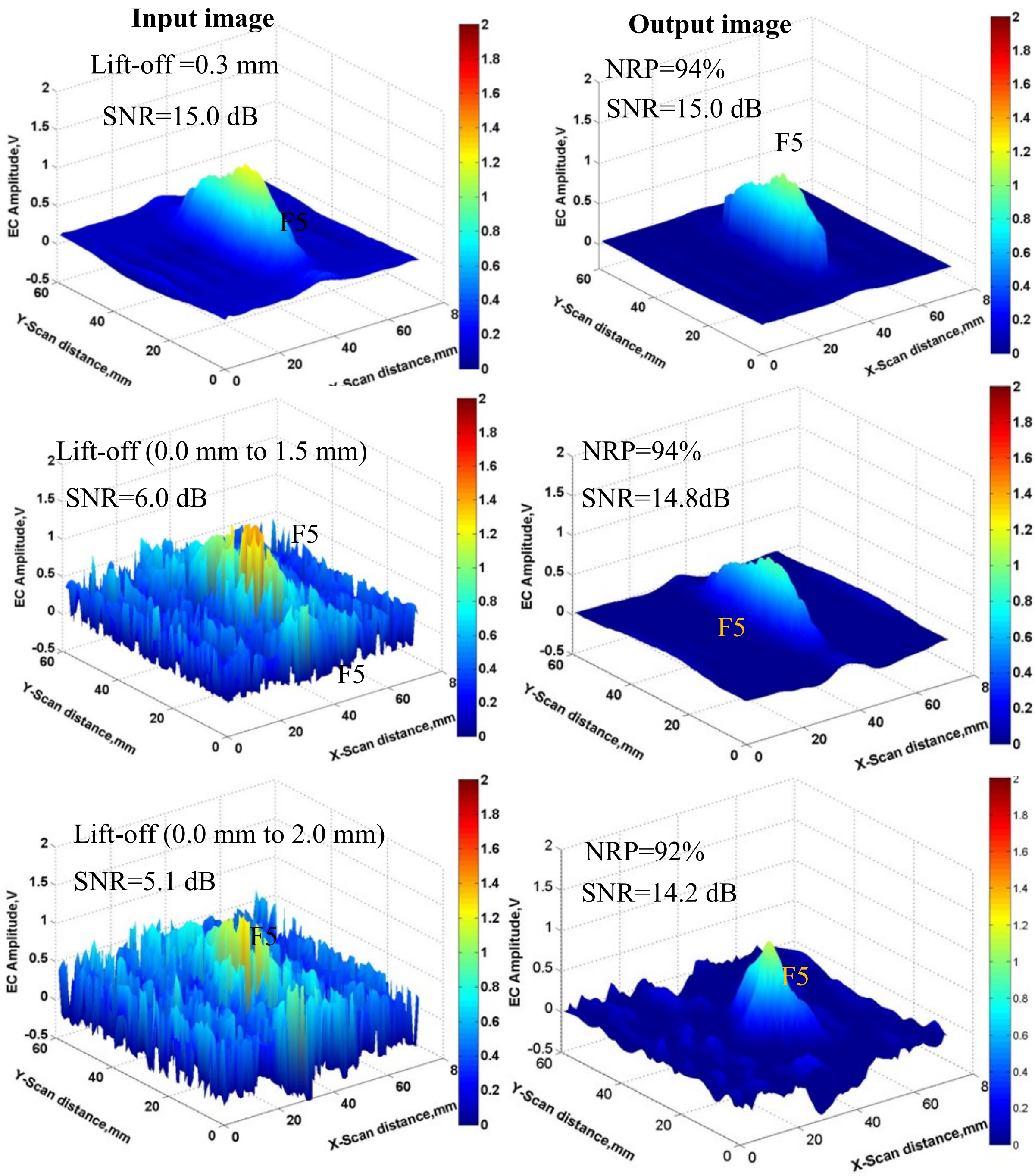

Figure 6.5 Performance of the hybrid ICA-DWT based approach for variations in lift-off.

6.3.2 *Evaluation of noise tolerance: composite noise*

The noise tolerance of the proposed hybrid ICA-DWT based approach has also been evaluated for EC images of weld plates acquired with variations in lift-off (0.0 mm to 1.5 mm, 0.0 mm to 2.0 mm). Figure 6.6 shows typical EC images of a flaw (F28, length 4.0 mm, width 0.25 mm, depth 0.5 mm) in a weld plate (W1) acquired with variations in lift-off and their corresponding output of the hybrid ICA-DWT based approach. The estimated NRP, SNR and flaw amplitude of the processed images are given in Table 6.2.

Table 6.2 Evaluation of the proposed hybrid ICA-DWT based approach for variations in lift-off.

Plate No.	**Flaw No.**	**Variations in lift-off, mm**	**Input image SNR, dB**	**Denoised image**			
				NRP, %	**SNR, dB**	**Flaw amplitude, V**	**FRP, %**
B1	F1	≤0.5	8.0	93	15.0	0.5	0
		≤1.0	6.8	92	14.2	0.5	0
		≤1.5	5.0	90	13.6	0.5	0
		≤2.0	4.5	88	13.2	0.5	0
B2	F5	≤0.5	10.0	94	15.0	1.0	0
		≤1.0	7.9	94	14.8	1.0	0
		≤1.5	6.0	94	14.8	1.0	0
		≤2.0	5.1	92	14.6	0.98	2
B3	F8	≤0.5	10.0	93	15.0	1.4	0
		≤1.0	7.5	90	14.8	1.4	0
		≤1.5	7.2	90	15.0	1.38	1
		≤2.0	6.2	86	14.5	1.35	3
B4	F15	≤0.5	9.5	92	15.2	1.4	0
		≤1.0	8.2	90	15.0	1.4	0
		≤1.5	7.5	90	14.2	1.37	2
		≤2.0	6.0	85	14.0	1.33	5
W1	F28	≤0.5	8.0	94	15.0	0.5	0
		≤1.0	4.8	94	15.0	0.5	0
		≤1.5	3.0	94	14.8	0.5	0
		≤2.0	-0.5	92	14.0	0.48	4
W2	F31	≤0.5	7.8	94	15.0	0.5	0
		≤1.0	4.5	92	15.0	0.5	0
		≤1.5	3.2	92	14.6	0.5	0
		≤2.0	-1.0	90	14.2	0.47	5

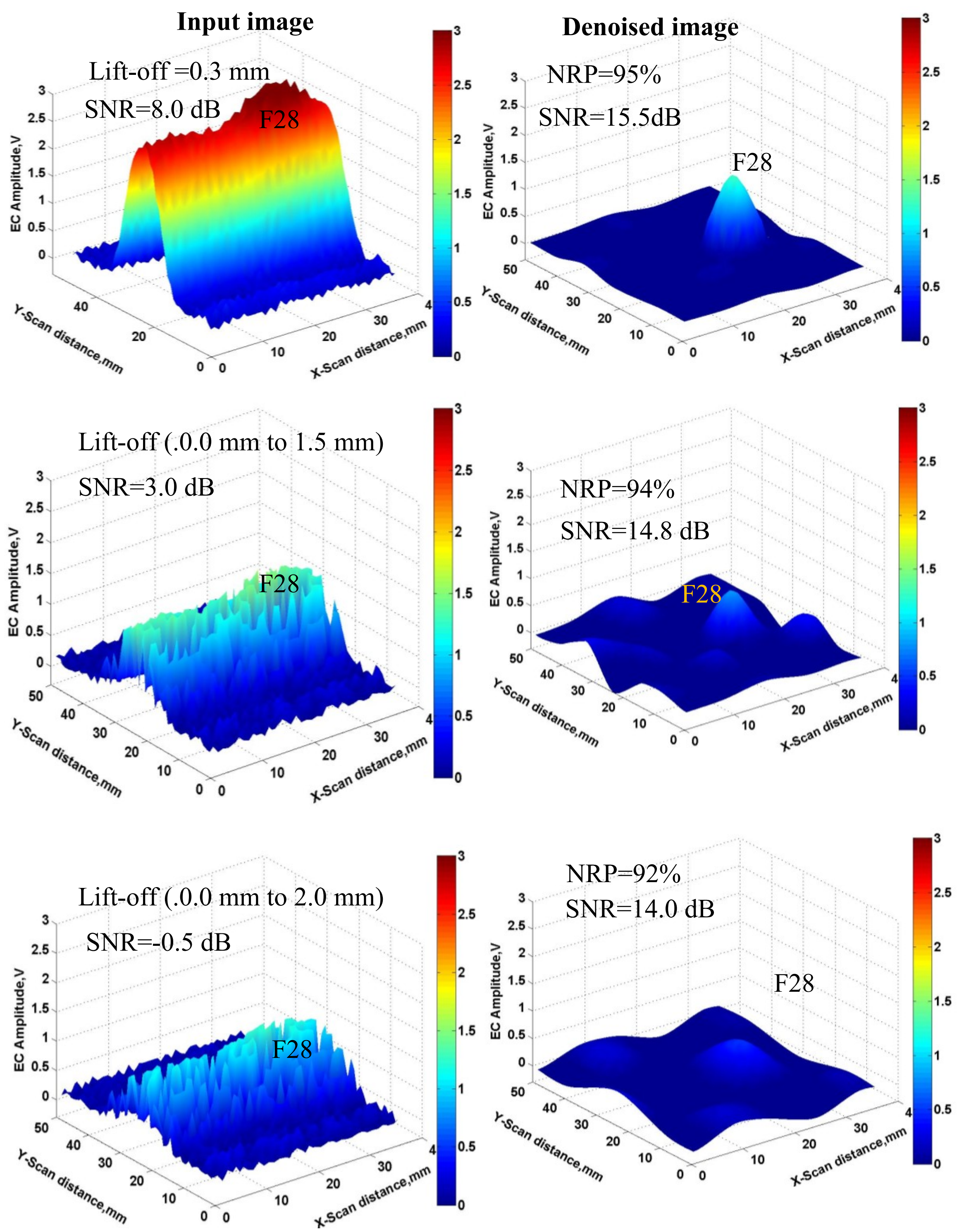

Figure 6.6 Performance of the hybrid ICA-DWT based approach for variations in composite noise.

Figure 6.7 and Figure 6.8 depict the comparative performance in NRP, SNR of the individual processing DWT, ICA and hybrid approaches for single source of noise and composite noise respectively. As can be seen, the proposed hybrid ICA-DWT based approach enhanced the noise reduction and improved the SNR. In addition, the capability of flaw retention indicates its tolerance to the higher amount of noise as compared to the individual DWT and ICA based approaches.

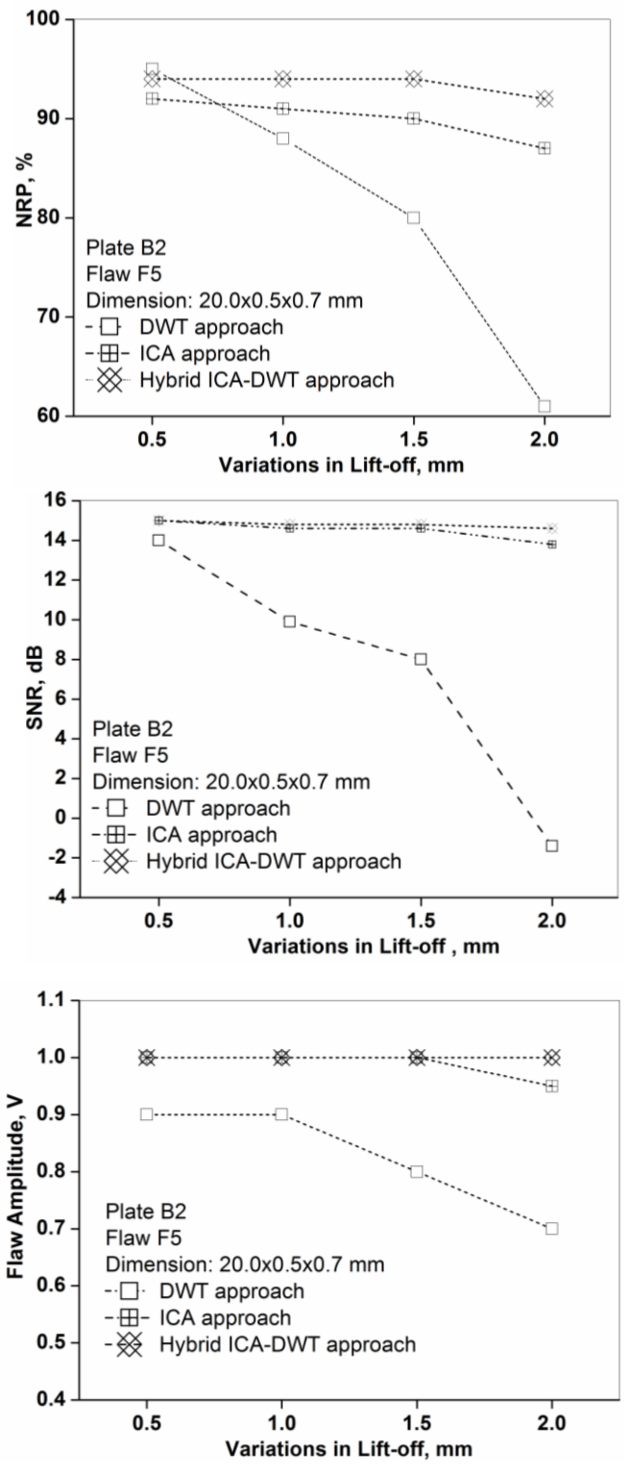

Figure 6.7 Denoising ability of hybrid ICA-DWT based approach for variations in lift-off.

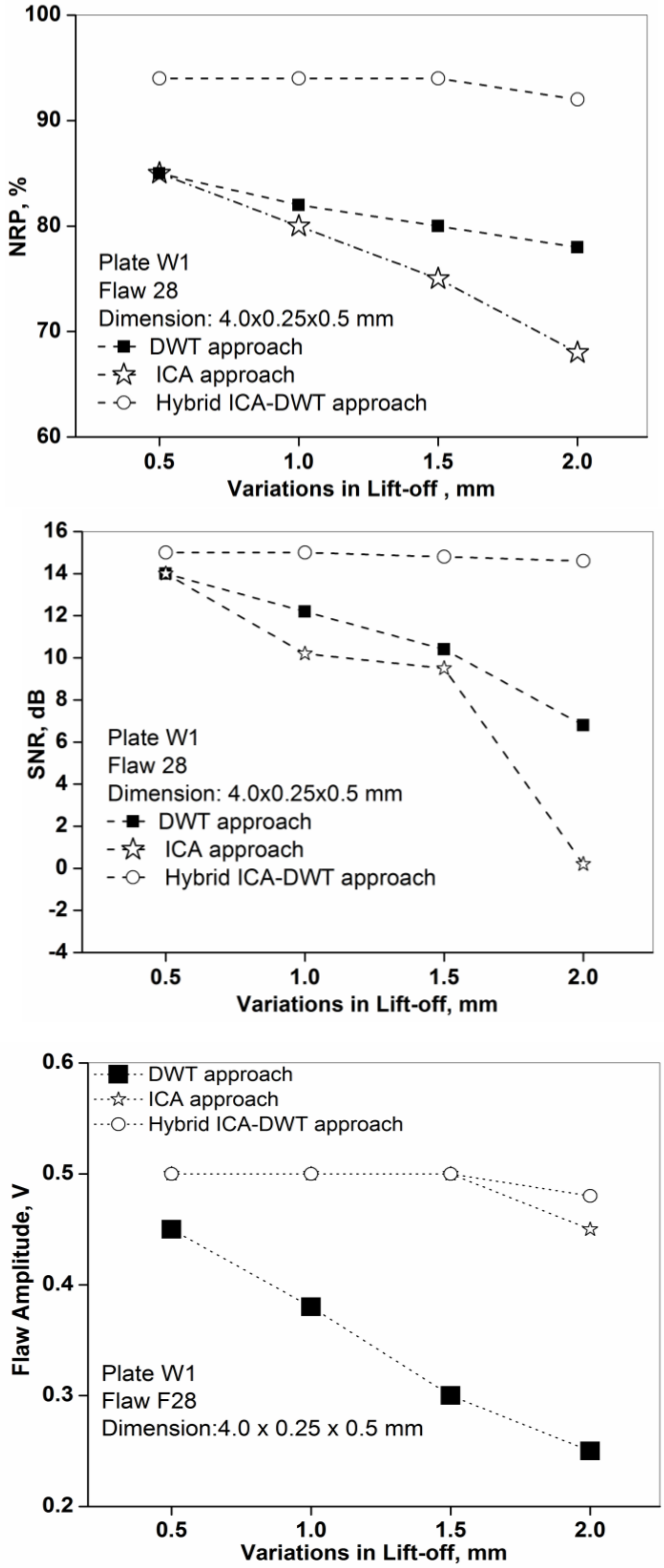

Figure 6.8 Denoising ability of hybrid ICA-DWT based approach for variations in composite noise.

The proposed hybrid ICA-DWT based approach exhibits the improved denoising capability for single source noise (lift-off noise) as well as composite noise up to the range of ≤ 2.0 mm variations in lift-off as compared with individual ICA based approach and DWT based approach. The amplitude of the flaw has been retained even in the presence of lift-off variations up to 2.0 mm.

6.3.3 Influence of test parameters

The influence of testing frequency and diameter of the EC probe on denoising ability of the proposed hybrid ICA-DWT based approach is evaluated. The several EC images of plates (B1, B2, B3) and weld plates (W1, W2) acquired using probes of 5.0 mm and 20.0 mm diameter at testing frequencies of 75 kHz and 20 kHz are processed.

6.3.3.1 Influence of test frequency and probe diameter

EC images acquired from plate (B4) and weld plate(W2) using 5.0 mm diameter EC probe at 75 kHz frequency have been used. The EC image of a plate (B4) having flaws F11 to F19 (F11-F1:length 8.0 mm, width 0.3 mm, depth 0.3 mm, 0.5 mm, 0.7 mm, F15-F16, length 8.0 mm, width 0.3mm, depth 1.0 mm, 2.0 mm, F17-F19, length 8.0 mm, width 0.5 mm, depth 0.5 mm, 1.0 mm, 2.0 mm), among them four of them are buried in noise due to lift-off variations as shown in Figure 6.9 (a). The processed image from the ICA approach and sub decomposition of flaw image using the DWT approaches are shown in Figure 6.9 (b) and Figure 6.9 (c). The NRP of 85% is achieved by the ICA approach and sub decomposition of the flaw component by the DWT approach enhanced the NRP to 92%. These results show similar denoising performance and observe no influence of testing parameters viz. varying diameter of 3.0, 5.0, 20.0 mm and frequencies of 20 kHz, 75 kHz and 150 kHz.

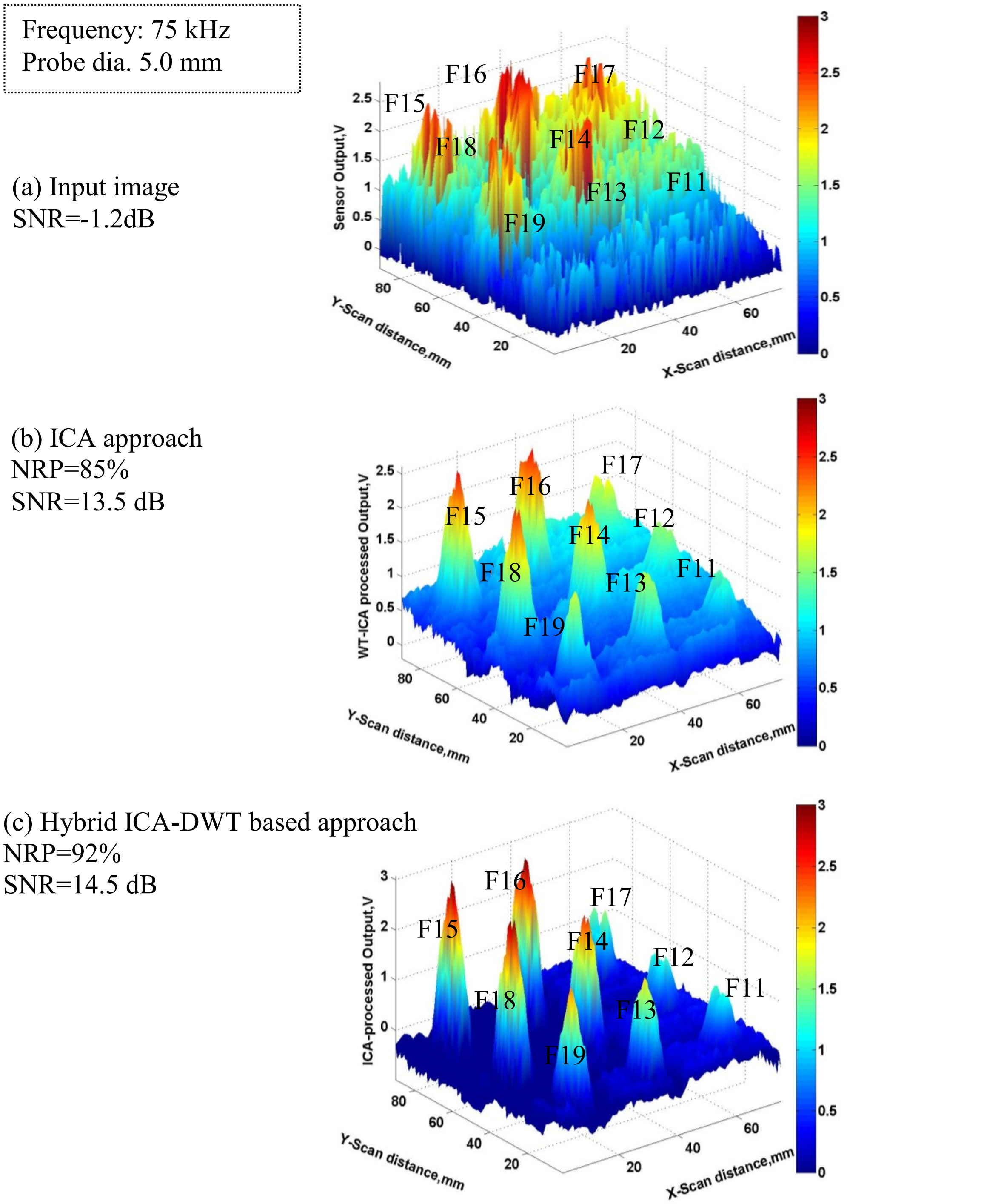

Figure 6.9 EC image of (a) nine flaws (F11-F19) in a plate (B4), output images from (b) ICA approach and (c) proposed hybrid ICA-DWT based approach.

The denoising performance of the proposed hybrid approach for removal of composite noise at different test parameter (test frequency75 kHz, 5.0 mm diameter probe) has been evaluated. The EC image of three flaws (F33, F34 and F35) depths of 0.3, 0.5 and 0.6 mm in a weld plate (W2) buried in composite noise has been tested. The input image and output image from the each stage of the approach are shown in Figure 6.10.

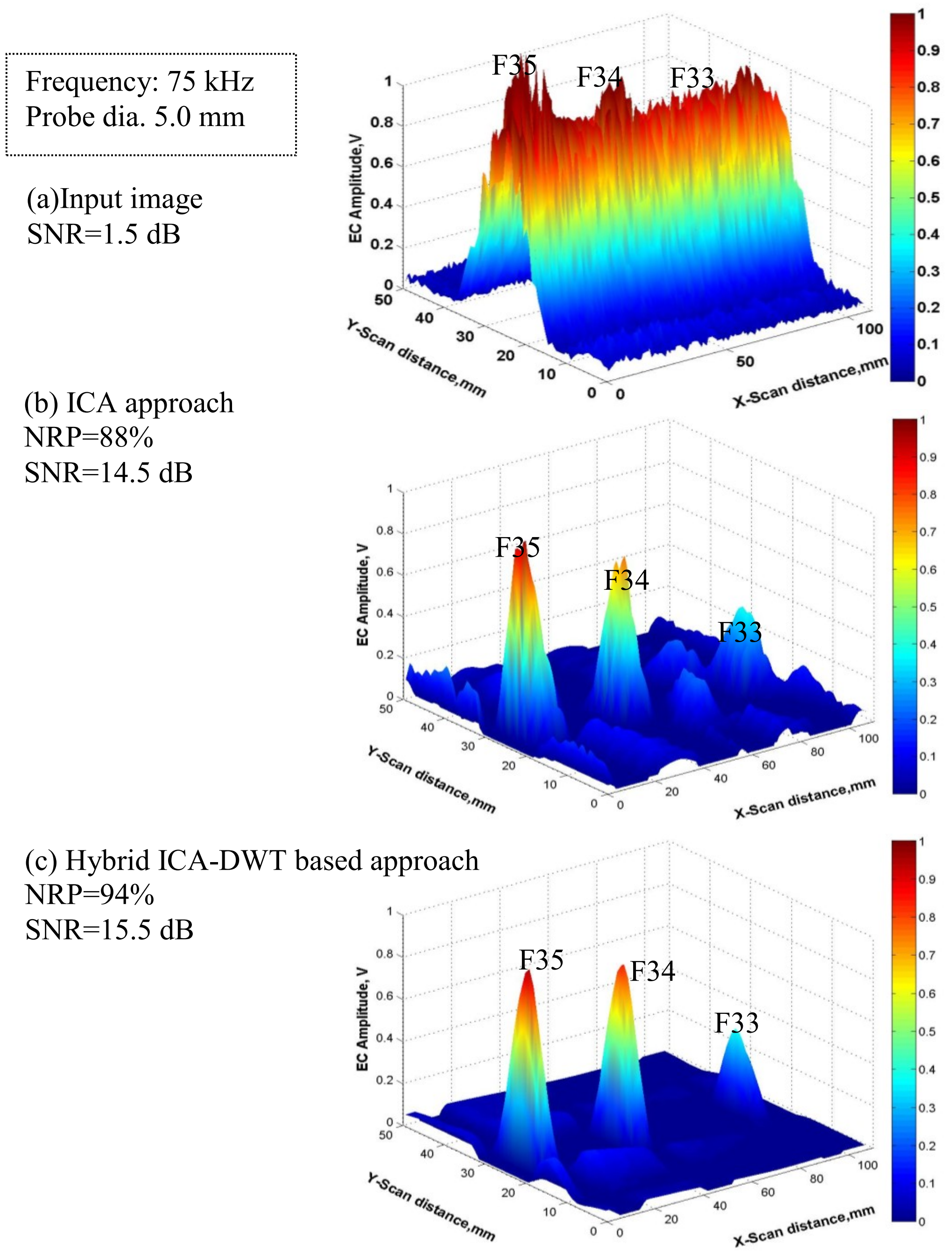

Figure 6.10 EC image of (a) thee flaws (F33-F35), output images from (b) ICA approach and (c) proposed hybrid ICA-DWT based approach.

Similar performance has been achieved with NRP of 88% from the ICA approach and subsequent DWT enhances NRP to 94% and establishes its noise reduction capability.

From these results, it is observed that no significant influence of testing parameters (varying diameter of 3.0, 5.0, 20.0 mm and frequencies of 20 kHz, 75 kHz and 150 kHz) on the performance of the ICA approach.

6.3.4 Influence of noise due to variations in electrical conductivity

The performance of the proposed hybrid ICA-DWT approach has also been evaluated for removal of noise due to gradual variations in electrical conductivity. EC image of a flaw (length 6.0 mm, width 0.3 mm and depth 0.5 mm) in the plate with noise is processed and results from each stage of the proposed hybrid ICA-DWT approach are shown in Figure 6.11. The NRP of 90%, SNR of 14.5 dB, consistent flaw retention ability are observed in the processed image.

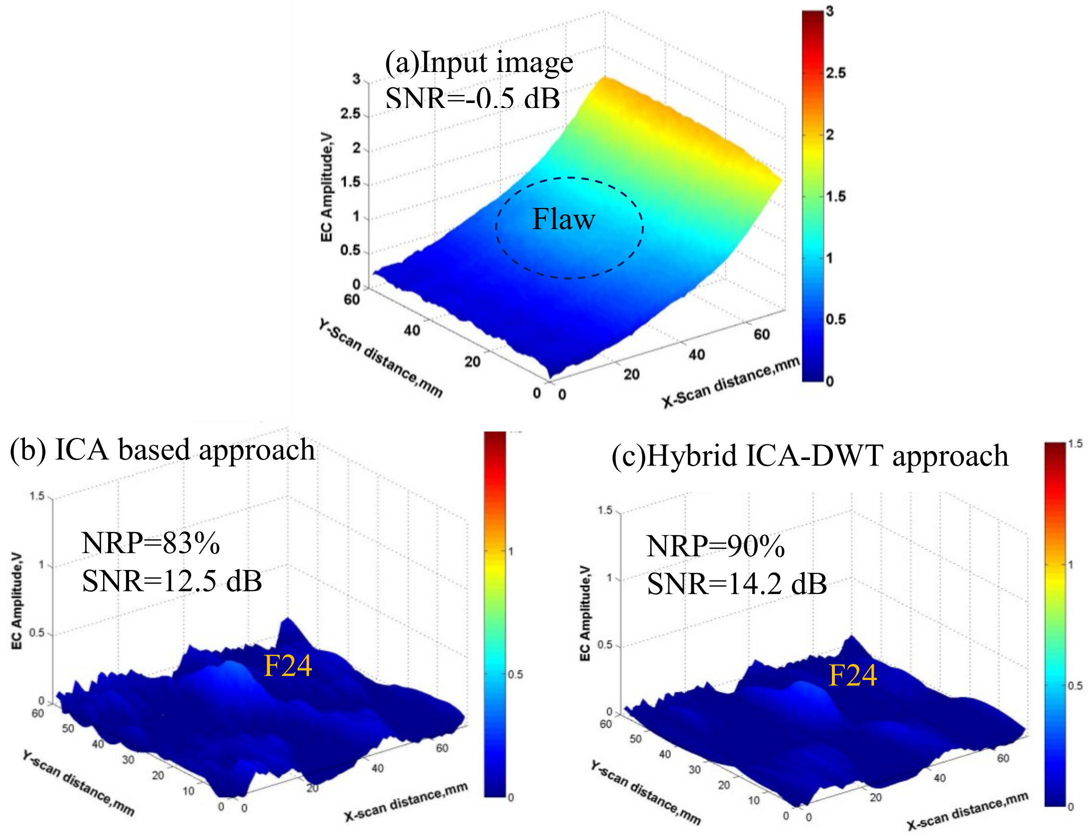

Figure 6.11 Denoising capability of the proposed hybrid ICA-DWT based approach for noise due to variations in electrical conductivity.

6.3.5 Influence of noise due to geometrical variations

The denoising ability of the proposed hybrid ICA-DWT based approach for removal of noise from geometrical variations has been evaluated. AISI type 316 SS tube of 5.1 mm outer diameter and 0.37 mm wall thickness having periodic wall thickness variations of the order of 10 to 20 microns (2.6% to 5.2 % wall thickness) is tested using surface absolute probe of 3.0 mm diameter at test frequencies of 350 kHz (δ=0.7 mm) and 750 kHz (δ=0.49 mm). EC images of flaws are of longitudinal notches (length 4.0 mm, width 0.1 mm, and depth 0.075 mm, 0.15 mm) and circumferential notches (length 4.0 mm, width 0.1 mm, depth 0.075, 0.15 mm) are processed by the proposed hybrid approach.

Two cases of noise a) single source of noise due to wall thickness variations and b) composite noise due to wall thickness and lift-off variations are considered. Figure 6.12 (a) shows the EC image of a flaw (F39-length 4.0 mm, width 0.1 mm, depth 0.075 mm) in a tube (T2) having wall thickness variations.

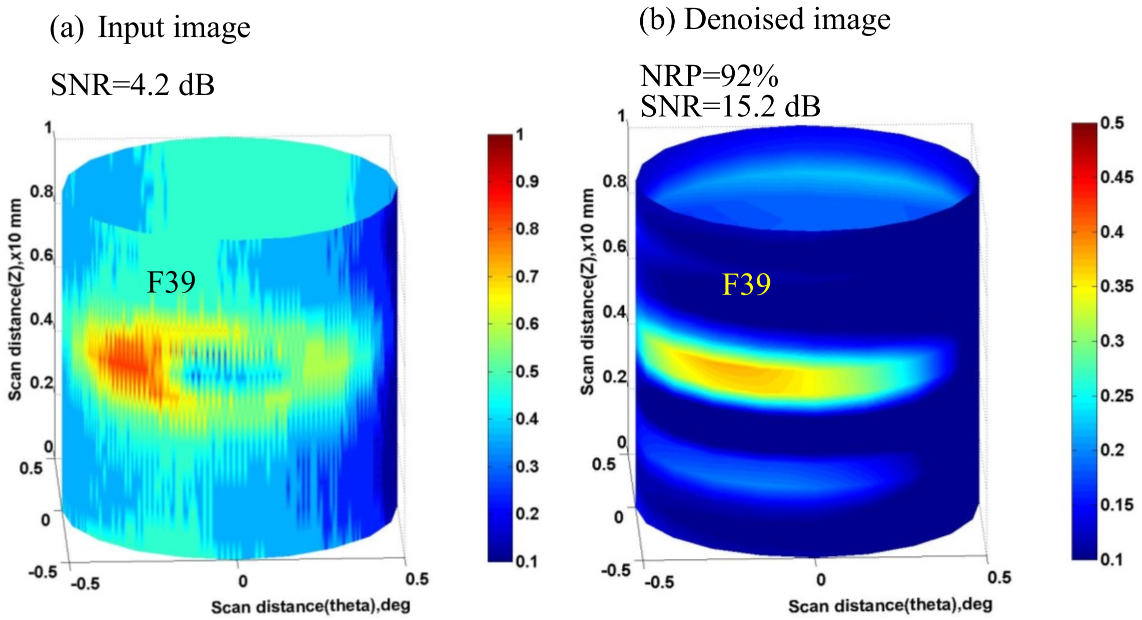

Figure 6.12 EC image of (a) flaw (F39, circumferential notch) in a tube T2 with noise due to wall thickness variations (single source of noise), (b) output image from the proposed hybrid ICA-DWT based approach.

The processed output image from proposed hybrid ICA-DWT based approach is shown in Figure 6.12 (b). NRP, SNR and flaw amplitude are found to be 92%, 15.2 dB and 0.38 V respectively. The proposed hybrid ICA-DWT based approach is also evaluated for removal of composite noise (due to wall thickness variations and variations in lift-off (0.0 mm to 1.0 mm) in an EC image of a flaw (F40- length 4.0 mm, width 0.1 mm, depth 0.15

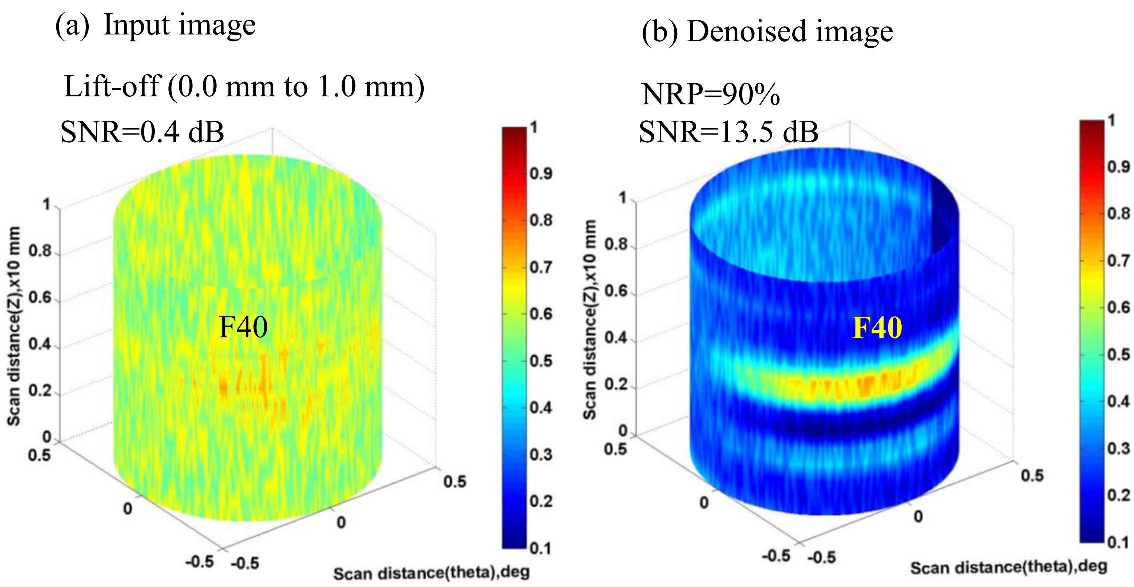

Figure 6.13 EC image of (a) a flaw (F40, circumferential notch) in a tube T2 with composite noise and (b) output image from proposed hybrid ICA-DWT based approach.

mm) and the results are shown in Figure 6.13. NRP, SNR and flaw amplitude are found to be 90% , 13.5 dB and 0.72 V respectively.

6.3.6 Application to sub-surface flaw detection

Based on these promising results for surface flaws, the applicability of the proposed ICA-DWT approach is extended to detection of sub-surface flaws. EC image of SS plate (B5) having sub-surface flaws (F20-F25, length 6.0 mm, width 0.3 mm) located at 1.0 mm, 2.0 mm, 3.0 mm, 3.5 mm, 4.0 mm and 4.5 mm below the surface is processed. EC image acquired at a 20 kHz (δ=4.0 mm) using 20.0 mm diameter probe (>length of flaw) and the results are shown in Figure 6.14. The result shown in Figure 6.14 demonstrates the noise reduction as well as flaw enhancement capabilities of this approach for sub-surface flaws with an improvement in NRP of 90% and SNR of 14.5 dB. These results clearly bring out an interesting observation that the performance of the proposed approach has not significantly been altered by the test frequency and the probe diameter. This result indicates the applicability of this approach to sub-surface flaw enhancement.

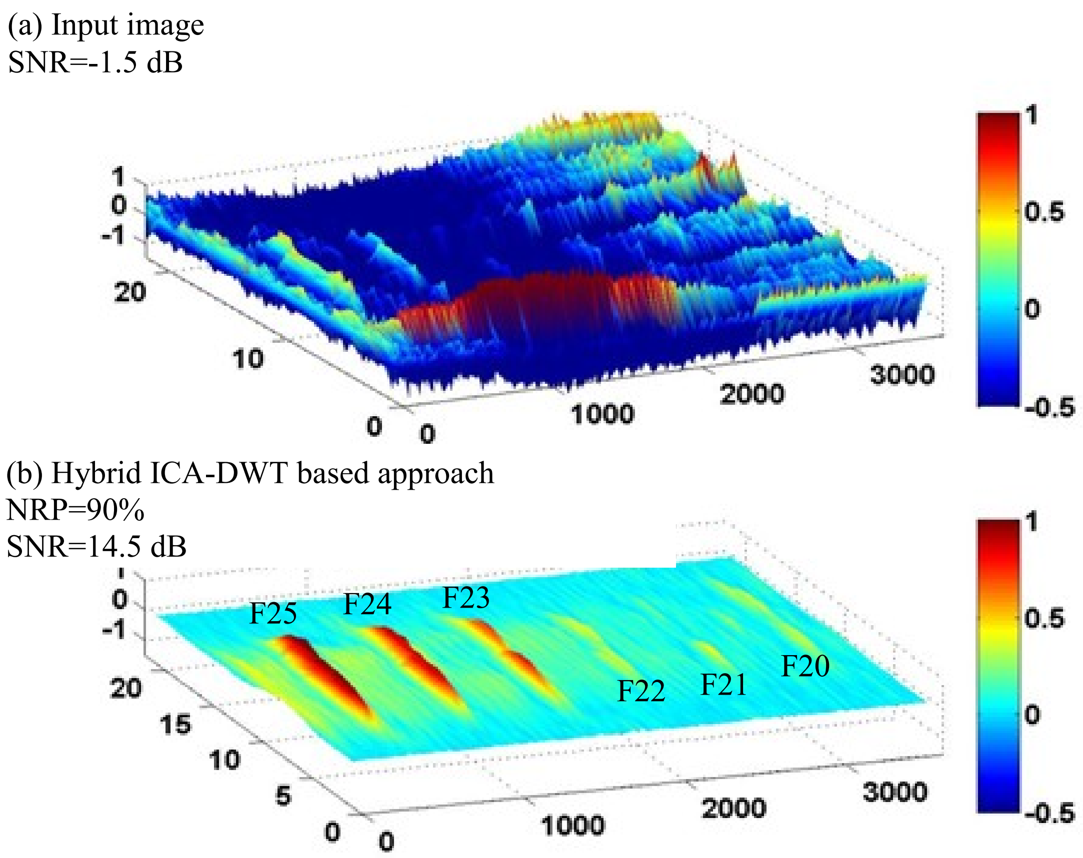

Figure 6.14 EC image of (a) sub-surface flaws (F20-F25) and (b) the output image from hybrid ICA-DWT based approach.

6.3.7 Application to surface flaw detection

Figure 6.15 (a) shows the EC image of surface flaws of length 6.0 mm (width 0.3 mm, depths 0.5 mm, 0.7 mm, 1.0 mm, 1.5 mm, 2.0 mm, 2.5 mm) having relatively limited information of the shallow flaws. The reduced sensitivity is due to the large diameter (20.0 mm) of the probe, which is 3 times greater than the length of the flaw. Figure 6.15 (b) shows the output image from hybrid ICA-DWT based approach. The processed image shows SNR of 14.5 dB. The approach has detected all the shallow flaws and this proves its efficacy for denoising as well as flaw enhancement capability.

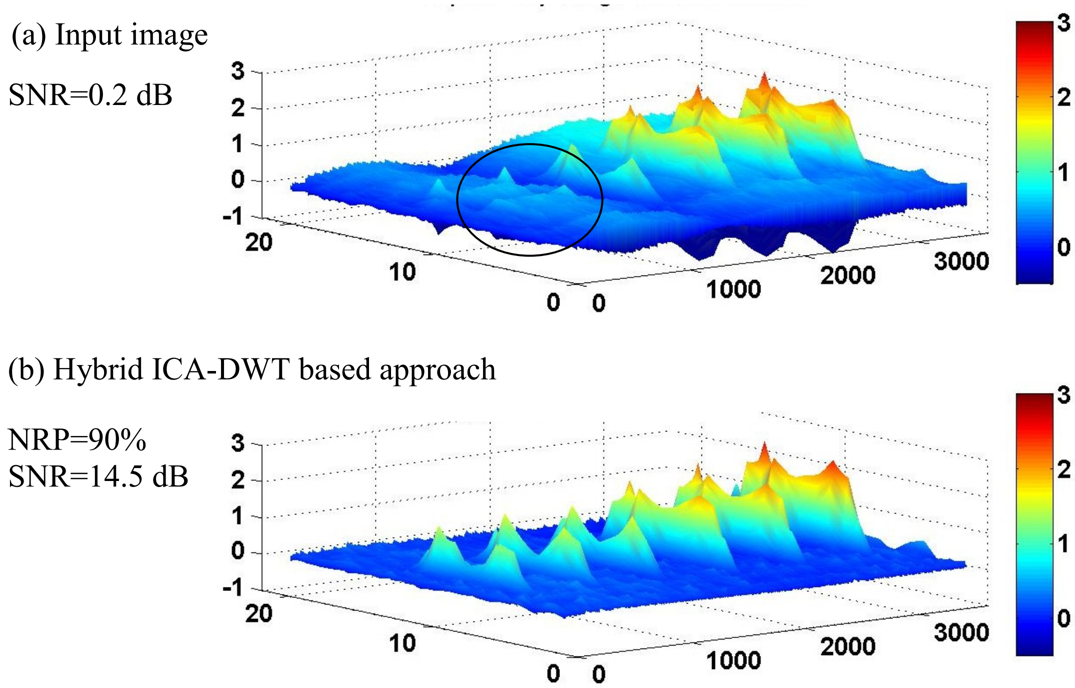

Figure 6.15 Output of the ICA-DWT approach for imaging of surface flaws by a large diameter probe.

6.3.8 Application to natural flaw detection

The proposed approaches have demonstrated better noise removal and improved flaw detectability for machined flaws. To evaluate the performance of the proposed approaches for a realistic flaw, an EC image of a fatigue crack in a SS plate (shown in Figure 6.16) has been processed. Figure 6.16 shows an EC image of the fatigue crack (length 12.0 mm, width 0.1mm) acquired at 150 kHz using a 3.0 mm diameter probe. Figure 6.16 also shows the denoising performance of the DWT, ICA and hybrid ICA-DWT based approaches.

In the DWT approach, wavelet filter Db5, level 5 has been identified as an optimum wavelet, same as that for plates with machined flaws. This promises its capability for

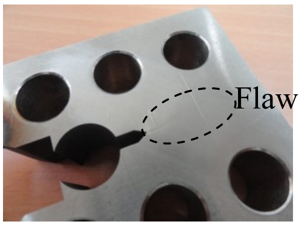

(a) Input image

SNR=10.2 dB

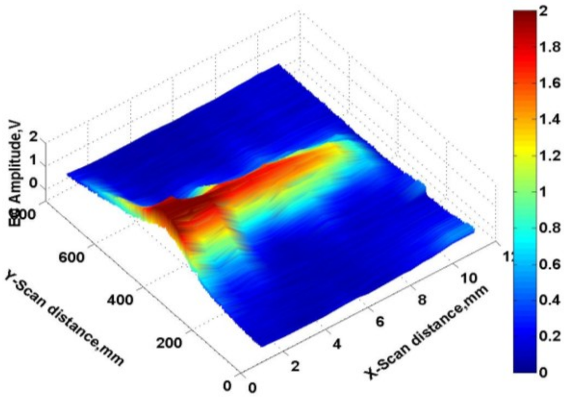

(b)DWT based approach
NRP=92%
SNR=13.5 dB

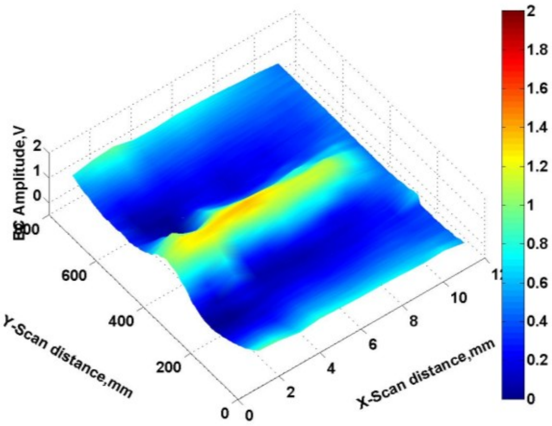

(c) ICA based approach
NRP=92%
SNR=13.5 dB

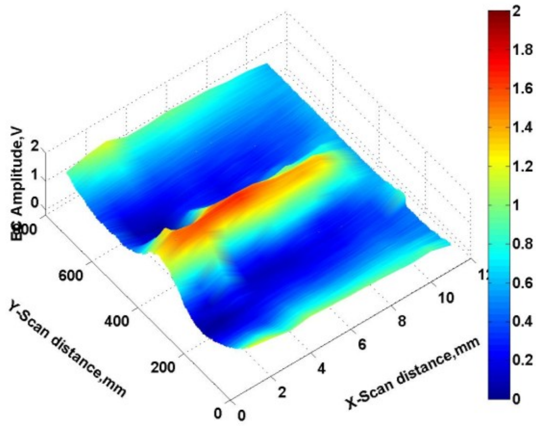

(d) Hybrid ICA-DWT based approach
NRP=94%
SNR=15.5 dB

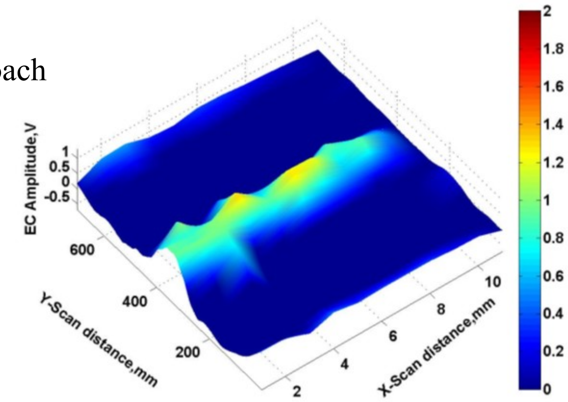

Figure 6.16 EC image of (a) a fatigue crack in a SS plate, processed images from (b) DWT approach, (c) ICA approach and (d) hybrid ICA-DWT based approach.

reliable selection of wavelet filter. The individual DWT and ICA based approaches have shown improvement in NRP of 92%, SNR of 13.5 dB. The hybrid ICA-DWT based approach has been improved the NRP to 94% and SNR to 15.5 dB. This confirms the proposed hybrid ICA-DWT approach is useful for denoising EC images of natural cracks.

6.4 Summary

After the study on denoising ability of the proposed DWT based approach and ICA based approach using NRP, SNR, and flaw amplitude, the possible two sequences, i.e., DWT-ICA and ICA-DWT have been investigated in detail. The observed results are the following:

- ICA-DWT based approach is a better approach with a significant improvement in NRP of 93% and SNR of 15.0 dB
- The proposed hybrid ICA-DWT approach achieved a NRP of 95% and SNR of 15.5 dB in the presence of composite noise, which is three times the SNR of the input images (4.5 dB).
- The proposed ICA-DWT approach improves the flaw retention ability and establishes its noise tolerance up to the variations in lift-off 0.0 mm to 2.0 mm for single source of noise and up to the variations in lift-off 0.0 mm to 1.5 mm for composite noise.
- No influence on denoising and flaw retention ability of the proposed hybrid ICA-DWT approach for varying test frequencies in the range of 20 kHz-150 kHz and probes of 3.0 mm, 5.0 mm and 20.0 mm is observed.
- The approach could enhance the detection of shallows flaws (depth 0.2 mm <10% wall thickness) of comparable amplitude with that of noise.

- The denoising capability of the hybrid approach has been successfully validated on the influence of composite noise a) due to lift-off and wall thickness variations (geometrical variations) in thin wall SS tubes and also b) noise due to gradual variation in electrical conductivity along the SS plate.
- The hybrid ICA-DWT based approach proposed in this thesis has significantly enhanced the flaw detection sensitivity of surface flaws, sub-surface flaws and natural cracks in EC imaging NDE.

Chapter 7 : Conclusion and Future works

7.1 Conclusion

The thesis has proposed image processing approaches for denoising of eddy current images, influenced by variations in lift-off, variations in material properties and composite noise. Detailed investigations on the spectral characteristics of the flaw and statistical characteristics of noise have been carried out. These approaches have been evaluated for capability of noise removal and enhancement of flaw detection in eddy current images acquired from AISI type 316 stainless steel specimens. The major conclusions drawn from the thesis are the following:

The discrete wavelet transform (DWT) based approach has been proposed for automated selection of optimal wavelet filter through maximum energy criterion and optimal decomposition level through weighted risk factor as an entropy criterion. This automated selection overcomes the limitation of employing large number of reconstruction trials for selection of wavelet filters and decomposition level. The optimal wavelet filter is identified, for the first time, a wavelet filter Db5-level 5 for plates, wavelet filter Bior6.8-level 5 for weld plates and wavelet filter Bior1.1-level 10 for thin wall tubes. The proposed DWT based approach establishes the selective elimination through sub-band level Heursure thresholding method. With the optimum thresholding method, there is a significant improvement in SNR of 14. 5 dB and NRP of 92% (single source of noise) and SNR of 13.5 dB and NRP of 89% (composite noise) achieved.

It has been found from the experiments that denoising ability of the proposed DWT based approach is robust for EC images acquired at 20 kHz, 75 kHz and 150 kHz excitation frequencies and probes of 3.0 mm, 5.0 mm, 20.0 mm diameters. The flaw retention ability of the DWT based approach has been evaluated for higher variations in lift-off >1.5 mm using FRP. FRP is increased to 30% with higher reduction in amplitude as compared to the FRP of 10% at variations in lift-off <1.0 mm and thus establishes its noise tolerance up to the variations in lift-off ≤1.0 mm.

Exploiting statistical independence of the noise, Independent component Analysis (ICA) based approach has been proposed. The effectiveness of the noise removal is established through the proposed flexible universal rule which selectively uses nonlinear functions based on Kurtosis. The optimisation based on Kurtosis overcomes the limitation of the strong dependence of *pdf* of source signals as used in the conventional gradient rule.

Significant improvement in noise removal (93%) has been observed for a single source of noise than for the composite noise (80%). However, ICA based approach has shown promising performance for separation of flaw by retaining equal amplitude for identical flaws, despite variations in noise distribution. The flaw retention ability of the proposed approach establishes its noise tolerance up to the variations in lift-off 0.0 mm to 1.5 mm for single source of noise and for composite noise up to the variations in lift-off 0.0 mm to 1.0 mm. It has been found from the experiments that the varying test frequencies in the range of 20 kHz-150 kHz and probes of 3.0 mm, 5.0 mm and 20.0 mm have no significant influence on the denoising ability of the ICA based approach. The approach could detect shallows flaws (depth 0.2 mm <10% wall thickness) of comparable amplitude with that of noise.

From the study, it is identified that, the statistical dependency (Gaussianity) between some of the noise data limits the noise removal. To overcome the limitation, hybrid image processing approaches have been studied by combining the advantage of the noise reduction ability of the DWT based approach and flaw retention ability of the ICA based approach. In the optimal sequence of ICA based approach followed by DWT, the statistical dependency (Gaussianity) of the noise data and has been separated by subsequent decomposition of ICA components by a narrow band filtering for the first time, using DWT based approach. The proposed hybrid ICA-DWT based approach achieves significant improvement in NRP of 95% and SNR of 15.5 dB. The proposed ICA-DWT approach has improved the flaw retention ability and established its noise tolerance up to the variations in lift-off 0.0 mm to 2.0 mm for single source of noise and for composite noise up to the variations in lift-off 0.0 mm to 1.5 mm. The approach could detect shallows flaws (depth 0.2 mm <10% wall thickness) of comparable amplitude with that of noise. The efficacy of the proposed hybrid ICA-DWT approach has been successfully demonstrated on i) subsurface flaws in thick SS plates, ii) thin wall SS tubes having periodic wall thickness variations and iii) natural fatigue crack.

Studies clearly establish that the proposed hybrid approach ensures significant noise reduction, enabling better sensitivity to detection of flaws in EC images. It has also provided better insight into the existence of statistical dependency between the flaw information and utilization of dependency for enhanced effective separation flaw information.

7.2 Technical and scientific contributions

The major contributions of this thesis are the following:

For automated removal of noise incorporating optimisation of wavelet filter through maximum energy as criterion and a weighted risk factor considering multi-scale dependency of flaw as an entropy criterion for optimisation of decomposition level has been proposed, for the first time. The optimal wavelet filter is identified for the first time, for plates wavelet filter Db5-level 5, for weld plates wavelet filter Bior6.8-level 5 and for thin wall tubes wavelet filter Bior1.1-level 10 is found optimum.

A semi local paradigm for wavelet thresholding has been established by incorporating sub-band level thresholding using Heursure thresholding method. There is a significant improvement in SNR of 14. 5 dB and NRP of 92% in the presence of single source of noise and for composite noise SNR of 13.5 dB and NRP of 89% is achieved. Power of proposed DWT based approach for successful handling of noise is achieved due to multiresolution capability of optimal wavelet and proposed thresholding method.

The statistical dependency of noise characteristics has been identified as a tool for effective separation of noise in EC images. The incorporation of optimal estimation of de-mixing matrix, involves selection of nonlinear function through Kurtosis has shown promising performance of flaw separation by retaining equal amplitude for identical flaws, despite variations in noise distribution.

The optimisation based on Kurtosis overcomes the limitation of the strong dependence on probability density function (pdf) of source signals as used in the conventional gradient rule.

The limitation of ICA denoising in the case of composite noise has been addressed by the proposed hybrid ICA-DWT based approach. In this approach, frequency dependency of flaws and statistical independence of noise is utilised to eliminate noise in EC image.

The proposed hybrid ICA-DWT approach achieved a NRP of 95% and SNR of 15.5 dB. The denoising and flaw retention ability has no influence on the varying test frequencies in the range of 20 kHz-150 kHz and probes of 3.0 mm, 5.0 mm and 20.0 mm.

Study brings out the new points that even in one material, wavelet filters are different and it gives caution to practitioner not to use a single wavelet filter for all test situations.

The proposed hybrid approach essentially aids the early detection of shallow flaws and can be used in field for in-service inspection of components. Such a faster and cost effective processing approach will be beneficial for the assessment of structural integrity to ensure safety for the working personal and common public, besides improving the plant availability factor and revenue.

7.3 Future works

The proposed image processing approaches demonstrated better noise removal and improved flaw enhancement in stainless steels. The applicability of the proposed hybrid ICA-DWT based approach has been tested on a fatigue crack in stainless steel plate. However, application of the proposed hybrid ICA-DWT based approach can be extended to cracks of varying orientations, width and depths.

The study has established optimal wavelet filters for plates, welds and tubes. However, reason behind the performance is worth investigating. Extending the study to transient state signals e.g. pulsed eddy current may give insight to the performance of the wavelet filters. Since it has high frequency components varying with time, effective denoising and better resolution may be possible.

The proposed energy criterion where 90% of E_{max} of wavelet coefficients and their corresponding wavelet filters are considered for wavelet filter optimisation. Further studies on selection of lower bound energy may be worth investigating to understand the process behind the performance.

The studies on the applicability of the proposed hybrid ICA-DWT based approach to EC images from components made of different electrical conductivity, magnetic permeability may be beneficial.

EC images from differential type probes, array probes having varying foot prints as compared to the surface absolute probe studied, is worth exploring as it may capture the real world situations having altogether different statistical and spatial frequency distribution of the data.

In this study, imaging by raster scanning of a single probe is attempted. However, array probes are being increasingly used for single line scan imaging purpose. Thus, applying this proposed approach to linear array probe images may be beneficial, as it enables rapid imaging.

The flaw enhancement capability of the proposed hybrid ICA-DWT based approach can be extended to detect embedded flaws and corrosion in a second and third layer of aircraft structures.

Sizing of flaws has not been attempted. However, the proposed hybrid approach can be used in conjunction with feature extraction algorithms as well as classification and sizing algorithms for sizing the flaws.

The present study uses Kurtosis as a measure of non-Gaussianity to optimise de-mixing matrix in ICA based approach. A comparative study on the optimisation of de-mixing matrix based on approximation of negentropy is worth exploring, as it may give a good comparison between the properties of two classical non-Gaussian measures viz. Kurtosis and negentropy.

It is possible to evolve guidelines for an automated noise removal for flaw detection by determining and using suitable thresholds. This requires extensive experimental studies on different materials and test conditions. Further, numerical modelling to generate data for this purpose is another possibility.

The discrimination between the various noise sources is not attempted in this thesis. The developed techniques appear capable, however, detailed experimental studies using wavelet packet analysis and fine tuning of decomposition level are necessary.

The application of the proposed image processing approaches may be extended to the imaging situations that are diffusion phenomenon based. One such technique is infrared thermography (IRT). The propagation of heat energy in a material is diffusive like the electromagnetic fields in EC testing. However, disturbing variables are different viz. reflectivity and emissivity. It may be worth studying the applicability of the proposed hybrid approach to IRT, especially, lock-in thermography.

The applicability of the proposed hybrid approach can be extended to other NDE images. The proposed optimal choice of non-linear functions for various noise distributions in other NDE images is worth exploring to enhance flaw detection.

Further, recent techniques such as ensemble empirical mode decomposition (EEMD) which uses adaptive intrinsic mode function may be attempted in place of DWT for further reduction in noise through adaptive analysis.

REFERENCES

[1] P. J. Shull, Nondestructive Evaluation: Theory, Techniques, and Applications, CRC Press, 2002.

[2] R. Baldev, T. Jayakumar and M. Thavasimuthu, Practical Non-Destructive Testing, 3 ed., Alpha Science International Ltd, 2007.

[3] S. S. Udpa and P. O. Moore, Nondestructive Testing Handbook- Electromagnetic Testing, 3 ed., vol. 5, ASNT, 2004.

[4] B. P. C. Rao, Practical Eddy Current Testing, New Delhi: Narosa Publishing House, 2007.

[5] R. Baldev, T. Jayakumar and B. P. C. Rao, "Review of NDT techniques for structural integrity," in *Sadhana*, New Delhi, In academy of proceedings in engineering sciences, 1995, pp. 5-38.

[6] H. Libby, Introduction to Electromagnetic NonDestructive Test Methods, New York: Weily-interscience, 1971.

[7] J. Blitz., Electrical and magnetic methods of Non-destructive testing, 2 ed., London: Chapman & Hall, 1997.

[8] B. P. C. Rao, "Eddy current testing: Basics," *Journal of Non Destructive Testing & Evaluation,* vol. 10, no. 3, pp. 7-16, 2011.

[9] K. V. Rajkumar, B. P. C. Rao, B. Sasi, K. Anish, T. Jayakumar, R. Baldev and K. K. Ray, "Characterisation of ageing behaviour in M250 grade maraging steel using eddy current non-destructive methodology," *Material Science Engineering - A,* vol. 464, no. 1, pp. 233-240, 2007.

[10] R. Baldev, C. V. Subramanian and T. Jayakumar, Non-destructive Testing of Welds, New Delhi: Wooddhead publications, 2000.

[11] K. Hedengren, D. Ritscher and B. Groshong, "Probe footprint estimation in eddy-current imaging," in *Review of Progress in Quantitative Nondestructive Evaluation*, New York, Springer US, 1990, pp. 845-852.

[12] G. Mook, F. Michel. and S. Jouri, "Electromagnetic imaging using probe arrays," *Journal of Mechanical Engineering,* vol. 57, no. 3, pp. 227-236, 2011.

[13] B. P. C. Rao, "Effective nondestructive testing of defects in engineering components," in *18th World Conference on Nondestructive Testing*, Sourth Africa, 2015.

[14] G. Mook, O. Hesse and V. Uchanin, "Deep penetration eddy currents and probes," *Material Testing,* vol. 49, pp. 258-264, 2007.

[15] B. Sasi, B. P. C. Rao, T. Jayakumar and R. Baldev, "Wavelet transform-based de-

noising method for processing eddy current signal," *Research in Nondestructive Evaluation,* vol. 21, no. 3, pp. 157-170, 2010.

[16] S. V. Vaseghi, Advanced Digital Signal Processing and Noise Reduction, 2 ed., John Wiley & Sons Ltd, 2000.

[17] A. V. Oppenheim and R. W. Schafer, Digital Signal processing, Prentice Hall, 1975.

[18] I. Pitas and A. N. Venetsanopoulos, Nonlinear Digital Filters: Principles and Applications, New york: Sprinter science and Business media, 1999.

[19] K. J. Anil, Fundamentals of Digital Signal Processing, New Delhi: Prentice-Hall of India Pvt Ltd, 2005.

[20] C. G. Rafel and E. W. Richard, Digital signal processing, New Delhi: Pearson Education Pte Ltd, 2002.

[21] K. Charles Chui, An Introduction to Wavelets, vol. 1, London: Academic Press, 1992.

[22] R. Polikar, The story of wavelets, in Physics and moern topics in Mechancical and Electrical engineering, N. Mastorakis, Ed., World Scientific and Eng. Society Press, 1999.

[23] S. G. Mallat, "Multifrequency channel decompositions of images and wavelet models," *IEEE transactions on Acoustics, speech and signal processings,* vol. 37, no. 1, pp. 2091-2110, 1989.

[24] Daubechies, Ten lectures on wavelets: Regional conference series in Applied Mathematics, Philadelphia: Society for Industrial and Applied Mathematics, 1992.

[25] T. Parimala, A. K. Ashafaq, G. Heber and G. R. Gao, "A fine grain load-adaptive algorithm of the 2D DWT for multithreaded architectures," *Journal of parallel and distributed computing,* vol. 64, pp. 68-78, 2004.

[26] Anutam and Rajni, "Performance analysis of image denoising with wavelet thresholding methods for different levels of decomposition," *The international journal of multimedia and its applications (IJMA),* vol. 6, no. 3, pp. 35-46, 2014.

[27] B. Toufik and N. Mokhtar, "The wavelet transform for image processing applications," in *Advances in wavelet theroy and their application in engineering, physics and technology*, Croatia, InTech, 2012, pp. 395-422.

[28] W. Yang and X. Ren, "Detecting impulses in mechanical signals by wavelet," *EURASIP J Appl Signal Process,* vol. 8, pp. 1156-1162 , 2004.

[29] R. Smid, D. Adam and K. Marcel, "Automated classification of eddy current signatures during manual inspection," *NDT&E International,* vol. 38, pp. 462-470, 2005.

[30] B. N. Singh and A. K. Tiwari, "Optimal selection of wavelet basis function applied to ECG signal denoising," *Digital Signal Processing,* vol. 16, pp. 275-287, 2006.

[31] L. Zhang, P. Bao and X. Wu, "Multiscale LMMSE-based image denoising with optimal wavelet selection," *IEEE Trans Circuits Syst Video Technol ,* vol. 15, no. 4,

pp. 469-481, 2005.

[32] O. A.Rosso, S. Blanco, J. Yordanova, V. Kolev, A. Figliola, M. Schurmann and E. Basar, "Wavelet entropy: a new tool for analysis of short duration brain electrical signals," *Journal of Neuroscience Methods,* vol. 105, pp. 65-75, 2001.

[33] B. Sasi, B. P. C. Rao, T. Jayakumar and R. Baldev, "Wavelet transform based denoising method for processing eddy current signals," *Research in Nondestructive Evaluation,* vol. 21, no. 3, pp. 151-170, 2010.

[34] D. L. Donoho, "De-noising by soft-Thresholding," *IEEE Transcation on information theory,* vol. 41, no. 3, pp. 613-627, 1995.

[35] D. L. Donoho and I. M. Johnstone, "Adapting to unknown smoothness via wavelet shrinkage," *biometrika,* vol. 81, pp. 425-455, 1994.

[36] G. S. Chang, B. Yu and M. Vetterli, "Adaptive wavelet thresholding for image denoising and compression," *IEEE Trans. Image Processing,* vol. 9, pp. 1532-1546, 2000.

[37] D. L. Donoho, I. M. Johnstone and D. Picard, "Wavelet shrinkage: asymptopia ?," *Journal of the Royal Statistical Society,* pp. 301-337, 1999.

[38] M. Vetterli and C. Herley, "Wavelet and filter banks: theory and design," *IEEE Transactions on Signal Processing,* vol. 40, pp. 2207-2224, 1992.

[39] I. Jolliffe, Principal Component Analysis, Springer-Verlag New York, Inc., 2002.

[40] N. Rajic, "Principal component thermography for flaw contrast enhancement and flaw depth characterisation in composite structures," *Composite Structures,* vol. 58, no. 4, pp. 521-528, 2002.

[41] V. Vavilov, "Noise-limited thermal infrared nondestructive testing," *NDT&E International,* vol. 61, pp. 16-23, 2014.

[42] F. Lingvall and T. Stepinski, "Automatic detecting and classifying defects during eddy current inspection of riveted lap-joints," *NDT& E International,* vol. 33, no. 1, pp. 47-55, 2000.

[43] A. Sophian, T. G. Y., D. Taylor and J. Rudling, "A feature extraction technique based on principal component analysis for pulsed Eddy current NDT," *NDT & E International,* vol. 36, no. 1, pp. 37-41, 2003.

[44] J. Karhunen and E. O. Hyvarinen, Independent Component Analysis, Wiley, New York, 2001.

[45] S. Roberts and R. Evarson, Independent componet analysis:Principles and Practice, Cambridge: Cambridge university press, 2001.

[46] A. Leon-Garcia, Probability and Random Processed for Electrical Engineering, 2 ed., New York: Addison Wesley, 1994.

[47] A. Hyvrinen, "New approximations of differential entropy for independent component analysis and projection pursuit," *In Advances in neural information processing systems,* vol. 10, pp. 273-279, 1998.

[48] A. Hyvarinen, "Fast and robust fixed-point algorithms for independent component analysis," *IEEE Trans. on Neural Networks,* vol. 10, no. 3, pp. 626-634, 1999.

[49] K. Koyama, H. Hoshikawa and N. Taniyama, "Investigation of eddy current testing of weld zone by uniform eddy current probe," in *15th WCNDT*, Rome, 2000.

[50] P. Xiang, S. Ramakrishnan, X. Cai, P. Ramuhalli, R. Polikar, S. S. Udpa and L. Udpa, "Automated analysis of rotating probe multi-frequency eddy current data from steam generator tubes," *Int. Journal of Applied electromagnetic and mechanics,* vol. 12, pp. 151-164, 2000.

[51] M. Das, H. Shekhar, X. Liu, R. Polikar, P. Ramuhalli, L. Udpa and S. Udpa, "A generalized likelihood ratio technique for automated analysis of bobbin coil eddy current data," *NDT&E International,* vol. 35, no. 5, pp. 329-336, 2002.

[52] S. S. Udpa and W. Lord, "Fourier descriptors classification scheme for differential probe signal," *Materials Evaluation,* vol. 42, pp. 1136-1141, 1984.

[53] B. P. C. Rao, "An intelligent image scheme for automated eddy current testing of austenitic stainless steel plates and welds," Doctoral Thesis, Saarland University, Germany, 2000.

[54] E. Pardo, J. S. Emeterio, M. Rodriguez and A. Ramos, "Noise reduction in ultrasonic NDT using undecimated wavelet transforms," *Ultrasonics,* vol. 44, pp. e1063--e1067, 2006.

[55] L. A. N. M. Lopez, D. K. S. Ting and B. R. Upadhyaya, "Removing eddy-current probe wobble noise from steam generator tubes testing using wavelet transform," *Progress in Nuclear Energy,* vol. 50, pp. 828-835, 2008.

[56] S. Thirunavukkarasu, B. P. C. Rao, T. Jayakumar and B. Raj, "Techniques for processing remote field eddy current signals from bend regions of steam generator tubes of prototype fast breeder reactor," *Annals of Nuclear Energy,* vol. 38, no. 4, pp. 817-824, 2011.

[57] J. Lazaro, J. S. Emeterio, A. Ramos and J. Fernandez-Marran, "Influence of thresholding procedures in ultrasonic grain noise reduction using wavelets," *Ultrasonics,* vol. 40, pp. 263-267, 2002.

[58] P. Y. Joubert, A. Tassin and Y. L. Diraison, "Source separation techniques applied to the detection of subsurface defects in eddy current NDT of aeronautical lap-joints," *NDT &E Intenational,* vol. 43, pp. 606-614, 2010.

[59] Y. L. Diraison, P. Y. Joubert and D. Placko, "Characterization of subsurface defects in aeronautical riveted lap-joints using multi-frequency eddy current imaging," *NDT&E International,* vol. 42, no. 2, pp. 133-140, 2009.

[60] B. P. C. Rao, S. Thirunavukkarasu, K. Krishnanand, T. Jayakumar, P. Kalyanasundaram and B. Raj, "Enhancement of magnetic flux leakage images of defects in carbon steel using Eigen vector based approach," *Nondestructive Testing and Evaluation,* vol. 23, no. 1, pp. 35-42, 2007.

[61] P. Kalyanasundaram, S. Thirunavukkarasu, B. P. C. Rao, T. Jayakumar and Baldev Raj, "Eigen value based approach for enhancement of eddy current images,"

Research in Nondestructive Evaluation, vol. 18, no. 1, pp. 13-22, 2007.

[62] B. H. Shin, P. Ramuhalli, L. Udpa and S. Udpa, "Independent component analysis for eddy current inspection of steam generator tubing," *Review of Progress in Quantitative Nonsdestructive Evaluation,* vol. 23A, pp. 597-604, 2004.

[63] S. Amrai, A. Cichocki and H. H. Yang, "A new learning algorithm for blind signal separation," in *Advances in neural information processing systems*, Cambridge, MIT Press, 1996, pp. 757-763.

[64] M. A. V. Bermejo, "Predictive and measurement methods for delta ferrite determination in stainless steels," *Welding Science,* pp. 113-121, 2012.